

Electronic Thesis and Dissertation Repository

12-17-2019 10:30 AM


Effects of Impurities on Calcium Oxalate Crystallization as Measured by Atomic Force Microscopy

Himasha Wijesekara
The University of Western Ontario

Supervisor
Hutter, Jeffrey L.
The University of Western Ontario

Graduate Program in Physics
A thesis submitted in partial fulfillment of the requirements for the degree in Doctor of Philosophy
© Himasha Wijesekara 2019

Follow this and additional works at: <https://ir.lib.uwo.ca/etd>

 Part of the [Condensed Matter Physics Commons](#), and the [Statistical, Nonlinear, and Soft Matter Physics Commons](#)

Recommended Citation

Wijesekara, Himasha, "Effects of Impurities on Calcium Oxalate Crystallization as Measured by Atomic Force Microscopy" (2019). *Electronic Thesis and Dissertation Repository*. 6785.
<https://ir.lib.uwo.ca/etd/6785>

This Dissertation/Thesis is brought to you for free and open access by Scholarship@Western. It has been accepted for inclusion in Electronic Thesis and Dissertation Repository by an authorized administrator of Scholarship@Western. For more information, please contact wlsadmin@uwo.ca.

Abstract

Calcium oxalate crystals are found in kidney stones as either calcium oxalate monohydrate (COM) or calcium oxalate dihydrate (COD). COM crystals are the most abundant form as they are thermodynamically more stable than COD crystals under physiological conditions. Certain aspartic acid-rich molecules such as osteopontin (OPN) are known to affect stone formation by inhibiting COM and COD growth. We have studied COM {010} and COD {100} faces in the presence of OPN, poly-aspartic acid (poly-ASP) and synthetic peptides derived from OPN to investigate the inhibitor mechanism.

We observed that poly-ASP preferentially inhibits one particular direction of {010} faces on COM crystals, creating “finger-like” features, while growth continues in other directions. We find that these features appear at a threshold concentration of poly-ASP that varies with the length of the polymer. Attempts to model the threshold concentration suggest that this is due to a competition between adsorption of polymer to already-pinned steps and removal of poly-ASP by desorption and possibly coverage by advancing steps between strongly pinned steps.

Growth of {100} faces of COD crystals in the presence of synthetic peptides derived from OPN with different iso-electric points displayed varying levels of inhibition. The two principal directions of the elongated elliptical hillocks on {100} faces were inhibited to different degrees by the peptides. This preferential inhibition is most likely the result of different Ca^{2+} ion densities and structures of the two different step directions.

The effects of imaging on the growth itself were studied for the case of COM growth in the presence of OPN. In the presence of OPN molecules, a continuously-scanned area showed faster growth relative to a larger area scanned less frequently. This enhanced vertical growth in the continuously-scanned area was found to vary with the OPN concentration and calcium oxalate supersaturation. We modeled this effect using a modified version of the Cabrera-Vermilyea model (1958), in which steps are pinned by adsorbed impurities, resulting in a decreased propagation speed due to the resulting curvature. In our case, we assume adsorption directly to steps, rather than to terraces as in the Cabrera-Vermilyea model.

Key words: Calcium oxalate monohydrate, Atomic force microscope, Osteopontin, crystal growth, inhibition, kidney stones

Summary for Lay Audience

Crystallization is an important field of study because many materials, both in nature and industry, are crystalline. In some cases, crystallization is undesired. One such example is the formation of kidney stones, which are comprised mainly of calcium oxalate. About 10% of the human population suffers from kidney stones at some point in their lives. We are using the atomic force microscope (AFM) to study the mechanism by which molecules found in urine prevent calcium oxalate crystallization.

Calcium oxalate crystals are found in kidney stones in two forms: calcium oxalate monohydrate (COM) and calcium oxalate dihydrate (COD). Proteins and large molecules found in urine are known to intervene in the process of crystal formation. We have used poly-aspartic acid – an amino acid – and osteopontin (OPN) – a large protein found in urine – to affect the growth of COM and COD crystals synthesized in the laboratory. Using the AFM, we were able to observe crystal growth in the presence of these inhibitors and develop a model to explain the inhibition mechanism. Having a better understanding of COM and COD crystallization in the presence of proteins will lead to improved therapeutic measures to control kidney stones.

The AFM is a member of the scanning probe microscope family, which allows real-time investigation of surface properties at a wide range of length scales. During imaging, a sharp tip scans across the sample and records the topography by measuring forces between the tip and sample surface. We studied the effects of the interaction between the AFM tip and sample surface on crystallization. We find that in the absence of inhibitors, the interaction is negligible, and growth is unaltered. In the presence of OPN, we observed enhanced growth due to scanning, suggesting that the imaging process removes inhibitors from the surface. We propose a model for this effect, which has important implications for the interpretation of AFM observations of crystal growth and inhibition.

Acknowledgments

I would like to take this opportunity to thank my supervisors Dr. Jeffrey Hutter, Dr. Graeme Hunter and Dr. Harvey Goldberg, for their support and guidance. My extended gratitude goes toward my advisory committee for spending their time evaluating my work. I appreciate the assistance of our collaborators from Schulich School of Medicine and Dentistry, specially Yinyin Liao for teaching me techniques and protocols in the laboratory.

My sincere thanks go to physics and astronomy staffs, Clara Buma, Jodi Guthrie, Brian Davis and Jennifer Tilson for their administrative support and kind words.

Once again, I would like to express my gratitude to Dr. Hutter, who very patiently guided me through all stages of this program and for standing by me through the challenges in my personal life. It was a privilege to be his student.

Finally, I would like to thank my family and friends, specially my husband Asanka, for his ultimate support.

Table of contents

Abstract	i
Summary for Lay Audience	ii
Acknowledgments.....	iii
List of Figures	vi
List of Tables	x
List of Appendices	xi
List of Acronyms	xii
1. Introduction to Calcium Oxalate Crystallization.....	1
1.1 Crystallization	2
1.1.1 Phase Transitions	2
1.1.2 Nucleation	4
1.1.3 Crystal Growth.....	5
1.1.4 Inhibition.....	7
1.2 Calcium Oxalate.....	10
1.2.1 Calcium Oxalate Monohydrate Crystals.....	11
1.2.2 Calcium Oxalate Monohydrate Inhibition	11
1.2.3 Calcium Oxalate Dihydrate Structure.....	16
1.2.4 Calcium Oxalate Dihydrate Inhibition.....	18
1.3 Experimental Techniques.....	20
1.3.1 AFM Studies	20
1.3.2 AFM on Crystal Growth	22
2 Materials and Methods	25
2.1 Solution Preparation.....	25
2.2 Crystal Sample Preparation.....	25
2.3 Peptide Preparation	26
2.4 AFM Imaging.....	26
2.4.1 Imaging in Fluid.....	27
2.4.2 Inline Mixing with a Syringe Pump.....	27
2.5 Movies and Velocity Calculations	29
2.5.1 Drift Correction.....	29
2.5.2 Calculating Velocity	29
3 Directional Pinning of Calcium Oxalate Monohydrate Crystallization by poly(aspartic acid)	
	31

3.1	Motivation/ Importance.....	31
3.2	Materials and Methods.....	32
3.3	Results.....	34
3.4	Discussion.....	39
3.5	Conclusion.....	45
4	Calcium Oxalate Dihydrate Inhibition with Osteopontin Peptide Series.....	46
4.1	Introduction/ Motivation.....	46
4.2	Materials and Methods.....	49
4.3	Results.....	51
4.4	Discussion.....	54
4.5	Conclusion.....	58
5	AFM Scanning Effects on Sample Growth and Inhibition.....	60
5.1	Introduction.....	60
5.2	Method.....	62
5.3	Results.....	65
5.4	Discussion.....	71
5.5	Conclusion.....	78
6	Conclusion and Future Work.....	80
6.1	Summary.....	80
6.2	Future Work.....	81
6.2.1	COM and COD Crystal Growth.....	81
6.2.2	AFM Tip Effect on Crystal Growth and Inhibition.....	82
6.3	Preliminary Work.....	82
6.3.1	Fluorescently Labeled Peptides to Locate poly-ASP on {010} Face of COM.....	82
6.3.2	Fluorescence Recovery after Photo bleaching (FRAP).....	83
6.3.3	High Resolution AFM Imaging.....	86
7	Reference.....	89
	Appendix A.....	98
	Recipes for the Solutions Used in Experiments.....	98
	Appendix B.....	102
	Design of the Continuous Flow System for the AFM Fluid Cell.....	102
	Appendix C.....	104
	List of Amino Acids.....	104

List of Figures

Figure 1.1 (a) Phase (<i>PT</i>) diagram of a single component material. b) Variation of free energy of a material as a function of temperature at a constant pressure.	2
Figure 1.2. Change in total free energy due to the formation of a sphere of solid phase of radius <i>r</i>	5
Figure 1.3. Surface configuration with a terrace bounded by a step with a kink site.	6
Figure 1.4. Schematic of growth of a square spiral at five different times.	7
Figure 1.5. Retarded growth due to inhibitors. The dots and the curves represent the inhibitors and curved steps growing between pinning sites.....	8
Figure 1.6. Variation of step velocity with supersaturation.	9
Figure 1.7. (a) Schematic of the unit cell of the COM crystal. (b) (010) face of the unit cell with atom positions. (c) SEM image of a COM crystal, with faces indicated.	11
Figure 1.8. AFM deflection image of a growth hillock on a {010} face of a COM crystal. Arrows show the growth direction of propagation each step.	12
Figure 1.9. Cross-sections of the two main growth directions on {010} face. Water molecules are not shown for simplicity. a) [120] step with (021) plane as the riser. b) [121] step with (121) plane as the riser.....	13
Figure 1.10 Crystals structure and SEM images of different types of COD crystals. (a) Schematic of the unit cell of the COD crystal.....	17
Figure 1.11 Chemical structures of amino acids used on COD growth and inhibition.	19
Figure 1.12. Schematic diagram of the atomic force microscope.....	21
Figure 1.13. Variation of force relative to the distance between tip and the sample.....	21
Figure 2.1. Schematic of a typical experimental set up with in-line mixing using a dual syringe pump.	28
Figure 2.2. Alternate AFM deflection image of a growth hillock on a {010} face of a COM crystal showing an advancing step. The dashed lines in (b) and (c) show previous positions of the step, while the solid line shows its current location.	30

Figure 3.1. Images of the {010} faces of COM crystals. (a) SEM image of a COM crystal with the {010} face horizontal. (b) AFM height image of a (010) face. (c) Higher resolution AFM deflection image of a {010} face showing a growth hillock, defined by growth steps aligned with [121] and [120] step directions.	34
Figure 3.2. AFM images of growth steps on the same region of a COM {010} face (a) before and (b) and (c), after the introduction of 0.06 $\mu\text{g/ml}$ poly-ASP (50 residue).....	35
Figure 3.3. Threshold concentration required for directional pinning for growth in a 0.3 mM calcium oxalate solution. The solid curve represents a fit to the model discussed in section 3.4.	35
Figure 3.4. Threshold pinning concentration as a function of calcium oxalate concentration for a poly-ASP chain length of 30 amino acid residues. Solid curve represents a fit to the pinning model discussed in section 3.4	36
Figure 3.5 Processed AFM images leading to isolated features. Red box tracks the same feature. (a) 8-bit grey scale image of an AFM height image. Boxes indicate edges of few features. (b) Processed image with edges skeletonized. (c) A magnified image of an isolated feature.	37
Figure 3.6. Average lateral distance between strongly-pinned steps as a function of calcium oxalate concentration.	37
Figure 3.7 Evolution of cross-sections measured perpendicularly to the strongly pinned steps on a COM {010} face during inhibition from 0.125 $\mu\text{g/ml}$ of poly-ASP (10 residues).	38
Figure 3.8. AFM height images of {010} face of COM crystals imaged in the presence of poly-ASP.	39
Figure 3.9 Schematic of the behavior of poly-ASP on COM crystal surface.....	40
Figure 3.10 Configuration of poly-ASP molecules on a step at threshold pinning.	42
Figure 4.1. (a) Schematic of the unit cell of the COD crystal. (b) (100) face of the unit cell with atom positions indicated.	47
Figure 4.2. SEM images of different types of COD crystals. (a) Tetragonal bipyramid COD crystals. (b) Elongated tetragonal prism COD crystals.	47

Figure 4.3 Cross sections showing oxalate ion and Ca^{2+} ion positions on (a) $\{100\}$ faces looking down the z-axis and (b) $\{101\}$ faces looking down the y-axis.....	48
Figure 4.4 AFM deflection images of (a) a triangular $\{101\}$ COD face. “blobs” seen on the surface are presumed to be either glue or a poly-AA film. (b) triangular hillocks on a $\{101\}$ face, and (c) elongated elliptical hillocks on a $\{100\}$ face.....	52
Figure 4.5 AFM images of COD (100) faces, 1 min after inhibition with (a) pOPAR, (b) P3, (c) HHS and (d) DVL.....	53
Figure 4.6 Measurement of aspect ratios of hillocks on the (100) face of a COD crystal for (a) growth without an inhibitor (b) growth in the presence of 5 $\mu\text{g/ml}$ pOPAR.	53
Figure 4.7 Change in aspect ratio of hillocks on the (100) face of COD crystals, after introducing 5 $\mu\text{g/ml}$ peptide solution, relative to pure growth.....	54
Figure 4.8 AFM deflection image of a growth hillock on a $\{100\}$ face of a COD crystal.	55
Figure 4.9 Two possible step risers for the $[001]$ step on $\{100\}$ faces: (a) (010) plane, (b) (110) plane. For convenience, the steps are shown to be several oxalate ions in height, but in reality, may be shorter.	56
Figure 4.10 Two possible step risers for the $[010]$ step on $\{100\}$ faces: (a) (001) plane, (b) (101) plane. For convenience, water molecules are not shown, and steps are shown with a height of several unit cells.....	57
Figure 4.11 Atomic structures of COD $\{100\}$ and $\{010\}$ faces, illustrating similar atom positions.....	58
Figure 5.1 Schematic of the expected evolution of the height profile for tip-enhanced growth. (a) AFM scan area divided into a continuously scanned inner area and a periphery that is only scanned periodically. (b) Evolution of the height profile along the red line.	64
Figure 5.2 Red curve: line profile acquired from an AFM image 20 minutes into crystal growth at 0.3 mM in the presence of 0.5 $\mu\text{g/ml}$ OPN.	65
Figure 5.3 Atomic force microscope images of COM crystal growth without inhibitor acquired with an imaging force of 18 nN force at times of a) 0 min into the experiment, b) 4 min into the experiment and c) 10 min into the experiment.	66

Figure 5.4 Atomic force microscope images of a COM {010} face grown from 0.3 mM CaOx solution in the presence of 0.25 $\mu\text{g/ml}$ OPN. a) First image after inhibitor is introduced. b) 12 minutes into the experiment. The scan area is starting to show enhanced growth relative to the periphery. c) 24 minutes into the experiment. Enhanced growth due to scanning is very prominent.....	67
Figure 5.5. a) Locations of line profiles used to measure differential growth between the continuously scanned and periphery regions. b) Two profiles in the periphery used to estimate the uncertainty and as control profile shapes.	68
Figure 5.6. Height profiles of a line running from the periphery to the inner scan area (red dashed line in Figure 5.5 a) of the 2 μm scans acquired at 4 minute intervals.	68
Figure 5.7 Average height difference between the periphery and continuously scanned region as a function of time for a {010} face grown with 0.5 $\mu\text{g/ml}$ OPN from 0.3 mM calcium oxalate solution.....	69
Figure 5.8. Growth rate of the continuously scanned area relative to the periphery, ΔR , as a function of inhibitor concentration.	70
Figure 5.9 Growth rate of the continuously scanned area relative to the periphery for different calcium oxalate concentrations in the presence of 0.5 $\mu\text{g/ml}$ OPN.....	71
Figure 5.10. AFM images acquired 12 minutes apart while inhibited with 1 $\mu\text{g/ml}$ OPN.	75
Figure 6.1 Confocal image of {010} faces of COM crystals in the presence of 20 nM of fluorescently labeled poly-ASP. Size of a crystal is in the range of 10 – 15 μm	83
Figure 6.2 Confocal images of COM crystals inhibited with fluorescently labeled peptides. a) COM crystals with {010} face up showing the intensity of the adsorbed peptide on the surface. b) An example of bleached regions indicated on COM crystal {100} face.....	84
Figure 6.3 Recovery of intensity of a bleached region of a COM {010} face normalized by the initial control intensity for P3 at a concentration of 2 $\mu\text{g/ml}$	85
Figure 6.4 High resolution AFM height image of the {010} face of a COM crystal. The inset is a scaled drawing of the crystal lattice aligned with the orientation of the crystal.	87
Figure 6.5 High-resolution AFM deflection images of the {010} face of a COM crystal inhibited with 9 nM of poly-ASP 50 acquired 60 s apart.	88

List of tables

Table 1-1 Properties of calcium oxalate hydrates	10
Table 1-2 Phosphorylated peptide sequences derived from OPN.	14
Table 2-1 Spring constant and the tip radius of the AFM tips.....	27
Table 3-1 Fit parameters for equation 3.11 in Figure 3.3 and Figure 3.4.....	44
Table 4-1 Phosphorelated peptide sequences derived from OPN and their iso-electric points...	51
Table 4-2 Ca ²⁺ ion density for each of the faces.....	55
Table 5-1. Fit parameters for the step adsorption model.....	78

List of appendices

Appendix A: Recipes for the solutions used in experiments	98
Appendix B: Design of the continuous flow system for the AFM fluid cell.....	102
Appendix C: List of amino acids	104

List of Acronyms

AFM	Atomic force microscope
CaOx	Calcium oxalate
COD	Calcium oxalate dihydrate
COM	Calcium oxalate monohydrate
C-V model	Cabrera–Vermilyea model
DVL	OPN 113–128 peptide
FRAP	Fluorescence recovery after photo bleaching
HHS	OPN 97–112 peptide
MD	Molecular dynamics
NC	Nephrocalcin
OPN	Osteopontin
P3	OPN 220–235 with three phosphates
poly-ASP	poly aspartatic acid
poly-AA	poly acrylic acid
pOPAR	Peptide of OPN containing residues 65–80
THP	Tamm-Horsfall protein

1. Introduction to Calcium Oxalate Crystallization

Kidney stone disease is a urological disorder that afflicts 10% of the human population [1], leading to considerable pain and, occasionally, renal failure. Kidney stones are composed largely of calcium salt crystals, the major components being calcium oxalates, which grow and aggregate in supersaturated urine solutions. However, the formation of calcium oxalate crystals in urine does not always imply kidney stones, as crystals are commonly found in both healthy humans and stone formers alike. When few crystals are formed, most are vacated with urine and do not contribute to stone formation. Physiological difficulties arise from retention of large crystals or aggregates, or from small crystals collected in the lumen of a tubule. Crystals may be retained without passing with urine due to their size, shape or adhesion to the epithelium [2].

Calcium oxalate in kidney stones is typically found in two different crystalline forms, each distinguished by different ratios of water: calcium oxalate monohydrate (COM) and calcium oxalate dihydrate (COD) [2]. The most common stones are microcrystalline aggregates containing calcium oxalate monohydrate (COM) as the primary constituent [3,4]. There are number of factors that determine the morphology of kidney stones, such as kinetics of crystallization, crystalline phase, urine disorders and presence of other stones such as ammonium urate [2]. Stone formation is strongly influenced by the anatomical context of the urinary tract. Anomalies such as constricted flow from the bladder or urinary tract infection induce formation of multiple stones [5,6].

Research on kidney stone formation and its prevention plays a major role in the process of developing therapeutic measures to minimize the suffering that occurs with the disease. In order to gain a better understanding of the matter, it is helpful to consider the background of crystal formation and growth. The following sections of this Chapter will lead us through the basic concepts of crystal growth to the background of previous work on calcium oxalate hydrates.

1.1 Crystallization

1.1.1 Phase Transitions

The phase of a material is its state of matter, and typically only one phase of a single-component system is stable at a particular temperature (T) and pressure (P). This allows us to construct a phase diagram as in Figure 1.1a) by mapping regions of P , T for each phase. The boundary between regions is a P as a function of T and represents the conditions at which two phases coexist, so that the corresponding phases are in equilibrium along the boundary. If the temperature or the pressure changes, one or the other phase becomes more stable, which leads to a phase transition.

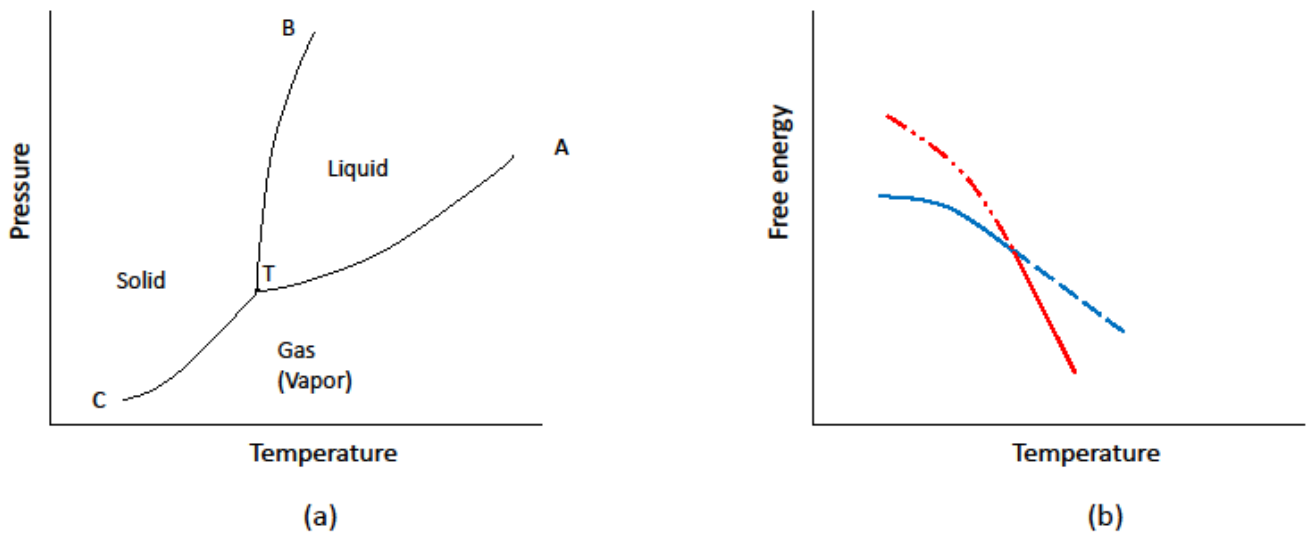


Figure 1.1 (a) Phase (PT) diagram of a single component material. (b) Variation of free energy of a material as a function of temperature at a constant pressure. The two curves represent the free energy functions of the two phases, and the phase transition temperature at which the two phases can coexist is at the point where the two curves cross.

The Gibbs free energy $G = U + PV - TS$ is the quantity that determines the stability of a state at a constant T and P . Here, U is the internal energy, P is the ambient pressure, V is the volume of the system, T is the absolute temperature and S is the entropy. A plot of free energy versus the

temperature for two phases is shown in Figure 1.1b at a constant pressure. It illustrates a single temperature at which the two phases can coexist, where the two curves cross. At other temperatures, the thermodynamically stable phase will be the one for which G is lower. Once G is minimized, the system is in equilibrium at that T and P . The chemical potential of the phase, which is the derivative of the Gibbs free energy with respect to the number of particles in the system, will also be in equality at the equilibrium state. The difference between the chemical potentials of the two phases, which is a function of P and T , represents the thermodynamic “driving force” for crystallization to occur and is called the supersaturation [7].

The systems of interest in this study are solutions of calcium (Ca^{2+}) and oxalate ($\text{C}_2\text{O}_4^{2-}$) ions dissolved in water. While the stable phase depends on temperature and pressure, since this is not a single component system, it also depends on the concentrations of components. In practice, we are concerned with the equilibrium behaviors at constant pressure and temperature. The equilibrium concentration is characterized by the solubility constant k_{sp} , which determines the degree to which the ions dissociate in the solution. A solution is considered saturated if

$$k_{sp} = [C_1]^{A_1}[C_2]^{A_2} \dots, \quad 1.1$$

where $[C_1]$ and $[C_2]$ are the concentrations of the ions, each raised to its coefficient A_1 and A_2 , in the equilibrium dissolution reaction,



High ion concentrations, due to either concentrated solutions or the presence of an additional ionic species, result in a modification of the equilibrium condition due to electrostatic screening, which reduces the interactions between ions. For example, Na^+ and Cl^- (salt) ions in a calcium oxalate solution will shield the oxalate ions from calcium ions. This modification is characterized by the ionic strength of the solution, which can be calculated using the equation

$$I = \frac{1}{2} \sum_i^n c_i z_i^2 \quad 1.3$$

where c_i and z_i represent the concentration and ionic charge of the i^{th} species.

The condition for equilibrium then becomes

$$k_{sp} = [a]^{A_1}[a_2]^{A_2} \dots, \quad 1.4$$

where a_i is the activity of the i^{th} ion. Activity is proportional to the molar concentration of the ions according to

$$a_i = \gamma_i C_i. \quad 1.5$$

where γ_i is the activity coefficient. For a dilute electrolytic solution, γ_i can be approximated by

$$\log \gamma_i = -AZ_i^2 I^{0.5}, \quad 1.6$$

where A is known as the Debye-Huckel constant. For aqueous solutions at 25 °C, the Debye-Huckel constant [69] has a value of

$$A = 0.51 \text{ mol}^{-1/2} \text{ dm}^{3/2}.$$

For such a solution, the supersaturation is defined as

$$\sigma = \frac{\Delta\mu}{k_B T} = \frac{1}{2} \ln \left[\frac{\prod_i^n a_i}{k_{sp}} \right]. \quad 1.7$$

The chemical potential $\Delta\mu$ of the supersaturated solution provides the driving force needed for nucleation of a new phase.

1.1.2 Nucleation

Changing the pressure or temperature of a system in a way that brings the system below the coexistence curve on a PT diagram promotes solidification. As a new phase is then thermodynamically favored, solidification begins with the nucleation of a seed crystal. The formation of a solid phase necessarily results in the creation of an interface between phases. The resulting change in the free energy therefore consists of two parts: the energy required to form the new surface, and the bulk free energy change associated with the phase transition. For a spherical nucleus of radius r , the change in free energy ΔG is

$$\Delta G = -\frac{4}{3} \pi r^3 \Delta\mu + 4\pi r^2 \gamma, \quad 1.8$$

where $\Delta\mu = \mu_l - \mu_s$ is the difference in the chemical potential of the two phases and γ is the surface energy of the interface between the solid and liquid phases. These newly formed nuclei will increase the free energy of the system for small r , favoring them to dissolve rather than grow. But if they get large enough, the decrease in the bulk free energy becomes large enough that growth of the nuclei will lower the free energy, favoring growth. That is, the system must

overcome an energy barrier, as shown in the Figure 1.2, of ΔG^* . Once this barrier is overcome, the free energy will decrease with increasing radius. The radius at this maximum free energy is called the critical radius r^* [7] and is given by

$$r^* = \frac{-2\gamma}{\Delta\mu}, \quad 1.9$$

where of course, the change in chemical potential $\Delta\mu$ due to the phase transition is negative.

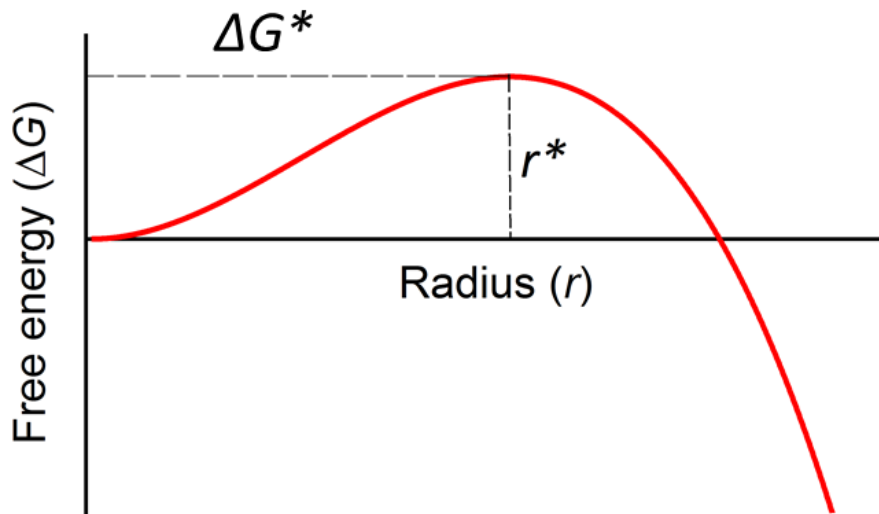


Figure 1.2. Change in total free energy due to the formation of a sphere of solid phase of radius r

1.1.3 Crystal Growth

Once a nucleus larger than the critical radius has formed, it will continue to grow via the addition of so called “adatoms” to the surface – crystallizing units, such as ions in the case of precipitation from solution. The kinetics of crystallization can be controlled by the rate of diffusion of adatoms from the melt or solution to the surface, or by their rate of incorporation into the growing crystal. In the case of faceted growth, adsorption is to a plane and the adatoms are initially bound only weakly. In that case, they diffuse on the surface until they encounter a step or desorb from the surface. When an adatom encounters a step, it becomes more strongly bound. If it reaches a kink site as shown in Figure 1.3, it will form multiple bonds, making it unlikely to desorb from the crystal. This results in the advance of the step position.

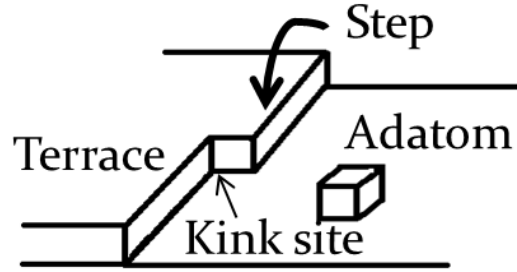


Figure 1.3. Surface configuration with a terrace bounded by a step with a kink site.

This mechanism of crystal growth is only effective when a step exists on the crystal surface [7]. The growth rate of a faceted crystal is controlled by both the rate of formation of steps and the lateral propagation of those steps. If the velocity of a straight step moving on the surface is v_0 , the spacing between steps is d and the height of each step is a , then the normal growth rate R of the face is

$$R = \frac{av_0}{d}. \quad 1.10$$

Smooth flat surfaces require a source of steps, which can be achieved by 2D nucleation or the presence of a screw dislocation [7]. 2D nucleation requires the formation of a stable cluster of adatoms on the surface with a nucleation barrier analogue to that of 3D nucleation. Even if a 2D nucleus is nucleated, growth will cease once the step reaches the crystal edge until a new cluster is formed [7]. On the other hand, the existence of a screw dislocation provides a nonvanishing source of steps, so once they appear, they dominate the growth. In that case, the growth rate is principally determined by the rate of lateral movement of steps and is not limited by step formation [7]. As a simple model, consider a square lattice as illustrated in Figure 1.4 with a screw dislocation perpendicular to the face. Suppose that initially a straight step originates from the defect, providing a site for adatoms to bind. In a supersaturated solution, this step will advance and a step normal to the initial step will appear out of necessity. The new portion cannot advance until its length is greater than a certain critical length l^* . When the second step advances, a third edge will form and propagate when it is long enough. The end result is a

square spiral of steps with a spacing of $4l^*$. For a growth spiral with step height a and step velocity v_s , growth rate normal to the surface is

$$R = \frac{av_0}{4l^*}. \tag{1.11}$$

This is an approximation for a simple square lattice. For an isotropic material the result will be a smooth spiral, and in reality, we will see a shape in between.

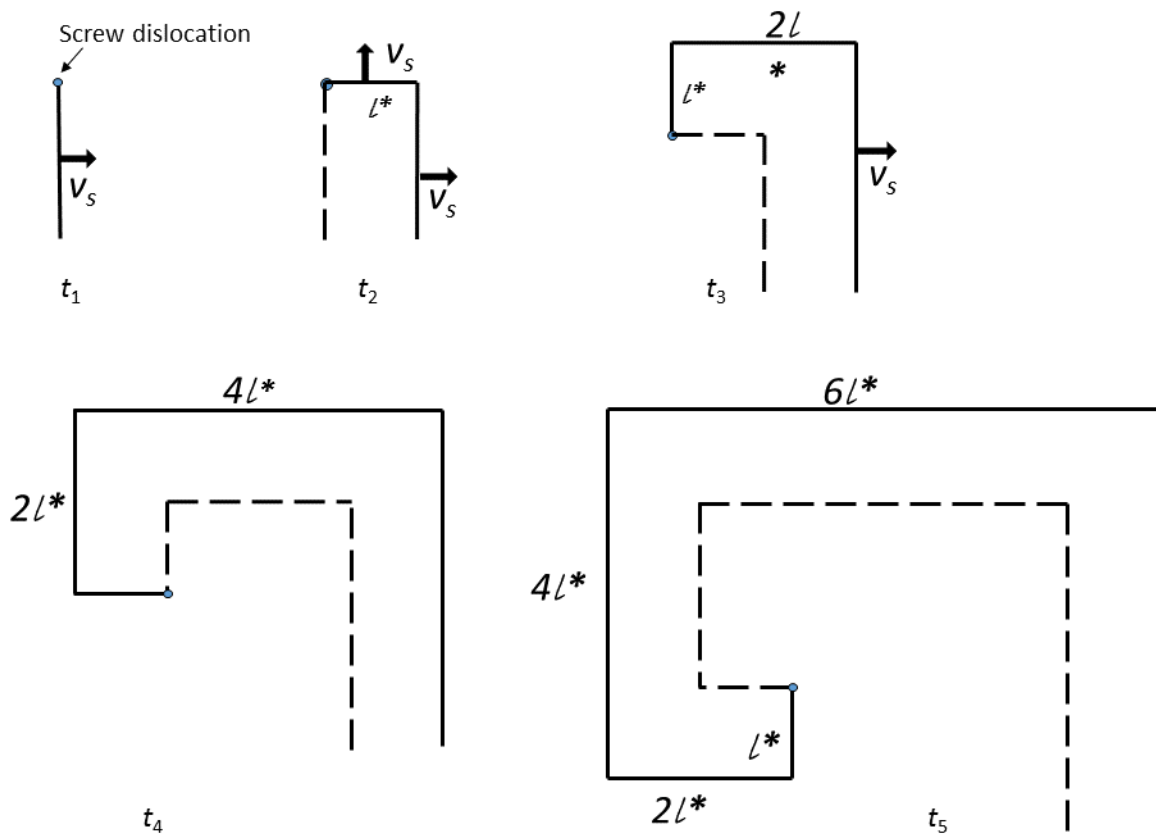


Figure 1.4. Schematic of growth of a square spiral at five different times. l^* and v_s represent the critical length and velocity of the step, respectively.

1.1.4 Inhibition

The shape of a crystal is controlled by a combination of energetic and kinetic factors. The equilibrium shape of a crystal is achieved by minimizing its total surface energy. However, the shape during growth is controlled by the growth rates of the different faces. It is possible to modify the shape of the crystal by introducing ions or molecules that alter the relative growth

rates of different faces through interactions with step edges [8]. Such particles are called kinetic inhibitors and affect crystallization kinetics without changing the thermodynamics of the system. In other words, the phase diagram of the system is not changed. There are several mechanisms by which growth can be modified: step pinning, impurity incorporation, kink blocking and step-edge adsorption [8]. Each of these mechanisms displays a specific dependence of step speed on inhibitor concentration and supersaturation of the solution.

The accepted model for the step pinning mechanism by which kinetic inhibitors affect crystal growth and morphology was described 60 years ago by Cabrera and Vermilyea [9,10]. The “C-V” model suggests that molecules that adsorb strongly to a growth surface will pin the advancing steps. Steps must then curve around the pinning sites for growth to proceed (Figure 1.5), reducing the effective supersaturation via the Gibbs-Thompson effect [10].

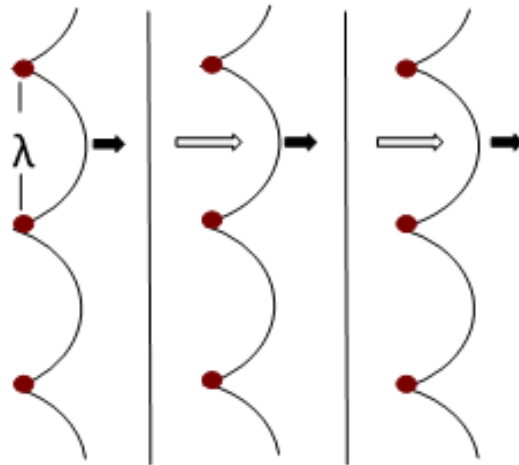


Figure 1.5. Retarded growth due to inhibitors. The dots and the curves represent the inhibitors and curved steps growing between pinning sites. Arrows show the relative velocities between retarded and normal growth velocities. λ is the space between inhibitors.

Curvature in steps advancing between inhibitors spaced λ apart, results in a decreased step velocity v_s , according to

$$v_s = v_0 \left(1 - \frac{2r^*}{\lambda}\right). \quad 1.12$$

The effective velocity of the steps on an inhibited face will then be somewhere between v_0 and v_s . When the spacing λ between the impurities is less than twice the critical radius r^* , growth will be arrested completely. Several AFM studies have shown the transition of straight steps to curved steps due to the introduction of inhibitors to the system [11–13]. Since v_0 is proportional to supersaturation, and r^* is inversely proportional to supersaturation, for small supersaturations the growth velocity will depend on supersaturation as illustrated in Figure 1.6.

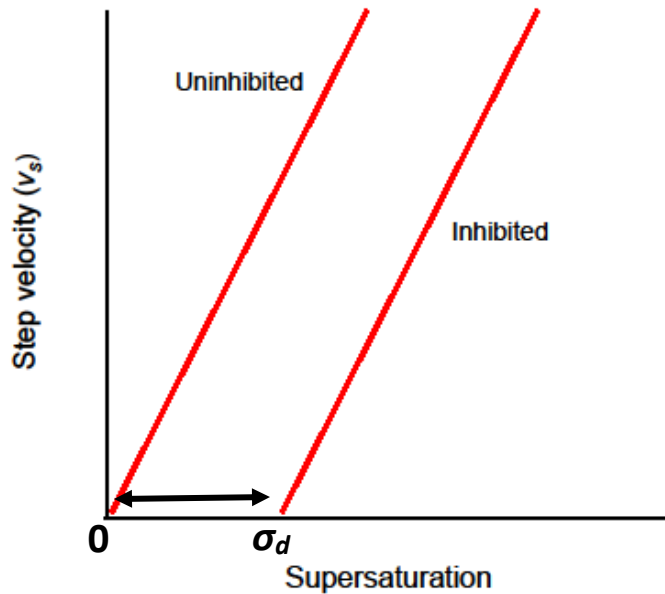


Figure 1.6. Variation of step velocity with supersaturation. An inhibited system with low inhibitor concentrations shows a region where growth velocity is zero below a threshold supersaturation. This region is known as the dead zone (σ_d).

Impurity incorporation occurs when inhibitor molecules become captured by advancing steps or kink sites and become part of the crystal. This will change the internal energy and therefore change the effective supersaturation of the crystal [8]. It may also change the shape of the crystal due to different incorporation rates into distinct steps [14].

Growth modification also occurs with kink blocking. In this case, steps with low number of kink sites propagate by the formation of a new kink site. Impurities can adsorb to kink sites for a

short period of time, leading to an effective decrement in kink density and blocking the site from adatoms. This will stop the advancement of the kink site, effectively reducing growth [15].

1.2 Calcium Oxalate

Understanding the growth of calcium oxalate crystals is a topic of interest in biomineralization and medicine. Many studies have explored how different calcium oxalate crystals form and how unwanted mineralization such as kidney stones are commonly prevented [16]. Calcium oxalate crystals have three degrees of hydration, two of which can be found in kidney stones. Calcium oxalate monohydrate (COM), also known as whewellite ($\text{CaC}_2\text{O}_4 \cdot \text{H}_2\text{O}$), is the most abundant form in the urine of stone formers. Calcium oxalate dihydrate (COD) crystals known as weddellite ($\text{CaC}_2\text{O}_4 \cdot 2\text{H}_2\text{O}$), are generally flushed out more easily as they are less adherent to cells [17–19]. Properties of these crystals can be found in Table 1-1.

Table 1-1 Properties of calcium oxalate hydrates

Property	Calcium oxalate monohydrate	Calcium oxalate dihydrate
Formula	$\text{CaC}_2\text{O}_4 \cdot \text{H}_2\text{O}$	$\text{CaC}_2\text{O}_4 \cdot 2\text{H}_2\text{O}$
Unit cell structure	Monoclinic	Tetragonal
Space group	$P2_1/c$	$I 4/m$
a (Å)	9.976	12.371
b (Å)	14.588	12.371
c (Å)	6.291	7.357
β	107.05°	
CAS number	5794-28-5	25454-23-3

1.2.1 Calcium Oxalate Monohydrate Crystals

COM crystals are the most abundant form of mineral in kidney stones and are the most thermodynamically stable form of calcium oxalate under physiological conditions. They have a monoclinic structure with a unit cell (Figure 1.7a and b) of dimensions $a = 9.976 \text{ \AA}$, $b = 14.588 \text{ \AA}$, $c = 6.291 \text{ \AA}$, and $\beta = 107.05^\circ$ [20]. Synthetic crystals formed for research purposes are usually in the form of single crystals, contact twins or penetration twins [21]. Other than being a physiologically relevant crystal, COM is also a very suitable choice for peptide-ion interaction studies as they have two very contrasting faces, one Ca^{2+} rich and highly positive, and other oxalate rich and highly negative, namely $\{100\}$ and $\{010\}$ respectively [20]. It has been observed that (100) penetration twinning as shown in Figure 1.7c is much more frequent among synthetic crystals.

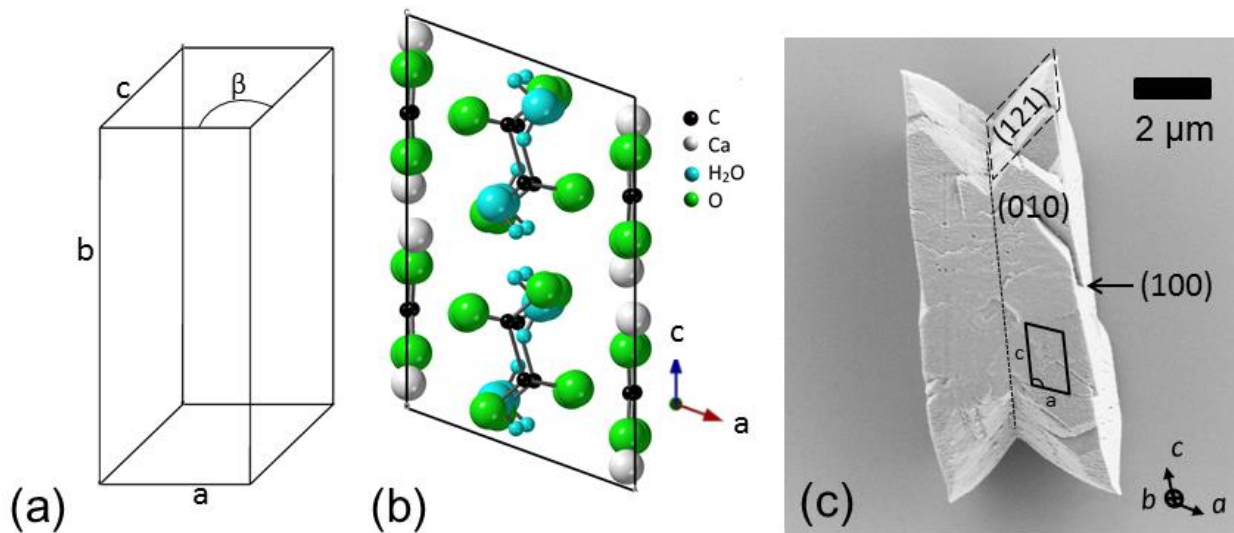


Figure 1.7. (a) Schematic of the unit cell of the COM crystal. (b) (010) face of the unit cell with atom positions. (c) SEM image of a COM crystal, with faces indicated. The dotted line represents the twin plane.

1.2.2 Calcium Oxalate Monohydrate Inhibition

Growth of COM crystals *in vivo* is affected by the contents of urine and the presence of naturally occurring macromolecules. For instance, osteopontin (OPN) and Tamm-Horsfall glycoprotein

(THP), both of which are rich in aspartic acid and glutamic acid, play an important role in controlling stone formation [22], and also promote formation of COD rather than COM [23]. The inhibition of COM has been studied by various methods, including constant composition analysis, in which the ion concentration in solution is monitored to maintain a constant composition during the experiment [1], scanning confocal interference microscopy [24] and atomic force microscopy. Atomic force microscope (AFM) studies have shown the transition of straight steps to curved steps due to the introduction of inhibitors to the system, as expected by the Cabrera-Vermilyea model [10]. Previous work using the AFM has shown that the $\{010\}$ face has growth hillocks bound by steps in the $[120]$ and $[121]$ directions. Figure 1.8. shows an AFM image of $\{010\}$ face of COM crystal indicating the main step directions. The $\{100\}$ face does not exhibit well defined growth hillocks [25]. Each step of the hillock is made of a terrace which has the same Miller index as the face, and a riser, which is an atomic plane at an angle to the terrace aligned along the step. Steps on $\{100\}$ and $\{010\}$ faces have step risers with $\{121\}$ and $\{021\}$ faces as shown in Figure 1.9 [26]. In principle, inhibition of growth could occur due to an inhibitor adsorbing to the terrace, riser or both.

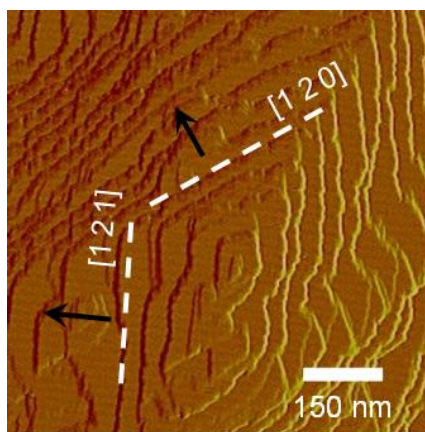


Figure 1.8. AFM deflection image of a growth hillock on a $\{010\}$ face of a COM crystal. Arrows show the growth direction of propagation each step.

In vitro studies performed by De Yoreo et al. have examined the effects of the presence of OPN on the $\{010\}$ and $\{100\}$ faces of COM. The results have shown major morphological modification on $\{010\}$ but little effect on $\{100\}$ faces [13,25,26]. This difference in degree of inhibition is due to face-specific OPN interactions. The OPN molecules interact weakly with the steps on $\{100\}$ faces and thus cause little or no change. Contrarily it was observed that $\{010\}$

faces consists of quadruple steps rather than the single steps seen on $\{100\}$ faces, suggesting that greater height facilitates binding of OPN to the step riser and the basal plane, leading to stronger inhibition [13,25].

Citrate ($C_6H_8O_7$), a small organic anion with three carboxyl groups, binds preferentially to $\{100\}$ faces relative to $\{010\}$ faces [25,27]. Binding is determined by the orientation of the oxalate group on the surface and the configuration of the calcium sites on the crystal. On $\{100\}$ faces, the flat orientation of the oxalate groups on the surface promotes binding by allowing more access to calcium ions, so that citrate can get closer to the calcium ions and the configuration of calcium sites accommodate all carboxyl groups in citrate. In contrast, on $\{010\}$ faces, oxalate ions are exposed and oriented orthogonal to the (010) plane, making it difficult for the citrate molecules to bind to the crystal due to electrostatic repulsion. There is a striking contrast between the inhibitory effect on $\{100\}$ and $\{010\}$ faces due to this specific interaction [25,27,28].

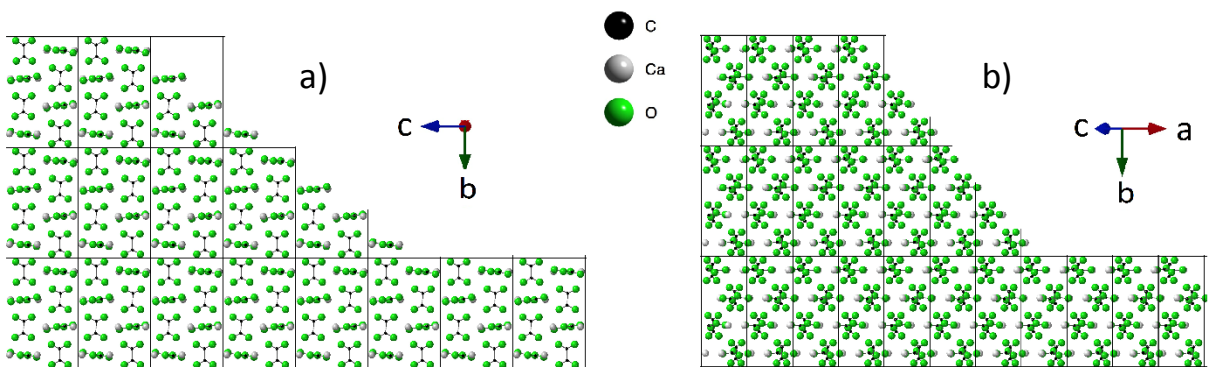


Figure 1.9. Cross-sections of the two main growth directions on $\{010\}$ face. Water molecules are not shown for simplicity. a) $[120]$ step with (021) plane as the riser. b) $[121]$ step with (121) plane as the riser.

OPN combined with citrate have achieved additive inhibitory effects by pinning step motion on different faces. At the same time, higher concentrations of OPN promote the formation of COD crystals by inhibiting COM crystals, which reduces the incidence of kidney stones since COD crystals are easily excreted in urine [27].

The effects of synthetic peptides comprised of sub-sequences of OPN on the growth of COM have been previously studied by Grohe et al. using confocal microscopy and molecular dynamics simulations. Exact contents of the protein used in experiments depends on the tissue of origin and the species its derived from. OPN synthesized from rat bone, is a molecule with an average phosphate content of 10 per molecule and 29 sites that can add phosphate (phosphorylated) to the molecule [29]. These phosphate groups in OPN contribute largely to the crystal inhibitor interactions [30]. In one molecular dynamics study, a peptide consisting of amino acids 220-235 of rat bone OPN (P3), one of several highly phosphorylated aspartic acid rich sequences found in the protein, was investigated (Table 1-2). The results suggested that the phosphate groups in the sequence provide a strong negative charge that causes closer and stronger interactions with the Ca^{2+} rich {100} face of the crystal [31]. Hug et al. focused on inhibition by a phosphorylated peptide sequence corresponding to amino acids 65-80 of rat-bone OPN, which we term pOPAR. Measurements of the crystal dimensions revealed that pOPAR inhibits growth of faces differentially in the order {100} > {121} > {010}, with the {100} face displaying the highest inhibition [32]. In the same study, molecular dynamic simulations were performed on {121} risers on {100} terraces and {121} risers on {010} terraces. Results showed that pOPAR binds to the {100} terrace very rapidly, whereas binding on {010} terraces occurs preferentially to {121} step risers rather than directly to the {010} terrace [32]. It was also found that inhibition by pOPAR is rapid relative to the time required for recovery to an uninhibited state after pOPAR is removed [33].

Table 1-2 Phosphorylated peptide sequences derived from OPN. The main amino acids in the sequences are serine (S), aspartic acid (D) and glutamic acid (E) (see Appendix C for more details).

Peptide	Sequence
pOPAR	pSHDHMDDDDDDDDGDD
P3	pSHEpSTEQSDAIDpSAEK
HHS	HHpSDEpSDESFTASTQA
DVL	DVLTPIAPTVDVPDGR

Most of the natural proteins that are known to affect COM crystal growth contain 10 – 40% aspartate and glutamate residues [34] suggesting that synthetic polyaspartic acid (poly-ASP) will be an effective inhibitor of COM crystallization. As poly-aspartic acid is known to be more effective at inhibiting growth than its monomer [35], synthetic poly-ASP chains behave as surrogate molecules to explore the inhibitory effects of aspartic acid domains in macromolecules. Constant composition studies and AFM studies done by Wang et al. [36] revealed that interspersing other amino acids into the poly-ASP chain has a significant effect on COM nucleation and growth. For instance, peptides in which every fourth aspartic acid monomer was substituted with serine resulted in more effective inhibitors than peptides with every fourth aspartic acid monomer substituted with glycine.

Many models of growth and step kinetics have been developed to explain crystal growth inhibition. For instance, a step kinetic model developed by Weaver et al. explored the kinetic effects of inhibitor adsorption, diffusion and incorporation on step velocities [37]. This model is a version of the C-V model, reformulated by taking into account impurity adsorption and kink density, to explain the discrepancies between experimental results and the C-V model. The proportionality between impurity coverage and solution impurity concentration and dependency of the dead zone on impurity concentration are among the corrected terms. The model assumes that the kinetic coefficient, which is a measure of above-mentioned kinetic effects, changes with poisoning of kink sites, which leads to reduction in the density of active kink sites. They conclude that some fraction of impurities adsorbed to the surface, slowing the steps by merely deactivating kink sites temporary by occupying them, without pinning the steps as postulated by the C-V model.

Cho et al. analyzed the effect of a pair of six-residue linear aspartic acid molecules, that have L and D chirality and are mirror images of each other (enantiomers) on COM crystal growth and applied the step kinetic model to understand the mechanism of inhibition. By successfully fitting the model to the velocity variation with aspartic acid concentration, they showed that the major effect of these polymers is to poison kink sites and reduce kink site density, which reduces the kinetic coefficient for step growth. Analyzing the fitting parameters of the study revealed that the level of inhibition is due to a high level of adsorbed poly-ASP molecules to the terrace of the crystal. Using adsorption /desorption parameters, the binding energy difference was estimated to

be 9 kJ mol^{-1} between the two faces $\{100\}$ and $\{010\}$. Molecular modeling shows that the reason for the difference in binding energy between the $\{100\}$ and $\{010\}$ faces is a result of the difference in arrangement of calcium and oxalate on faces [38].

Scanning confocal interference microscopy (SCIM) was first used by Grohe et al. to analyze the formation of COM in the presence and absence of poly-ASP. In this study, the increasing poly-ASP concentration led to irregular growth shapes, an increase in the population of COD, and an increase of nucleated crystal number density [39].

In this study we focus on the $\{010\}$ faces of COM crystals as they are known to show inhibitory effects with both macromolecules and small anions. Most of the studies point to the fact that small anions show preferential binding to $\{100\}$ faces over $\{010\}$ faces. However, binding of anions to the step risers on $\{010\}$ are expected to be favorable. This combined with the fact that $\{010\}$ faces consist of clean growth hillocks, makes $\{010\}$ faces a good platform to study effects of impurities on COM crystals.

1.2.3 Calcium Oxalate Dihydrate Structure

Unlike COM crystals, COD crystals can be found in both healthy and stone formers' urine and are usually easily excreted [18,19,40]. COD forms bipyramidal crystals with a tetragonal unit cell structure (Figure 1.10a and b) with lattice dimensions of $a = b = 12.371 \text{ \AA}$, and $c = 7.357 \text{ \AA}$ [41,42]. They may exist in urine as octahedral crystals (Figure 1.10c), which is the most common form, or as dodecahedral crystals [2]. COD crystals can be present as small or large octahedral crystals with sizes ranging from 1 to 50 \mu m , or elongated rod-like dodecahedral crystals, which can form large aggregates harmful to the kidney [2,43]. Numerous studies have been performed comparing formation and inhibition of COM and COD crystals. Studies have shown that COD crystals have less adherence to the cell surface than do COM crystals, and that they are less injurious to the cell membrane [44]. A study by Lieske et al. suggested that there is a preferential molecular interaction between $\{100\}$ faces of COD and the plasma membrane of the kidney [45]. Moreover, it is also known from previous studies that once nucleated, the COD crystals will pass into urine before achieving a larger size and forming stones [2]. However, when they aggregate with other crystals, they can be quite harmful.

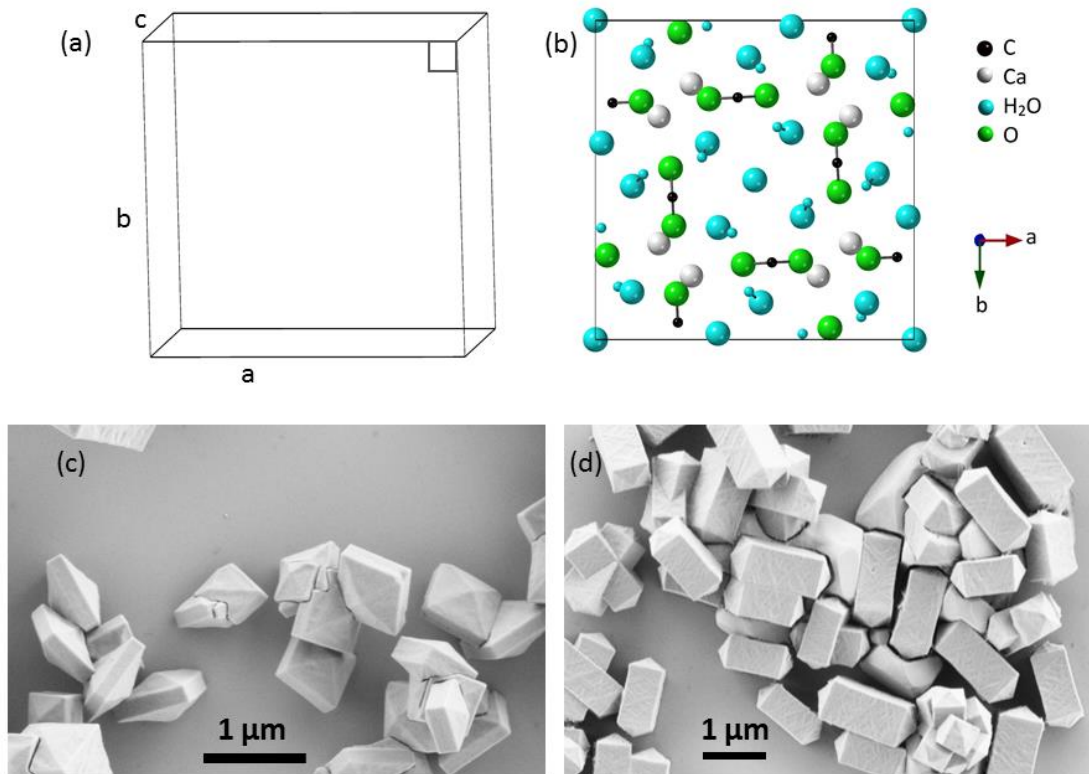


Figure 1.10 Crystals structure and SEM images of different types of COD crystals. (a) Schematic of the unit cell of the COD crystal. (b) (100) face of the unit cell with atom positions. (c) Octahedral COD crystals. (d) Dodecahedral COD crystals.

As the most thermodynamically stable form of calcium oxalate under physiological conditions is COM, this phase must be suppressed to promote the growth of COD for experimental purposes. Jung et al. used poly-acrylic acid to inhibit COM, allowing COD to form. Increasing the concentration of poly-acrylic acid changes the morphology of COD from tetragonal bipyramids with dominant $\{101\}$ faces to tetragonal bipyramids mixed with flat prism faces to elongated tetragonal bipyramidal prismatic (dodecahedral) crystals with dominant $\{100\}$ square faces as shown in Figure 1.10d [46]. For this reason, different concentrations of poly-acrylic acid can be selected for preferred formation of specific crystal faces [47].

As COD crystals are less damaging to the kidney cell membrane and are rapidly excreted from the urine [44], existence of COD crystals in the system is of special interest to the health care industry. OPN and its peptides have been proven to inhibit COM and promote COD [17,48]. For instance, a study by Grohe et al. explored the effects of OPN peptides on COM inhibition

and COD formation in filtered and sterilized urine and concluded that COD formation is controlled by the phosphorylated aspartic acid-rich regions of OPN [48].

Another extensive study was conducted by Chan et al. to investigate the effects of synthetic peptides of rat bone OPN on the formation of COM and COD. The study investigated the roles of acidity, hydrophilicity and phosphate/carboxylate-containing peptides on crystallization of COD and included peptides with net negative charge and one with net positive charge. This revealed a trend where increasing the net negative charge of the peptides is correlated with the amount of COD precipitation. pOPAR, which is a phosphorylated peptide, stands out in promoting COD among other peptides. Intriguingly, one basic peptide (OPN129–144 termed GDS) also induced COD precipitation [49].

1.2.4 Calcium Oxalate Dihydrate Inhibition

Even though COD formation is medically preferred over COM in regard to kidney stone formation, its inhibition and prevention is a topic of interest in both kidney stone research and in crystal growth studies. Stones made of dodecahedral COD crystals and small octahedral crystals can be observed in people with heavy to moderate hypercalciuria which is the condition of elevated calcium in urine [2].

Early studies of the inhibition of calcium oxalate dihydrates explored the effects of Tamm-Horsfall protein (THP) and nephrocalcin (NC), both of which are acidic glycoproteins [50]. In the case of NC, it was concluded that the crystal growth inhibition is controlled by highly selective bonding with {100} faces.

These faces have a highly planar arrangement with two layers of oxalate ions, one layer with oxalate ions coplanar to the surface and the other with oxalate ions normal to the {100} face [51]. This unique arrangement of oxalate ions promotes binding of the crystal face with calcium associated with NC. A similar arrangement can be observed in COM {100} faces [45,51,52]. On the other hand, THP shields the crystal surface from oxalate ions impeding oxalate ions in the solution from reaching the crystal-solution interface. This effect increases when the THP concentration is raised and is more prominent in solutions with high calcium concentration, which causes THP molecules to form a gel [20,45].

Even though there have been many studies of COM crystal growth, there is limited microscopic information on COD growth and inhibition. Jung et al. explored the effects of macromolecular additives such as poly-L-aspartic acid, poly-L-glutamic acid and poly acrylic acid (chemical structures are shown in Figure 1.11) on COD faces in real time using the AFM.

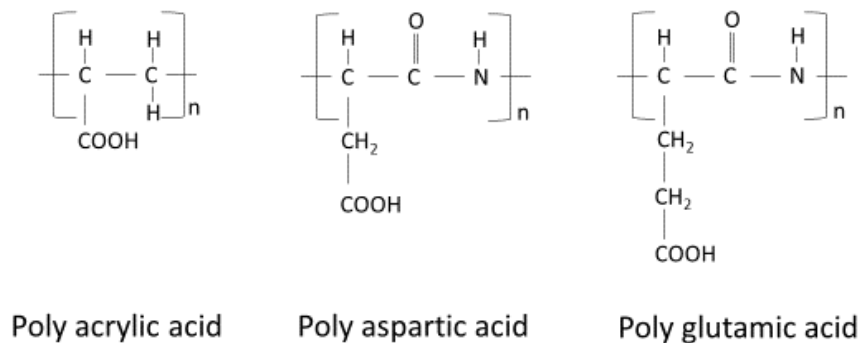


Figure 1.11 Chemical structures of amino acids used on COD growth and inhibition.

They showed that increasing additive concentration leads to a change in stone shape from octahedral to rod like and finally into a dumbbell shape [41]. The change in the crystal shape was explained as the result of preferential interaction of the above polymers with {100} faces due to the higher Ca^{2+} density ($0.0440 \text{ ions}/\text{\AA}^2$) than on {101} faces ($0.0125 \text{ ions}/\text{\AA}^2$) [41,47]. All inhibitors studied on COD inhibited the growth of {100} faces to a higher degree than the {101} faces, making the triangular {101} faces grow faster than {100} faces, resulting in a large rectangular {100} face elongated along the c-axis.

These macromolecules with anionic side chains caused inhibition of growth on both {101} and {100} faces. While the data acquisition was difficult for Jung et al. on {101} faces, the {100} face displayed well defined elliptical growth hillocks elongated along the b-axis [35,47]. Addition of all three polymers slowed the advancement of steps aligned with the [001] direction (with the growth direction [010]) significantly, while steps aligned with the [010] direction (with the growth direction [001]) were less affected. Step velocities measured along these steps show that the velocity decrease of the [001] step is greater than that of the [010] step. This suggested

that the polymers adsorbed to steps along the [001] direction more than to the steps along [010] direction [47]. The resulting shape of the inhibited hillocks was more circular than elliptical.

Another study by Grohe et al. analyzed the formation of calcium oxalate crystals in the presence and absence of poly-aspartic acid using scanning confocal interference microscopy (SCIM) and AFM. Results of the study showed that the presence of poly-aspartic acid promoted precipitation of COD crystals and increasing polymer concentrations led to decreased growth rates along [110] directions [39].

A recently developed class of crystal growth modifier, double-hydrophilic block copolymers, has been used to modify COD growth by Zhang et al. These polymers consist of one hydrophilic block intended to interact strongly with inorganic material surfaces and another hydrophilic block that does not interact with the surface but promotes solubility of the polymer in water [53]. It was observed that the presence of this polymer favors the morphological transition of COD crystals from tetragonal bipyramids to elongated tetragonal prisms dominated by {100} faces [54].

1.3 Experimental Techniques

1.3.1 AFM Studies

The atomic force microscope (AFM) has made possible direct imaging of nucleation and crystal growth events at the microscopic, and even near-molecular, level [6]. The atomic force microscope probes the surface of a sample with a sharp tip a few micrometers long and with a tip radius often less than 5 nm. The tip is located at the free end of a cantilever beam that is 100 to 200 μm long. Forces between the tip and the sample surface cause the cantilever to deflect. A piezoelectric scanner is used to move the sample relative to the tip in three directions. A laser beam reflected off of the cantilever to a detector measures the cantilever deflection as the tip is scanned over the sample, or the sample is scanned under the tip.

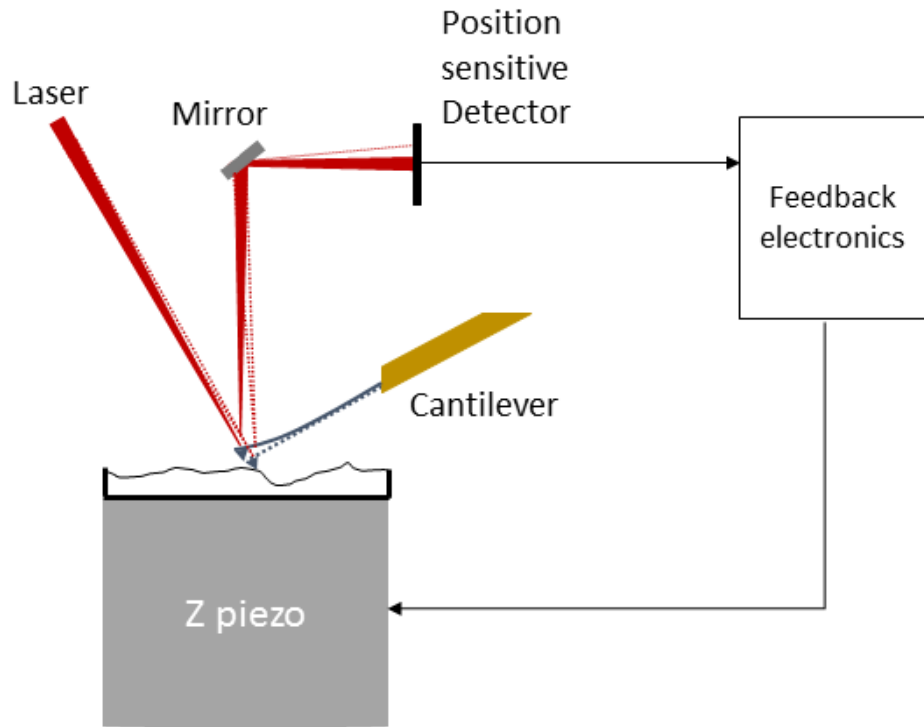


Figure 1.12. Schematic diagram of the atomic force microscope.

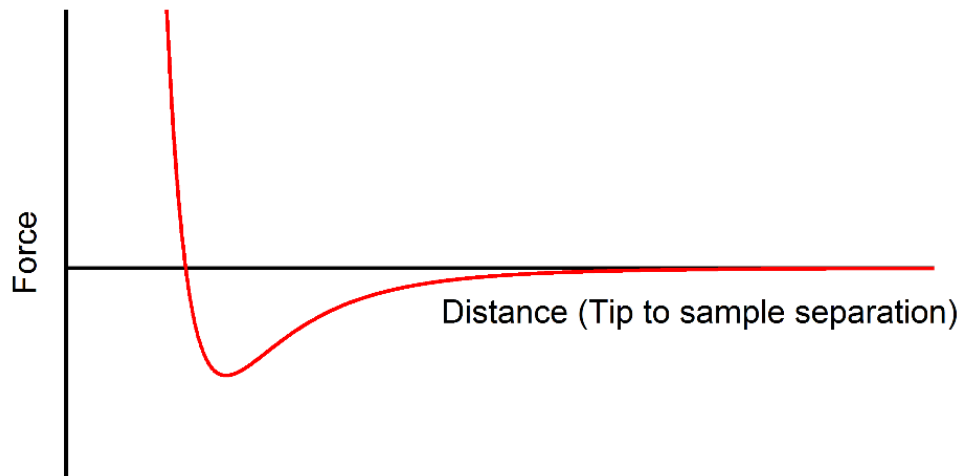


Figure 1.13. Variation of force relative to the distance between tip and the sample.

The general dependence of the tip-sample interaction on the distance between tip and sample is illustrated schematically in Figure 1.13. Two distinct regions, contact and non-contact, represent the distances at which repulsive and adhesive forces dominate the interaction between the atoms of the tip and the sample. In contact mode, the tip makes ‘physical contact’ with the sample. As the scanner moves the tip across the sample in contact mode, repulsive short-range forces, which act normally to the surface, induce a deflection of the cantilever. The topology of the surface will cause changes in the cantilever deflection while scanning, resulting in a change in position of the reflected laser beam as shown in Figure 1.12. The deflection signal is compared to a user-defined set point. A feedback circuit is used to move the scanner up and down along z direction under the tip so that the deflection is returned to the defined point. As a result, a constant force is maintained during scanning (aside from momentary fluctuations). This movement of the scanner, necessary to maintain a constant deflection, is mapped to generate a height map of the sample. The momentary delay in the response of the scanner height to a changing deflection signal leads to a momentary error in the feedback loop. The “deflection image” is a map of this error. These two images, height and deflection, provide information about the surface.

1.3.2 AFM on Crystal Growth

The AFM has the ability to image in air, vacuum or fluid. The ability to obtain quality images in fluid permits nanoscale investigations of crystal nucleation, growth and inhibition directly in the environment of interest. Before the invention of the AFM, theories such as crystal growth via the screw dislocation mechanism proposed in 1951 by Burton and Cabrera [55] were only observed *ex-vivo*. With the ability to image in fluid environments, the AFM has provided more relevant images *in situ*. Consecutive images gathered during an experiment can easily be assembled in the form of a movie, providing visualization of the dynamic phenomenon. The AFM is the only tool that allows real-time *in situ* investigations of growth at length scales ranging from the molecular level to 100 μm faces [56].

For the past three decades, AFM studies of crystallization have been performed on many systems. Some examples are protein crystals such as lysine, canavalin and insulin, inorganic materials such as different forms of biomineral calcite, and calcium oxalate [57]. A benefit of *in situ* AFM is the ability to gather kinetic data, as well as topographical information, over a user

defined area. It can acquire scans with a short time interval between each frame, by scanning rapidly over the surface which in turn can be used to quantify kinetic data such as step speed and growth rate of the surface. These scans provide the opportunity to compare a model with physical data. For example, a proposed mechanical model for interactions between a crystal surface and a protein can be directly compared to step speed data and morphology. This permit nanoscale investigations of crystal nucleation, growth and inhibition [58,67]. Studies conducted with the AFM on crystal growth have enabled investigations of crystal growth mechanisms and the role of inhibitors on growth rates and crystal formation [1,13,22,25].

Studies of COM crystallization using the AFM have been performed to obtain a better understanding of the mechanism of crystal nucleation and growth. Different faces of COM and their individual step directions were identified using the images from the AFM [11,13,25]. De Yoreo et al. has introduced aspartic acid rich peptides such as THP and OPN to COM crystal faces and studied the change in morphology on COM faces with the aid of AFM. They have observed that the {100} faces only have single elementary steps (height =3.98 Å), while {010} faces have double and quadruple steps as well. These steps allow the proteins that are too large to interact with a single step to adsorb to the crystal surface and modify growth [13,25].

Friddle et al. has looked at COM growth and inhibition by aspartic rich peptides, at single molecule resolution using the AFM. This has provided real-time images of inhibitor molecule interactions with crystal steps, and the resultant morphology changes [58].

Experiments on crystal growth with the AFM can be enhanced with accessories that facilitate the ability to precisely control temperature, pH level, flow rate and composition of the solution and the capability to change solution while imaging.

Crystallization is an important field of study since many natural and industrial materials are crystalline. The effect of impurities on crystallization is of interest both for the control of crystal morphology and for the prevention of undesired crystals, such as human kidney stones. The atomic force microscope allows us to study the growth of calcium oxalate crystals, the main mineral component of kidney stones, in real time and at high resolution in the presence of protein sequences known to inhibit their growth. We find that these inhibitor molecules decrease the propagation rate of growth steps on faceted crystal surfaces, in agreement with the general

consensus that inhibitors adsorb to growth surfaces, forcing advancing steps to curve, thereby decreasing the effective supersaturation. However, we find that the decreased step velocity is strongly dependent on step direction, indicating that the inhibition mechanism involves adsorption to steps, not merely terraces. This may be useful for the development of better therapeutic measures to prevent the formation of kidney stones, and may be important for an increased understanding of the inhibition of crystallization in general. In addition, we find that the act of imaging by atomic force microscopy can increase the growth rate in the presence of kinetic inhibitors, presumably by removing inhibitor molecules from the surface. Quantifying this effect is important for the interpretation of real-time atomic force microscopy of crystal growth.

2 Materials and Methods

2.1 Solution Preparation

Calcium oxalate solutions were prepared using two separate calcium (Ca^{2+}) and oxalate ($\text{C}_2\text{O}_4^{2-}$) ion stock solutions. Calcium stock solution was comprised of calcium nitrate, and oxalate stock solution of sodium oxalate, both with 5.88 mM concentration and also containing 0.4412 M sodium chloride concentration according to the recipe in Appendix A. All solutions used deionized water purified with a Milli-Q water system. These solutions were mixed in equal parts, and further diluted to produce 1 mM calcium oxalate solution for initial nucleation of crystals. For growth solutions, stock solutions were diluted to attain calcium oxalate concentrations varying from 0.2 mM to 0.6 mM. For example, 0.3 mM solution, commonly used to achieve steady state growth, is made by mixing 255 μl of calcium and 255 μl of oxalate solution with 4490 μl of deionized water, resulting in a 5 ml of 0.3 mM growth solution. For all solutions, sodium oxalate ($\text{Na}_2\text{C}_2\text{O}_4$), calcium nitrate ($\text{Ca}(\text{NO}_3)_2 \cdot 4\text{H}_2\text{O}$), sodium chloride (NaCl), and anhydrous sodium acetate (CH_3COONa ,) were used as purchased from Sigma-Aldrich.

2.2 Crystal Sample Preparation

To prepare crystal samples, COM crystals were nucleated from 1 mM calcium oxalate solution on glass cover slips (12 mm, Ted Pella, Inc.) in tissue culture plate wells (24 well, BD Canada). First, 170 μl of 5.88 mM calcium stock solution was added to the wells followed by 660 μl of deionized water. Then, 170 μl of 5.88 mM oxalate stock solution was added to each cell while stirring the solution with pipette tip to provide a uniform concentration in the final solution. The well plate was then left undisturbed for three hours to permit nucleation. In the process of making COD samples, each cell was mixed with poly-acrylic acid to suppress COM formation and promote COD. Further details are included in Chapter 4.

After three hours, the walls of the well and the glass cover slip were lightly scraped with a clean metal spatula to dislodge crystals into the solution. Solutions were then filtered through polycarbonate membrane filters with a 0.8 μm pore size (Spi supplies/Whatman) using a plastic Swinny filter holder (Pall Corp.). Filter papers with the collected crystals were then dried in an oven at 70 °C. Silicon pieces cut from an undoped polished Si wafer were coated with a thin layer of UV-curing adhesive (Norland Optical Adhesive NOA 81, Norland Products, Inc.) and

partially cured with a 6 W UV light for 10 s. This layer of glue must be applied as a very thin layer to avoid crystals submerging in glue during the next step. This was achieved by rubbing two Si wafers together (polished sides) with the minimum amount of glue between them and separating by sliding one piece across the other. Once the crystals were dry, they were transferred to the Si pieces by lightly pressing the filter papers to the partially cured surface. The adhesive was further cured for 15 minutes under UV light to completely set the glue.

2.3 Peptide Preparation

Polymers and peptides needed for the experiments were prepared as freeze-dried aliquots. In order to do that, either 1 mg or 5 mg of the peptide is dissolved in 1 ml distilled water. Then aliquots of 50 μ l were dispensed into microfuge tubes, and stored overnight at -80 °C. Aliquots are then freeze dried before sending one aliquot for amino acid analysis (Institute for Biomolecular Design, University of Alberta, or Advanced Protein Technology Centre, Hospital for Sick Children, Toronto) to determine the exact amount of polymer or peptide in the tube. Completely processed aliquots can be stored in a freezer for a few years and reconstituted into solution again with distilled water, when needed. Polymers such as poly-ASP, e.g., poly (L-aspartic acid sodium salt) (Alamanda polymers) with lengths ranging from 10 to 200 amino acid residues were also used as crystallization modifier. Short peptides derived from the macromolecule OPN were prepared in a similar method for the COD experiments.

2.4 AFM Imaging

Crystal growth was imaged in real time using a Multimode AFM with Nanoscope V controller (Bruker) equipped with a glass fluid cell. Samples were mounted on to 12 mm AFM specimen discs (Ted pella, INC) using glue (Krazy glue). Scanning was performed in contact mode at 25–40 lines/s using silicon nitride cantilevers (Bruker) with spring constants ranging from of 0.03 N/m to 0.06 N/m. AFM tips with specifications listed in Table 2-1 below were used.

Table 2-1 Spring constant and the tip radius of the AFM tips

AFM tip	Spring constant (N/m)	Tip Radius (nm)
DNP –S	0.12	10
MSNL-W	0.03	2
SNL-10	0.12	2

2.4.1 Imaging in Fluid

Supersaturated calcium oxalate solution was introduced to the fluid cell from a plastic syringe using flexible polymer tubing (1/16 inch, Tygon). To compensate for the depletion of the concentration of calcium oxalate in the fluid cell due to crystal growth, the solution in the fluid cell was replaced by fresh solution every 5 min. We verified that the growth rate remained constant to within 10% between injections fresh solution [13]. This flushing also gave us the ability to rapidly change from growth solution to inhibited solution without interrupting the imaging.

2.4.2 Inline Mixing with a Syringe Pump

A constant supersaturation can be maintained by continuous flow of solution through the fluid cell using the experimental setup illustrated schematically in Figure 2.1. This was achieved using a dual syringe pump (Legato 270p), which allows infusion into, and withdrawal from, the cell simultaneously by a drive step motor. The pump can be fixed with two syringes for infusion and two syringes for withdrawal. Two 20 ml syringes filled with calcium and oxalate solution with twice the concentration needed for the experiment were fixed on the infuse part of the pump. Polymer tubes leading out from them were joined together with a T connector halfway from the fluid cell. This way, calcium and oxalate solutions are mixed well in the tubes before injected into the fluid cell, providing a uniform concentration within the cell. Withdrawal of solution was accomplished by two 20 ml empty syringes and tubes filled with water (to avoid creating a vacuum in the tubes) leading from cell to the pump.

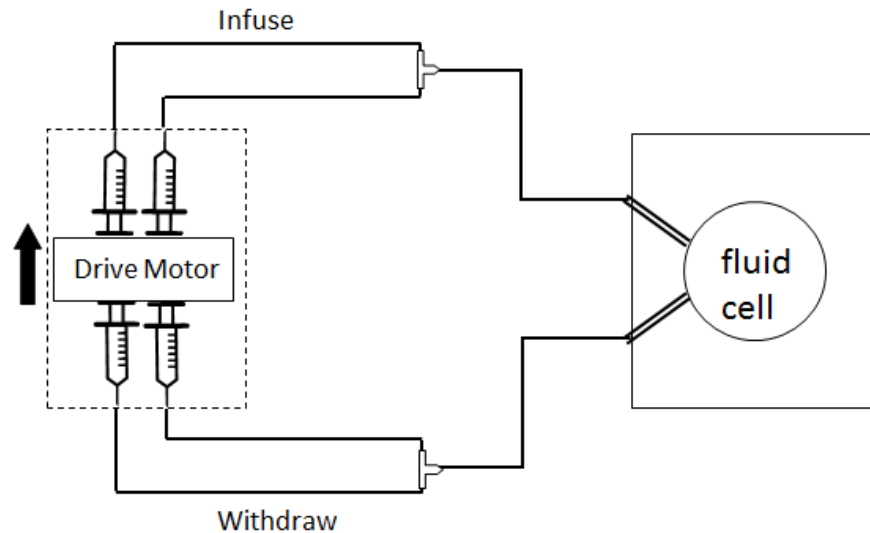


Figure 2.1. Schematic of a typical experimental set up with in-line mixing using a dual syringe pump.

In order to avoid disturbances due to the flow to the AFM tip, a slow rate of 5 ml/hr was used. This provides $1.4 \text{ mm}^3/\text{s}$ flow rate in the cell and $4.63 \times 10^{-4} \text{ m/s}$ velocity across the cell. This flow rate was slow enough to create minimum disruption to images but fast enough to avoid depletion of ions in the cell (see Appendix B). An o-ring is used to seal the fluid cell to contain the solution and to prevent air bubbles. To prevent possible leaks, the sample must have bigger dimensions than the diameter of the o-ring used. A synthetic polymer grease (multi-purpose synthetic grease, Super Lube[®]) was used around the o-ring to improve the seal while being careful to use the minimum amount of grease needed. Once the fluid cell with greased o-ring was lowered onto the sample, the fluid cell was flooded with solution by starting the pump. As the last step of the setup, the system is checked for proper withdrawal of solution and lack of air bubbles. The pump can be paused to stop the flow to eliminate any minor disturbances to obtain a high-resolution image if needed. Once the experiment is underway, the system was continuously monitored for leaks and air bubbles.

2.5 Movies and Velocity Calculations

2.5.1 Drift Correction

During imaging, the apparent sample location tends to drift slightly due to creep in the glue used to mount samples to AFM studs or compressing relaxing of the o-ring. The cantilever and the AFM scanner can be susceptible to external temperature changes [57]. We compensated for this by registering successive frames to a common feature and using the Igor pro software (WaveMetrics Inc.) with an in-house macro to offset images. The macro loads the AFM images and allows the user to click on a feature that is common in all frames. The offset of the location of this feature compared to the location of the first frame is recorded for each frame. The images offset in this way were then combined into a movie, to facilitate observations of the progression of steps on the surface. Because AFM images are acquired line-by-line, the apparent step direction is usually distorted. To avoid the effect of inevitable step distortion due to motion during the acquisition of a frame, we used alternate frames with a consistent scan direction (frame up or frame down). This way the change in the step direction will be common to all images and will not affect any observations or calculations.

2.5.2 Calculating Velocity

Step velocity can be determined by measuring the position of an individual step through several frames. Other research groups have used this method of calculating step velocity when step edges are well defined and can be tracked relative to a fixed feature in the image [13,14]. Figure 2.2 shows three alternate frames (spanning six frames acquired over 55 s) in which a single step is tracked. During velocity calculation, a line is drawn perpendicular to the steps and a single step is tracked along this line in each frame. A single point is selected along the step and the macro record the perpendicular point along the line that is drawn in the beginning. This is carried out using a freeware image processing software ImageJ (NIH, USA). The time elapsed between each of these step positions can be calculated from the scan rate and the resolution of the image using the equation,

$$\text{time elapsed} = \frac{2 \times \text{resolution}}{\text{scan rate}}. \quad 2.1$$

Once the displacement of the step relative to the previous frame is extracted from the macro, velocity is calculated.

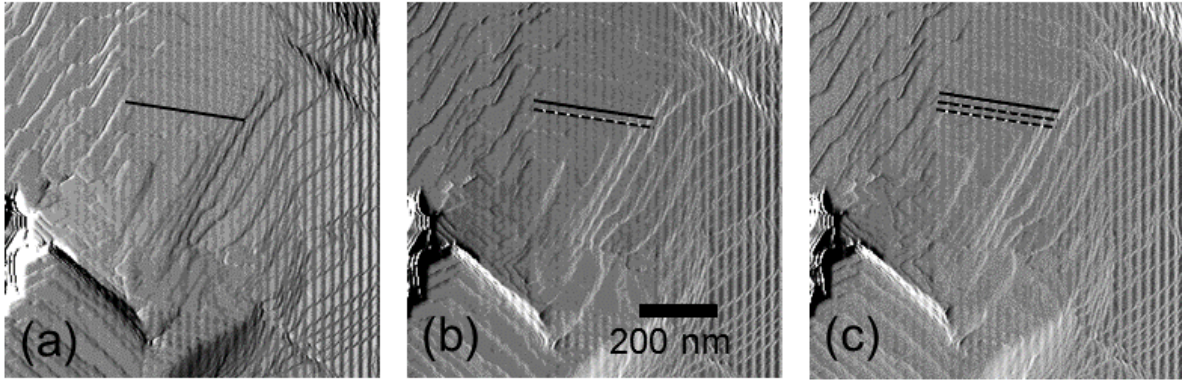


Figure 2.2. Alternate AFM deflection image of a growth hillock on a $\{010\}$ face of a COM crystal showing an advancing step. The dashed lines in (b) and (c) show previous positions of the step, while the solid line shows its current location.

3 Directional Pinning of Calcium Oxalate Monohydrate Crystallization by poly (aspartic acid)

3.1 Motivation/ Importance

Kidney stone disease, a painful condition that can lead to renal failure, afflicts more than 10% of the human population [42]. The major components of kidney stones are calcium oxalate crystals, which aggregate to form stones in urine. Calcium oxalate in kidney stones is typically found in one of two crystalline forms, each with a different ratio of water: calcium oxalate monohydrate (COM) and calcium oxalate dihydrate (COD) [2]. As COM crystals are the most abundant form of calcium oxalate crystals in kidney stones, understanding their formation and prevention is important to the development of therapeutic treatments.

The morphology of a faceted crystal is governed by the relative surface energies and growth rates of its facets [7]. It is possible to modify the shape of the crystal by introducing ions or molecules that alter the relative growth rates of different faces through interactions with step edges [8]. Such agents are called kinetic inhibitors and affect crystallization kinetics without changing the thermodynamics of the system. In other words, these additives do not change the phase diagram of the system.

As described in Chapter 1, the accepted model for the step pinning mechanism by which kinetic inhibitors affect crystal growth and morphology was described more than 50 years ago by Cabrera and Vermilyea [10]. The “C-V” model suggests that molecules that adsorb strongly to a growth surface will pin the advancing steps when they encounter the adsorbed molecules. Steps must then curve around the pinning sites for growth to proceed, reducing the supersaturation via the Gibbs-Thompson effect. When the spacing λ between the impurities is less than twice a certain critical radius r^* , growth will be arrested completely since the curvature required for step flow reduces the supersaturation to zero. Several AFM studies have shown a transition from straight steps to curved steps due to the introduction of inhibitors to the system [59].

It is well known that several urinary proteins are able to modify calcium oxalate growth. Many of these proteins, particularly osteopontin (OPN) and Tamm-Horsfall glycoprotein (THP), have domains rich in aspartic acid [34]. These aspartic acid domains provide carboxyl groups that

interact with the surface Ca^{2+} ions on crystal faces [1,25,38]. Synthetic polymers and polypeptides are also able to modify calcium oxalate growth [26]. For instance, poly(aspartic acid), referred to here as poly-ASP, chains are known to be more effective at altering crystal growth than the aspartic acid monomer on its own [60]. L. Wang, et al., observed that other amino acids incorporated as spacers in the peptide sequence can enhance the effects of poly-ASP on nucleation and growth of COM. For example, using serine as a spacer has a greater effect on crystallization than does glutamate [1]. Grohe et al. analyzed the formation of COM with and without the presence of poly-ASP. Their study revealed that increasing the amount of poly-ASP leads to irregular growth shapes, a higher population of COD crystals and smaller COM crystals [39].

This chapter presents a study of the effects of poly-ASP on {010} faces of COM crystals using the atomic force microscope (AFM) and introduces a simple model for adsorption of inhibitors to steps. Different molecular weights of poly-ASP are introduced to supersaturated growth solutions and the results are observed on {010} faces. We observed that poly-ASP inhibits different growth directions by different amounts. This directional pinning forms “finger like” features on the crystal surface. It was also seen that at low poly-ASP concentrations, growth continues in other directions between pinning sites. There is a threshold inhibitor concentration for these features to appear, which varies with the length of the polymer. Differential inhibition of steps observed in the study is not expected for the C-V model with adsorption to terraces. Developing a model to describe the directional pinning and the threshold concentration distribution can shed light onto inhibition mechanism.

3.2 Materials and Methods

COM crystallization and growth experiments were conducted with samples and solutions prepared according to the methods described in Chapter 2. Calcium oxalate (CaOx) solution with 1 mM concentration was used for the initial nucleation of crystals and growth solutions with concentrations varying from 0.2 mM to 0.6 mM were used in AFM experiments to observe growth in real time at the nanometer scale.

Poly-ASP, e.g., poly(L-aspartic acid) sodium salt (Alamanda polymers), with lengths ranging from 10 to 200 amino acid residues was used as a crystallization modifier. Inhibitor solutions were prepared by diluting the reconstituted polymer solutions to the desired concentration, as described in Chapter 2.

Crystal growth was imaged in real time using a Multimode AFM with Nanoscope V controller (Bruker) equipped with a glass fluid cell scanning in contact mode at 25–40 lines/s. Imaging was performed with SNL-10 (Bruker) silicon nitride cantilevers (for specifications, see Table 2-1). Imaging forces were minimized by adjusting the set point voltage to the minimum required maintain tip-sample contact, allowing crystal surfaces to grow without disruption.

Supersaturated calcium oxalate solution with 0.3 mM concentration was introduced to the fluid cell from a plastic syringe using flexible polymer tubing (Tygon). The fluid cell was flushed with fresh solution every 5 min to prevent depletion of the concentration of calcium oxalate due to crystal growth during imaging. Previous studies have verified that growth rate remains constant to within 10% between injections of fresh solution [33]. The flushing also gave us the ability to rapidly change from growth solution to inhibited solution without interrupting the imaging. Growth solutions with concentrations ranging from 0.2 to 0.6 mM were used in our experiments. In order to prepare inhibitor solutions, a portion of the distilled water used in the recipe for the growth solution was replaced with the reconstituted poly-ASP solution. This resulted in supersaturated CaOx solutions with poly-ASP concentrations of 0.025 to 0.24 $\mu\text{g/ml}$.

Crystals fixed to the silicon substrate were located using a low-resolution optical microscope attached to the AFM system. COM crystals typically presented either {100} or {010} horizontal faces. Figure 3.1a shows a typical example of a COM crystal that can be seen in our samples with {010} face presented upwards, imaged by scanning electron microscopy (LEO Zeiss 1530) at the Western nanofabrication facility. Once an appropriate facet is identified, we continue incubation in the AFM with calcium oxalate solution for a few minutes to allow growth to continue and the system to reach a steady state before introducing fresh growth solution containing poly-ASP. For each length of polymer, we gradually increased the concentration beginning from a low value. At every concentration of polymer, changes in the surface morphology were observed. This allowed us to identify the threshold concentration for the appearance of strong directional pinning and it was fairly well defined. At the conclusion of

each experiment, the fluid cell was flushed with pure solution (i.e., without poly-ASP) to allow recovery of growth from inhibition to be observed. Each experiment was repeated with a new crystal on a new sample.

3.3 Results

The orientation of the $\{010\}$ faces required for the present experiments could be identified by scanning the entire crystal as in Figure 3.1b. Alternatively, in cases where the crystal was larger than the $\sim 14 \mu\text{m}$ range of the AFM scanner used, a smaller scan size was used to confirm the existence of growth hillocks with straight steps oriented along $[121]$ and $[120]$ directions, characteristic of the (010) face, as shown in Figure 3.1c. Step velocities were calculated to be approximately 2 nm/s .

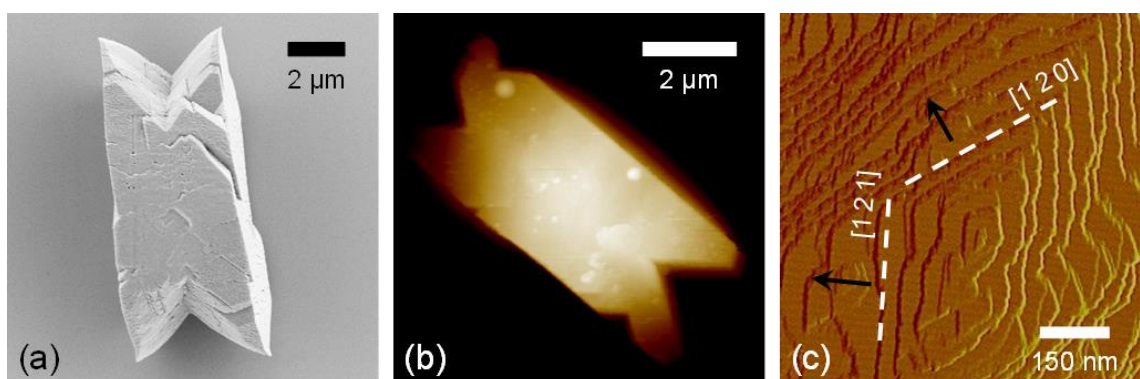


Figure 3.1. Images of the $\{010\}$ faces of COM crystals. (a) SEM image of a COM crystal with the $\{010\}$ face horizontal. (b) AFM height image of a $\{010\}$ face. (c) Higher resolution AFM deflection image of a $\{010\}$ face showing a growth hillock, defined by growth steps aligned with $[121]$ and $[120]$ step directions. Black arrows indicate the direction of propagation for steps.

Upon addition of poly(ASP), the initially straight steps on $\{010\}$ faces rapidly became rough (compare Figure 3.2a to Figure 3.2b). With inhibitor at all concentrations tested, the propagation speed decreases, in agreement with previous studies [1,38], for all lengths of poly-ASP. Upon increasing the poly-ASP concentration, growth in a particular direction, roughly $[120]$, ceased completely at a well-defined concentration, while steps continued in other directions. This directional pinning created finger-like features on the surface as seen in Figure 3.2c. This phenomenon was observed for all poly-ASP chain lengths, with a threshold concentration that

decreased with increasing polymer length, as shown in Figure 3.3. At still higher concentrations, growth is arrested in all directions.

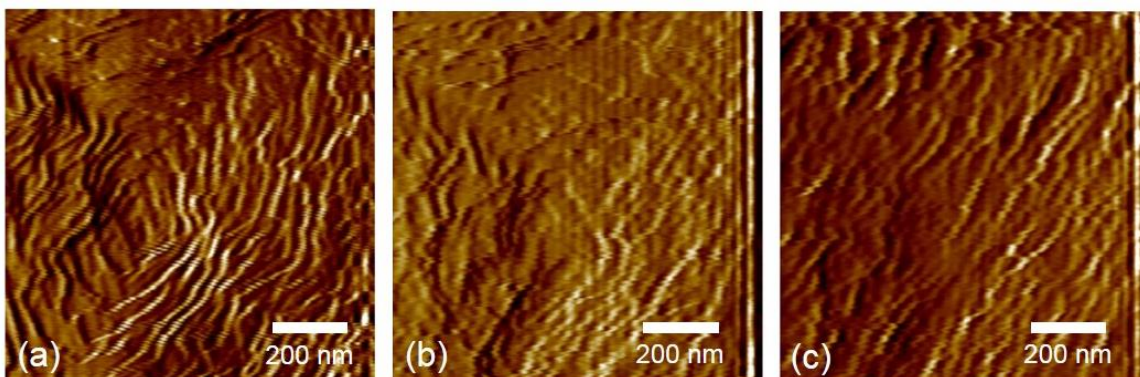


Figure 3.2. AFM images of growth steps on the same region of a COM {010} face (a) before and (b) and (c), after the introduction of 0.06 $\mu\text{g/ml}$ poly-ASP (50 residue).

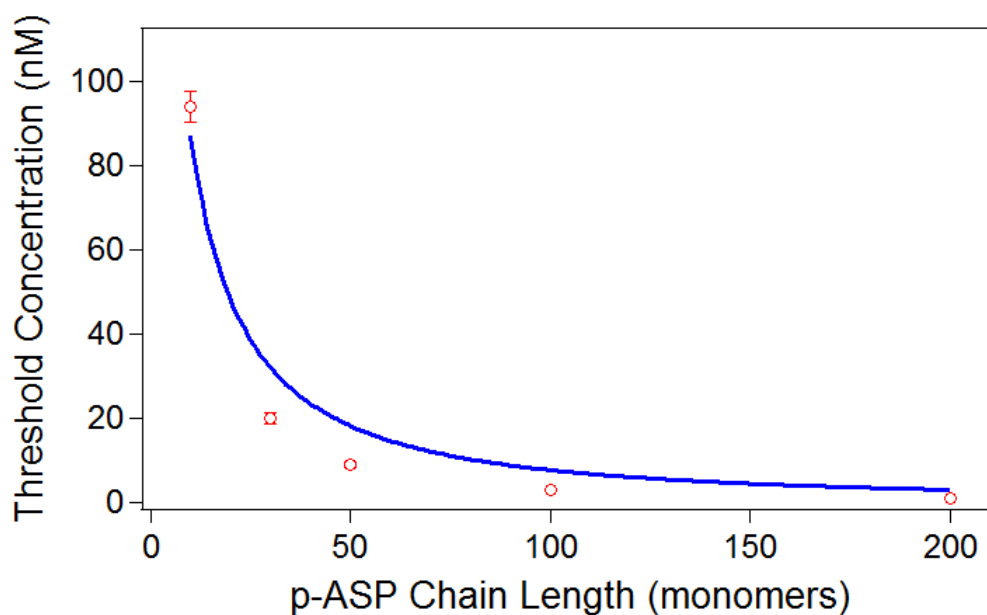


Figure 3.3. Threshold concentration required for directional pinning for growth in a 0.3 mM calcium oxalate solution. The solid curve represents a fit to the model discussed in section 3.4.

We performed a similar study but with a fixed inhibitor length (a 30 residue poly-ASP chain) and a variable calcium oxalate concentration ranging from 0.2 to 0.5 mM. The resulting threshold poly-ASP concentration for pinning increased with increasing calcium oxalate supersaturation as shown in Figure 3.4. Error bars of the inhibitor concentrations in Figure 3.3 and Figure 3.4 were recorded as the smallest increment in concentration that was used to determine the threshold.

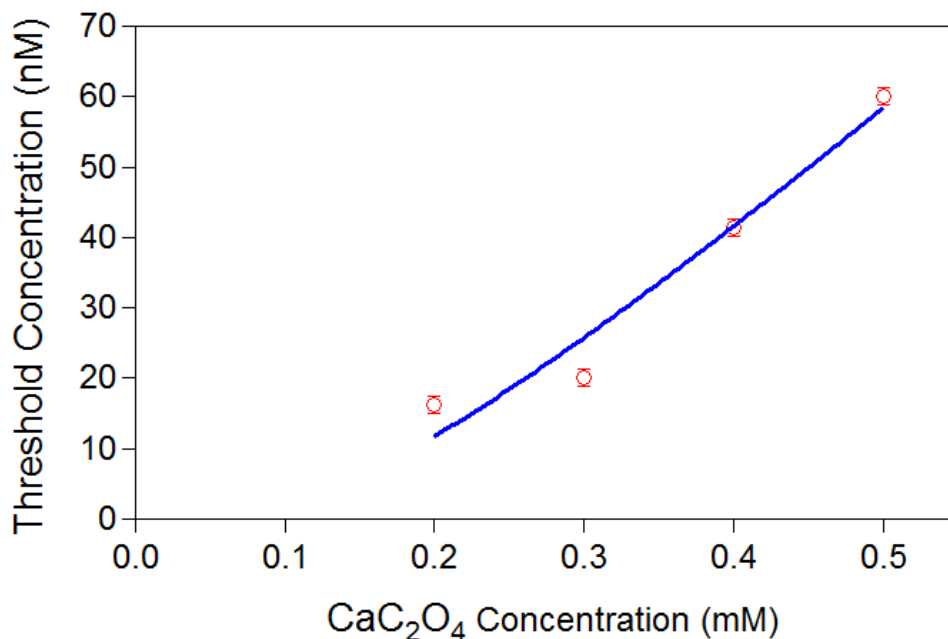


Figure 3.4. Threshold pinning concentration as a function of calcium oxalate concentration for a poly-ASP chain length of 30 amino acid residues. Solid curve represents a fit to the pinning model discussed in section 3.4

The width of the fingers as indicated by the arrow in Figure 3.2c (i.e., the distance between strongly-pinned steps) were measured using the AFM height images converted to 8-bit grey scale images (Figure 3.5a). Features in the image were isolated by processing it to a skeletonize form as seen in Figure 3.5b using ImageJ software (NIH, USA), where the edges of the features are reduced to a single pixel wide. Figure 3.5c shows a magnified image of one such feature. Widths of several features from one experiment was measured and the average value was calculated with the uncertainty estimated as the minimum length that can be measured. Resulting values were relatively independent of polymer length. However, the width decreased with increasing supersaturation, as seen in Figure 3.6. Width measurements were verified by roughly measuring the features in Nanoscope analysis software (Bruker).

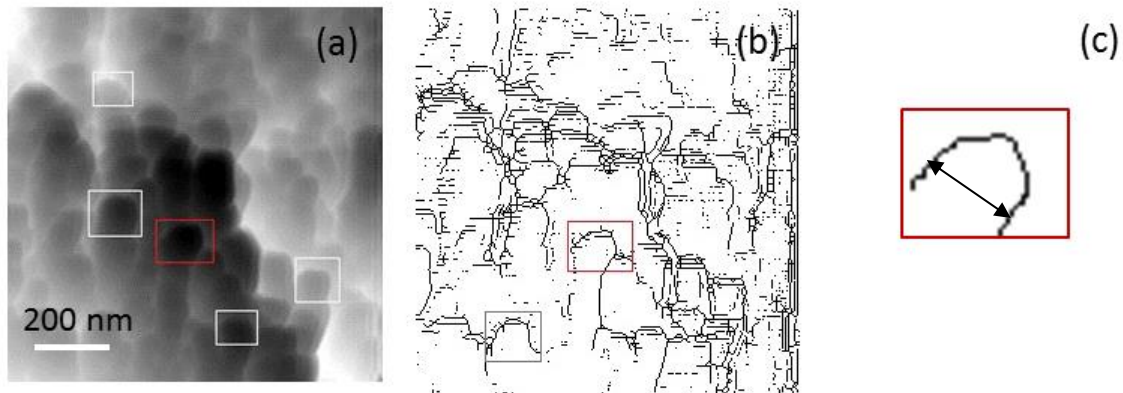


Figure 3.5 Processed AFM images leading to isolated features. Red box tracks the same feature. (a) 8-bit grey scale image of an AFM height image. Boxes indicate edges of few features. (b) Processed image with edges skeletonized. (c) A magnified image of an isolated feature. Arrow indicates the measured width.

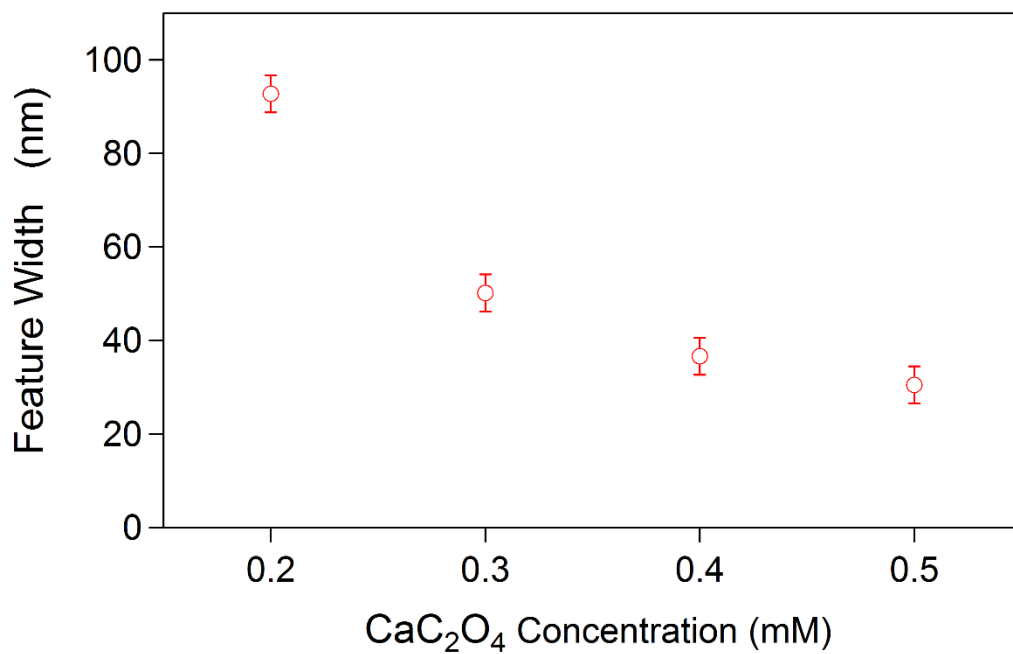


Figure 3.6. Average lateral distance between strongly-pinned steps as a function of calcium oxalate concentration.

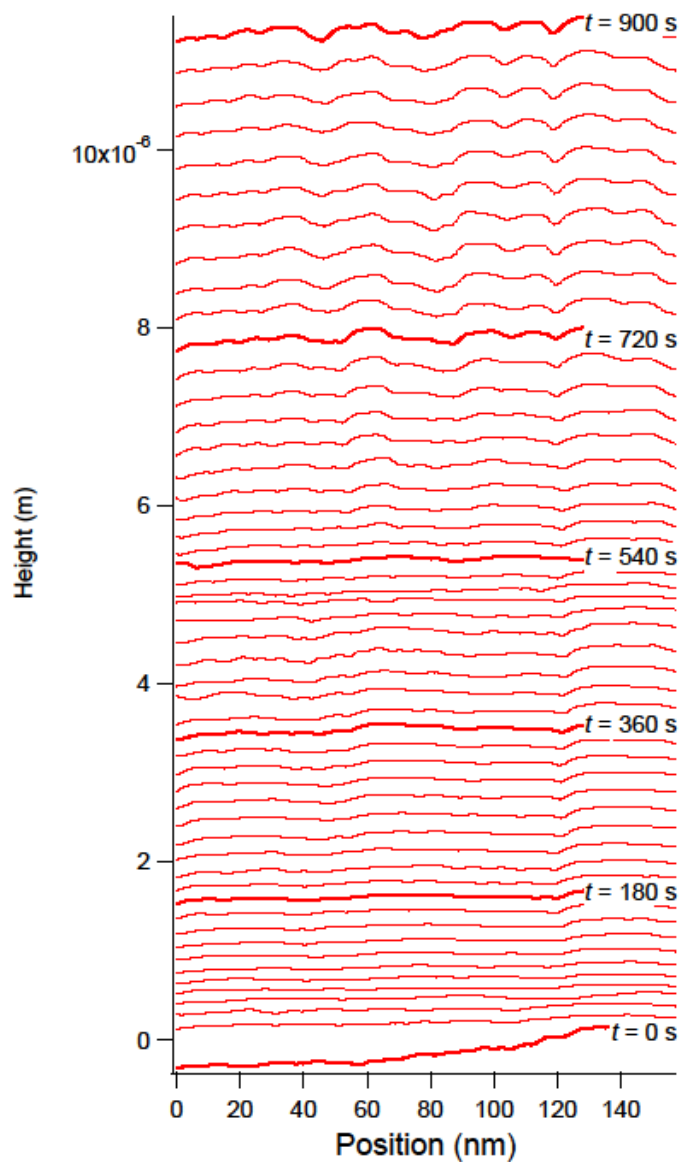


Figure 3.7 Evolution of cross-sections measured perpendicularly to the strongly pinned steps on a COM {010} face during inhibition from 0.125 $\mu\text{g/ml}$ of poly-ASP (10 residues). Each profile is offset vertically by 10 nm for convenience. After several minutes, a steady state is seen, with an average vertical growth rate of 0.05 nm/s.

The transition to the unidirectional pinned state can be observed in time-lapse movies (see supplementary movie 0.3mM_0.06pASP50). Due to the motion of steps in directions other than

the pinned direction, the $\{010\}$ face continues to grow vertically. Height cross-sections across the fingers reveal that narrow trenches form along the pinning direction, with a depth that attains a steady state within a few minutes. Figure 3.7 shows this transition from mobile steps a few unit cells high to well-defined features with typical heights of ~ 5 to 10 nm corresponding to heights of 5 to 10 unit cells in the $[010]$ direction.

At the end of experiments, larger scale images were acquired to ensure that there are no effects due to the act of AFM scanning. Figure 3.8 shows AFM height images of $\{010\}$ faces of COM crystal captured in the presence of poly-ASP. It is evident that AFM scanning is not influencing the growth.

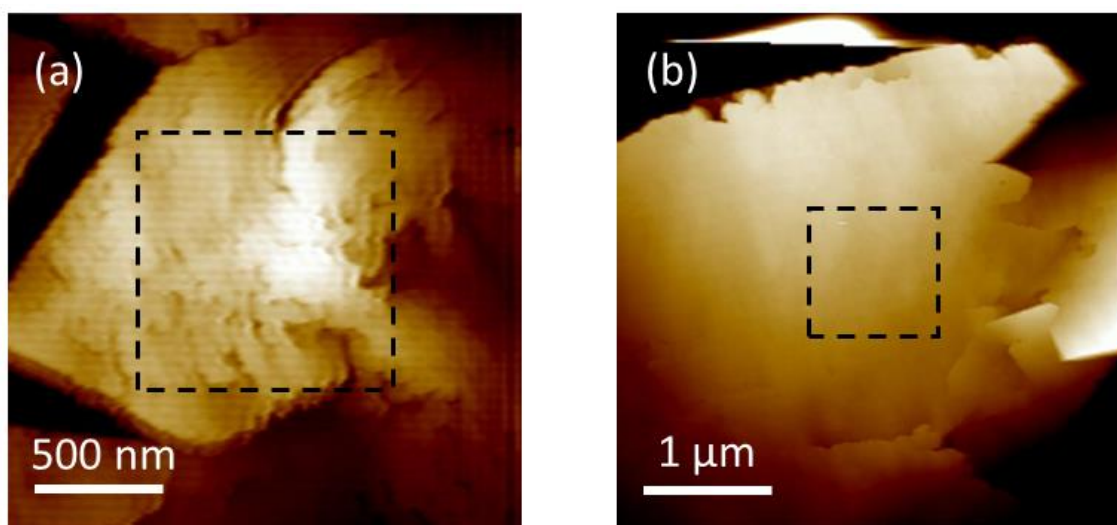


Figure 3.8. AFM height images of $\{010\}$ face of COM crystals imaged in the presence of poly-ASP. Dashed boxes indicate the $1 \mu\text{m}$ scan area. (a) Inhibited with $0.125 \mu\text{g/ml}$ of poly-ASP 10 in 0.3 mM CaOx . (b) Inhibited with $0.04 \mu\text{g/ml}$ of poly-ASP 100 in 0.3 mM CaOx

3.4 Discussion

Crystal growth on COM $\{010\}$ faces typically follows the classical picture of well-defined smooth steps flowing from a growth hillock centered on a screw dislocation. Previous studies of COM growth in the presence of poly(ASP) have revealed strong inhibitory effects on $\{100\}$ and $\{010\}$ faces [1,22,32,38], with step roughening consistent with the Cabrera-Vermilyea model.

Our observations agree with these basic results, but also demonstrate that pinning occurs more strongly in one particular direction. Formation of the resulting finger-like features was previously observed by Wang et al. [1], but not further discussed. Similar finger-like step bunches on crystals of potassium dihydrogen phosphate (KH_2PO_4) in the presence of Fe^{3+} were observed by Land et al. [59].

The observation that some directions are pinned more strongly than others indicates that poly-ASP directly affects steps, and does not bind to terraces, pinning any steps that passes, as would be expected in the Cabrera-Vermilee model. We attempted to model the threshold concentration for unidirectional pinning as a competition between adsorption of poly-ASP to already-pinned steps once a steady state has been achieved, and the removal of poly-ASP, due to either coverage by steps advancing along other directions or by desorption from the pinned surface. When poly-ASP is introduced to the growth solution, it must diffuse to the surface where it will be loosely bound until it encounters the preferred step direction as illustrated by Figure 3.9. The absence of fingers at concentrations lower than the threshold suggests that at low concentrations, bound inhibitors either desorb from the surface or become incorporated by the growing crystal before a strongly pinned step can form. At the threshold poly-ASP concentration, there is a sufficient supply of inhibitors from the solution that pinning persists.

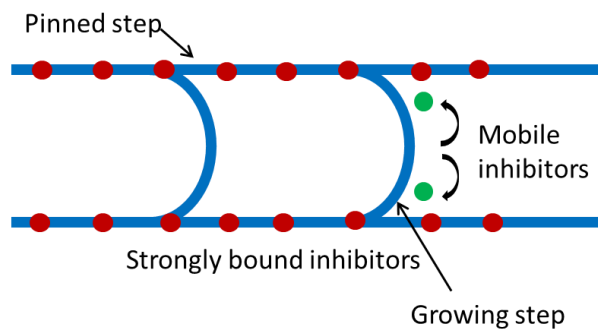


Figure 3.9 Schematic of the behavior of poly-ASP on COM crystal surface.

We model the rate of change of density of strongly-bound inhibitors, ρ_{1D} to a pinned step as

$$\frac{d\rho_{1D}}{dt} = r_+ C_i - r_- \rho_{1D}, \quad 3.1$$

where the rate constant r_+ controlling addition of poly(ASP) to the pinned step depends in principle on its diffusivity and probability of binding to a step, c_p is the inhibitor concentration in solution, and r_- characterizes the rate at which inhibitors are removed from participation in pinning, which is expected to be proportional to ρ_{1D} , the linear density of inhibitors along the pinning direction.

The density of strongly-bound inhibitors along the pinned step can change with time due to adsorption from solution, desorption from the step, and coverage by the advancing steps. A polymer in the solution has to diffuse through the solution and find its way to the crystal surface. We expect the rate of addition to the pinned step r_+ to be proportional to its diffusivity in solution and the number of possible binding sites. As a simple model, we consider its diffusivity to be that of a sphere of radius equal to the random-walk radius of gyration R_g of a polymer consisting of N monomers of length b . In that case,

$$D = \frac{k_B T}{\sqrt{6\pi\eta b}} \frac{1}{\sqrt{N}}. \quad 3.2$$

Polymers that diffuse from solution onto the surface between these pinned steps will be mobile, as they are loosely bound to the crystal, and diffuse until they meet a pinned step to form stronger bonds. Poly-ASP chains bind to the COM crystal surface by electrostatic interactions between Ca^{2+} ions on the surface and carboxyl groups on the polymer. We assume the rate of binding to be proportional to the number of monomers N , so that

$$r_+ \propto DN. \quad 3.3$$

In principle, bound poly(ASP) can be removed by both desorption from the pinned step, which is expected to be proportional to the amount of inhibitor already present (ρ_{1D}), or by incorporation into the growing crystal which is expected to be proportional to both the amount present and the normal growth rate R of the surface.

Clearly, desorption will be dominant in the limit of very low growth velocities, but previous studies done by Grohe et al. using fluorescently labeled OPN peptides show that incorporation of peptides into COM crystals can occur [31,39].

In order to estimate the incorporation rate, we note that for a step velocity v_s and steps of height h spaced a distance λ apart, R will be

$$R = \frac{v_s h}{\lambda}. \quad 3.4$$

If the effective height of the polymer on the surface is a , the rate of coverage should be proportional to

$$\frac{R}{a} = \frac{v_s h}{\lambda a}. \quad 3.5$$

Therefore, we express r_- as

$$r_- = \frac{v_s h}{\lambda a} + d, \quad 3.6$$

where d is the desorption rate.

The threshold concentration inhibitor density along the pinned step can be estimated using a simple geometry. If at the threshold there are enough inhibitors to keep the step pinned, then the distance between bound polymers must not exceed twice the critical radius of steps on the surface. Assuming that the polymer is aligned along the step as illustrated in Figure 3.10, we find

$$\rho_{1D} \approx \frac{1}{l+2r^*} \quad 3.7$$

at the threshold where l is the length of the polymer and r^* is the one-dimensional critical radius.

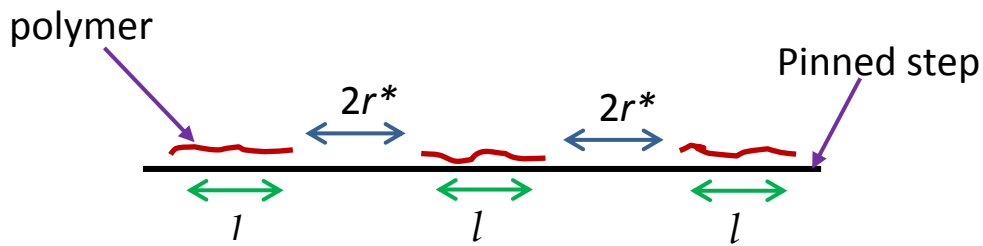


Figure 3.10 Configuration of poly-ASP molecules on a step at threshold pinning.

In equation 3.7, the value of l depends on the configuration of the polymer on the surface. If it attaches to the surface as a “blob”, then l will be radius of gyration. Previous studies of adsorption of polymers on surfaces suggest that polymers lay flat [61]. We therefore assume the polymer to be fully extended along the step so that l is its end-to-end length, bN . At threshold pinning, the inhibitor density ρ_{1D} is then

$$\rho_{1D} \approx \frac{1}{bN+2r^*}, \quad 3.8$$

where b is the monomer length and N is the number of monomers in each chain.

At a steady state, there is no variation in the inhibitor density with time. Then equation 3.1 becomes

$$\frac{d\rho_{1D}}{dt} = r_+ C_i - r_- \rho_{1D} = 0, \quad 3.9$$

so that

$$r_+ C_i = r_- \rho_{1D}. \quad 3.10$$

The inhibitor concentration at threshold is then

$$C_i = \frac{r_- \rho_{1D}}{r_+} = \frac{\sqrt{6\pi\eta b}}{4\pi k_B T \sqrt{N}} \left(\frac{v_s h}{\lambda a} + d \right) \frac{1}{bN + 2r^*}. \quad 3.11$$

Some of the parameters in the model are known or can be measured from AFM images. For example, the spacing between steps can be measured in the AFM images and was found to be between 30 and 50 nm. The velocity of steps between the pinned sites was measured as ~ 2 nm/s by tracking a single step's displacement in a series of AFM images. The critical radius can be measured from the minimum curvature at the very center of a growth hillock to be in a rough range of 5 – 10 nm. The monomer length (b) and height of the molecule (a) were estimated using bond lengths. Other parameters such as step height and viscosity of the fluid were collected from the literature.

A non-linear least square fit to the measured threshold concentrations as a function of poly-ASP chain length is shown in Figure 3.3. The fit force the desorption term d to zero, indicating that the desorption is not the dominant form of inhibitor removal. The monomer length and molecule height, which was set as free parameters, returned values 0.4 and 0.7 nm. These values are of the right order of magnitude but are higher than the calculated values. All fit parameters can be found in Table 3-1.

Table 3-1 Fit parameters for equation 3.11 in Figure 3.3 and Figure 3.4.

Fit parameter	Variable: poly-ASP length (N)	Variable: C_{CaOx}
	$C_{CaOx} = 0.3$ mM	Poly-ASP length = 30
Step velocity (v_s)	2 nm/s	2 nm/s
Step height (h)	1 nm	1 nm
Viscosity (η)	0.00093 Pa s	0.00093 Pa s
Boltzmann constant (k_B)	1.38×10^{-23} J/K	1.38×10^{-23} J/K
Temperature (T)	300 K	300 K
Distance between steps (λ)	50 nm	50 nm
Critical radius (r^*)	5 nm	5 nm
Desorption rate (d)	0	0
Monomer length (b)	0.4 nm	0.4 nm
Inhibitor molecule height (a)	0.678 ± 0.001 nm	0.67 nm
Saturation concentration (C_{sat})		0.052 ± 0.005 mM

In order to validate the model, we attempted to fit equation 3.11 to the data in Figure 3.4, in which the supersaturation is varied and poly-ASP length is kept constant at 30 monomers. As both step velocity and critical radius depend on supersaturation, they were replaced by

$$v_s = v_{fit} \frac{C_{CaOx} - C_{sat}}{0.3 - C_{sat}} \quad 3.12$$

and

$$r^* = \frac{r_{fit}^*(0.3 - C_{sat})}{(C_{CaOx} - C_{sat})}. \quad 3.13$$

In this case C_{sat} is the saturated constant and C_{CaOx} is the CaOx concentration while v_{fit} and r_{fit}^* are fit parameters returned by the fit equation 3.11 for $C_{CaOx} = 0.3$ mM. All parameters were set fixed at values from the fit in Figure 3.3 while C_{sat} was set as a free parameter. The fit returns a saturation concentration of 0.052 mM, which roughly agrees with the saturation concentration of 0.07 mM calculated using ionic strength (Table A.7 in Appendix A).

In the case of width of the features decreasing with increasing supersaturation (Figure 3.6), one would intuitively expect that as step velocities increase, inhibitors are able to only diffuse over a short distance in the time it takes to encounter a step.

This simple model for threshold concentration unidirectional pinning seems to describe approximately the behavior of inhibitors causing the directional pinning, at steady state with physically realistic parameters.

3.5 Conclusion

Introducing low concentrations of poly-ASP has resulted in steps that are pinned in one particular direction (roughly [120]), on {010} faces of COM crystals. These unidirectional features start to form at a threshold inhibitor concentration that varies with the length of the polymer. As an attempt to describe the inhibitor mechanism at the threshold concentration we have modelled the threshold inhibitor concentration as a result of the competition between adsorption from solution to already pinned steps and removal of inhibitors from the pinned step by desorption and incorporation into the crystal due to coverage by advancing steps in other directions. At the steady state, adsorption to the step is governed by diffusion of the polymer in solution and available binding sites on the polymer. At the same time, depletion of inhibitor from the pinned step depends on the linear inhibitor density on the strongly pinned step and the rate of vertical growth of the crystal. In order to keep the steps completely pinned, the distance between polymers must be less than the twice the critical radius. Polymer density can then be calculated using simple geometry.

Combining these factors for steady-state pinning leads to equation (3.11), which represents the polymer concentration in solution at threshold. Equation 3.11 predicts a dependence of threshold inhibitor concentration on poly-ASP chain length with a shape similar to the experimental data shown in Figure 3.3. Fitting these data yields parameters consistent with our expectations. The model was then further validated by fitting equation 3.11 to experimental data in Figure 3.4, using the same parameter values. Future experiments and quantitative analysis with molecular dynamic simulations may allow us to validate the model further.

4 Calcium Oxalate Dihydrate Inhibition with Osteopontin Peptide Series

4.1 Introduction/ Motivation

The study of calcium oxalate crystallization has become an interesting area of research in the health care industry since calcium oxalate is the principal component of kidney stones. Kidney stone disease, a very painful condition that can lead to renal failure, afflicts more than 10% of the human population [42]. Calcium oxalate in kidney stones is typically found in two different crystalline forms, each distinguished by different ratios of water: calcium oxalate monohydrate (COM) and calcium oxalate dihydrate (COD) [2]. COM is the most abundant and thermodynamically stable form of calcium oxalate in kidney stones and is seldom excreted by a healthy person. In contrast, COD crystals are flushed out routinely with urine by both stone formers and healthy humans [18,19]. Studies have shown that once nucleated, the crystals will normally pass into urine before they attain a large size and form stones [62]. However, if they are not excreted, COD crystals can transform into more stable COM crystals or aggregate with other crystals to develop kidney stones. COD forms bipyramidal crystals with a unit cell of a tetragonal structure (Figure 4.1a) with lattice dimensions of $a = b = 12.371 \text{ \AA}$, and $c = 7.357 \text{ \AA}$ [41,42].

As COD crystals are less damaging to the kidney cell membrane than are COM crystals [44], the existence of COD crystals in the system is of special interest to the health care industry. OPN and peptides derived from OPN have been proven to inhibit COM and promote the less stable COD [17,48]. It has been observed that the presence of certain peptides or polymers induces morphological changes in COD crystals. Zhang et al. used a double hydrophilic block copolymer (poly(ethylene glycol)-*block*-poly(methacrylic acid)), which consists of one hydrophilic block that interact strongly with mineral surfaces and another hydrophilic block that promotes solubilization in water, to explore formation and transitions of COD. They found that the presence of the block-copolymer favours the morphological transition of COD crystals from tetragonal bipyramids (Figure 4.2a) to elongated tetragonal prisms dominated by $\{100\}$ faces (Figure 4.2b) [54].

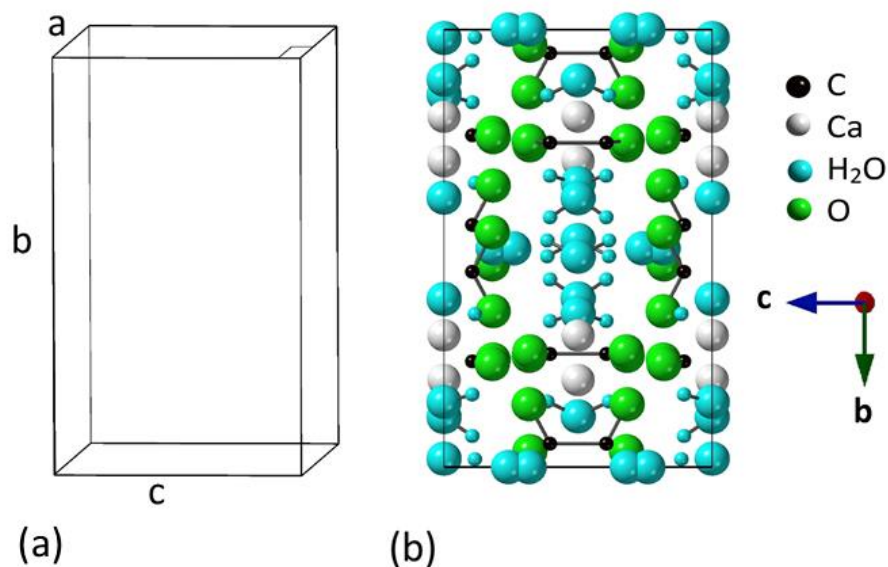


Figure 4.1. (a) Schematic of the unit cell of the COD crystal. (b) (100) face of the unit cell with atom positions indicated.

Jung et al. investigated the modifications to COD by three different anionic polymers: poly-aspartate, poly-glutamate and poly acrylate. They explained the change in the crystal shape as the preferential interaction of the polymers with {100} faces due to the higher Ca^{2+} density ($0.04395 \text{ ions}/\text{\AA}^2$) than on {101} faces ($0.0125 \text{ ions}/\text{\AA}^2$) [41,47]. All inhibitors studied on COD, including block copolymers, inhibited the growth of {100} faces to a higher degree than the {101} faces, making the triangular {101} faces grow faster than {100} faces, resulting a large rectangular {100} face elongated along the c-axis.

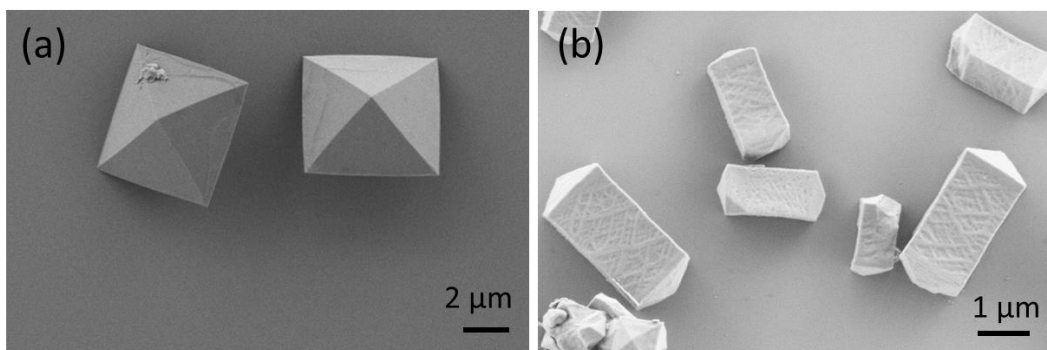


Figure 4.2. SEM images of different types of COD crystals. (a) Tetragonal bipyramid COD crystals. (b) Elongated tetragonal prism COD crystals.

Another critical factor in the formation of kidney stones is the attachment of nucleated crystals to the tubular cell surface. The adhesive molecules distributed on the apical surface of the tubular cells determines whether the crystal binds and is retained as a kidney stone [45]. A study done by Lieske et al. has characterized the adhesion interaction energy between COD and top free surfaces of renal epithelial cells of monkeys, in culture. The results showed that COD crystals adhere to the cells rapidly, preferentially on the $\{100\}$ face. This preferential binding is explained as a result of oxalate ions on the surface of $\{100\}$ faces that are orthogonal to the face itself (Figure 4.2a), providing the ideal binding site for the epithelial cells to interact with the crystals. $\{101\}$ faces present oxalate ions that emerge at the surface at an acute angle relative to their face (Figure 4.2(b), therefore having less affinity to cells [45,51].

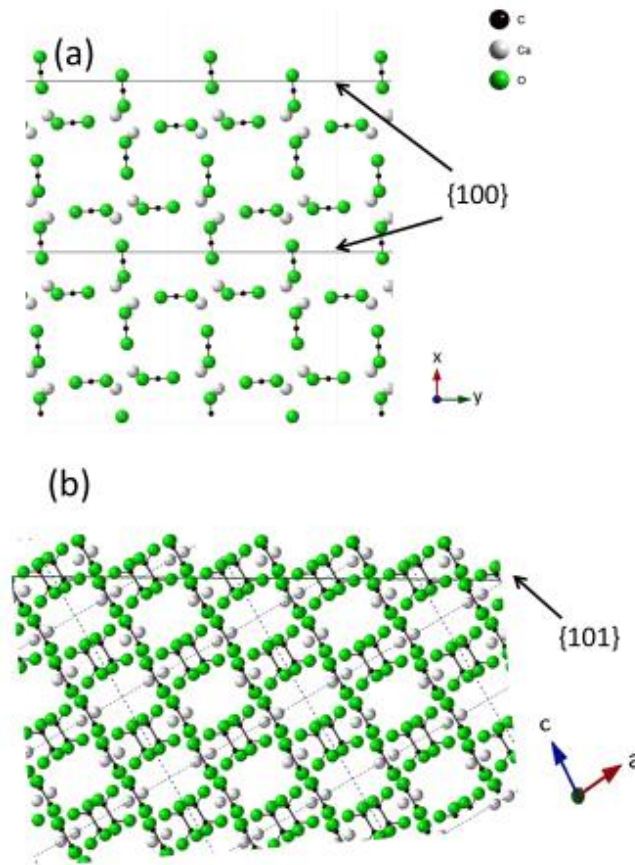


Figure 4.3 Cross sections showing oxalate ion and Ca^{2+} ion positions on (a) $\{100\}$ faces looking down the z-axis and (b) $\{101\}$ faces looking down the y-axis. Water molecules are omitted for better visualization of the ions.

4.2 Materials and Methods

Crystal samples used for our experiments were synthesized using 1 mM calcium oxalate solution and 0.5 mg/ml poly-Acrylic Acid (poly-AA) (Sigma-Aldrich) solution. Solutions used for the AFM experiments were prepared using the methods described in Chapter 2. Poly-AA is an extremely potent inhibitor of COM; even concentrations as small as 1 $\mu\text{g/ml}$ have been demonstrated to affect its growth [46]. While poly-AA is nearly preventing COM, it also affects COD formation so we can control the shape of the crystals formed. The concentration of poly-AA present determined the prominent face of the resulting crystals, as it affects the growth speed of each face differently. 4 $\mu\text{g/ml}$ and 24 $\mu\text{g/ml}$ poly-AA resulted in crystals with {101} faces prominent or {100} faces prominent, respectively. All samples were nucleated in tissue culture wells (9 well plate, BD Canada), with a glass cover slip at the bottom (20 mm, Ted Pella, Inc.), with 850 μl of calcium and oxalate stock solutions, 40 μl or 240 μl of 0.5mg/ml poly AA, solution and finally deionized water to bring the final volume in the cell to 5 ml. The well plate was then left undisturbed for 72 hours to permit nucleation. After 72 hours, the walls of the wells and the glass cover slips were lightly scraped to dislodge the crystals. These crystals were then transferred to pieces of silicon wafers and glued down using an UV curing adhesive (Norland Optical Adhesive NOA 81, Norland Products, Inc.) that cures upon exposure to ultraviolet light to prevent them from dislodging while scanning. More details are provided in Chapter 2.

Poly (aspartic acid) with lengths of 10 and 50 amino acid residues as well as several peptides derived from OPN were used to study modifications of crystallization. These OPN peptides, termed pOPAR, HHS, DVL, and P3, are known to have different iso-electric points, [1] which is the pH at which the peptide is electrically neutral and does not migrate in an electric field.

Crystal growth was imaged in real time using a Multimode AFM with Nanoscope V controller (Bruker) equipped with a glass fluid cell scanning in contact mode at 30 – 40 lines per second. Imaging was performed with SNL-10 (Bruker) silicon nitride cantilevers. Imaging forces were minimized by to avoid any damage to the crystal surface that could affect growth.

Supersaturated 0.4 mM calcium oxalate solution was introduced into the fluid cell from a plastic syringe using flexible polymer tubing (Tygon). During imaging, the concentration of calcium oxalate in the fluid cell decreases as the crystals grow. To prevent this from affecting growth, the fluid cell was flushed with fresh solution every 5 min. Previous studies have verified that the growth rate remained constant to within 10% between injections of fresh solution [33]. The procedure of flushing rather than continuous flow gave us the ability to rapidly change from growth solution to inhibited solution without interrupting the imaging.

At the beginning of each experiment, a large area of the sample is imaged in order to identify the orientation of the crystals. When scanning a triangular {101} face, a relatively horizontal surface was selected to avoid possible scanning artifacts. For example, if the crystal surface is at a steep angle the scanned image will be a projection of the true topology and the limited vertical range of the piezoelectric scanner might prevent the entire face from being imaged. Also, the edge of the crystal could interact with the cantilever rather than AFM tip, which would lead to spurious images and might even damage the cantilever or dislodge the crystal.

Once an appropriate facet is identified, we allowed the system to sit in growth solution for a few minutes to ensure that a steady state had been reached. Growth of the facet in pure growth solution was imaged at the beginning of the experiment to confirm growth and to locate an area with a hillock or clean straight steps. Images were captured in pure growth solution for 5–10 mins before introducing fresh solution containing inhibitors. All peptides and polymers were introduced in 2 $\mu\text{g/ml}$ and 5 $\mu\text{g/ml}$ concentrations. Then, the crystal was imaged for 20–25 mins in inhibited solution to observe the changes in growth kinetics. Finally, the inhibited solution was flushed with fresh pure solution (without inhibitor) at a calcium oxalate concentration of 0.4 mM. This procedure was repeated a 2 – 3 times, each time on a new sample, for each peptide and concentration. Collecting images for pure growth, inhibited growth and recovery from inhibition for every polymer and peptide of interest allowed us to compare the changes in growth induced by each inhibitor.

4.3 Results

The two faces of COD crystals studied exhibited different features. The triangular {101} faces shown in Figure 4.4a consist of pyramidal hillocks bound by straight steps (Figure 4.4b). The angle of the triangular hillocks matches the dihedral angle of the crystal of $\sim 81^\circ$. Even though studies performed by Jung et al. indicated that the velocity of steps on {101} faces is too fast to measure [35], our observation was of steps moving at a low velocity of 0.1 – 0.2 nm/s. Calcium oxalate concentrations were increased from 0.3 mM to 0.6 mM in an effort to observe faster growth but were unable to produce speeds beyond 0.4 nm/s. In another experiment, half of the NaCl solution was replaced with pure water to increase the activity coefficients and effective supersaturation. None of these efforts succeeded in a significant increase in step speed. Our observation of the absence of any alteration to the morphology of the {101} faces in the presence of the peptides studies suggests that step-inhibitor interactions are not significant on this face.

Table 4-1 Phosphorelated peptide sequences derived from OPN and their iso-electric points. The main amino acids in the sequences are Serine (S), Aspartate (D) and Glutamate (E) (see Appendix C for more details).

Peptide	Sequence	Iso-electric point (pH)	Molecular weight (g/mol)	Molar concentration at 2 $\mu\text{g/ml}$ (mM)	Molar concentration at 5 $\mu\text{g/ml}$ (mM)
pOPAR	pSHDHMDDDDDDDDGD	3.39	1929	1.0	2.6
P3	pSHEpSTEQSDAIDpSAEK	2.98	2019	0.9	2.5
HHS	HHpSDEpSDESFTASTQA	3.48	1938	1.0	2.6
DVL	DVLTPIAPTVDVPDGR	3.93	1665	1.2	3.0

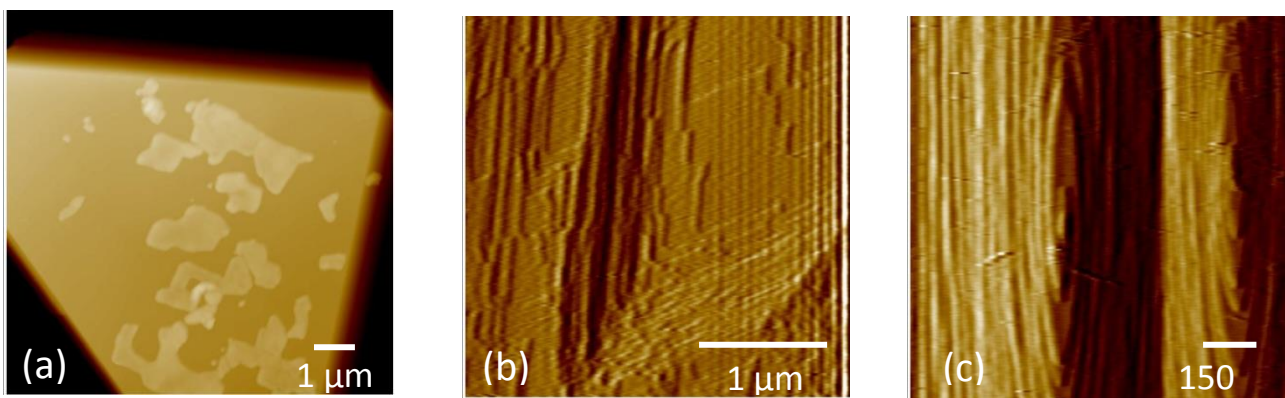


Figure 4.4 AFM deflection images of (a) a triangular $\{101\}$ COD face. “blobs” seen on the surface are presumed to be either glue or a poly-AA film. (b) triangular hillocks on a $\{101\}$ face, and (c) elongated elliptical hillocks on a $\{100\}$ face.

The rectangular $\{100\}$ faces showed very elongated elliptical growth hillocks with a well-defined center, growing rapidly (Figure 4.4c). Growth of hillocks was captured with a scan rate of 30–40 lines/s and 256 lines per frame. However, tracking a single step in consecutive images still proved to be difficult even at this high (for atomic force microscopy) frame rate. Initially, we studied growth and inhibition with poly-ASP chains of 50 monomers to compare our observations with those in literature [47]. Our results showed the same elliptical growth hillocks in growth from pure calcium oxalate solutions without inhibitor, which became more circular when inhibited with poly-ASP.

Experiments conducted using other members of the OPN peptide series showed similar results. Since the molecular weight of the peptides differ, the molar concentrations corresponding to mass concentrations of 2 $\mu\text{g/ml}$ and 5 $\mu\text{g/ml}$ range from 1.2 mM to 3.0 mM (see Table 4.1). Most peptides changed the morphology of the crystal face, elongated elliptical hillocks became less elongated or, in some cases, nearly circular. The resulting change depend on the peptide, despite similar molar concentrations. Figure 4.5 shows the inhibition state of the crystal 1 min after introducing 5 $\mu\text{g/ml}$ of each peptide to the face.

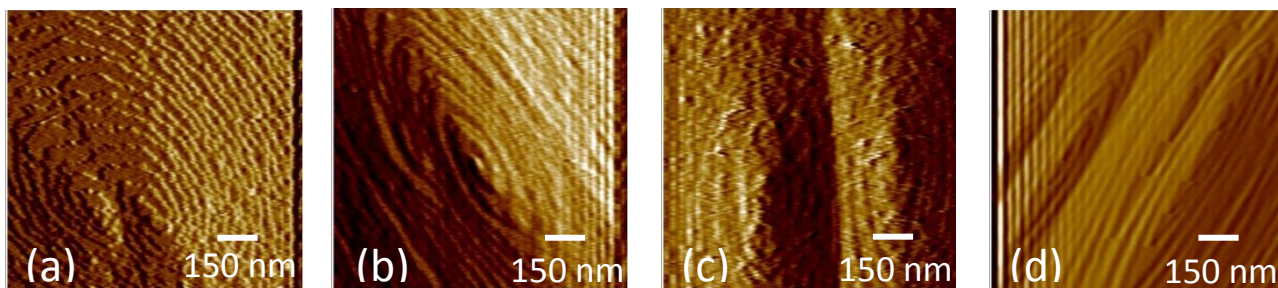


Figure 4.5 AFM images of COD (100) faces, 1 min after inhibition with (a) pOPAR, (b) P3, (c) HHS and (d) DVL.

Of the four OPN peptides studied, only the peptide with the highest iso-electric point (DVL) did not affect crystallization. The aspect ratios were determined by measuring the major and minor axes of the elliptical hillocks, using a spiral step as a reference, as shown in Figure 4.6. This process was repeated three times for each hillock with three different steps.

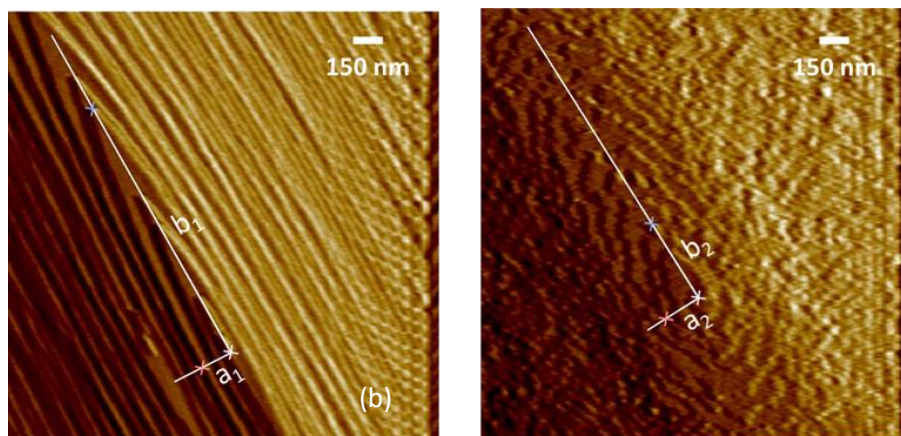


Figure 4.6 Measurement of aspect ratios of hillocks on the (100) face of a COD crystal for (a) growth without an inhibitor (b) growth in the presence of 5 $\mu\text{g/ml}$ pOPAR.

The aspect ratios between uninhibited hillocks and inhibited hillocks were compared and the change in the ratio for each peptide was calculated as a percentage of the uninhibited hillock ratio. The results are shown in Figure 4.7 for mass concentrations of 5 $\mu\text{g/ml}$.

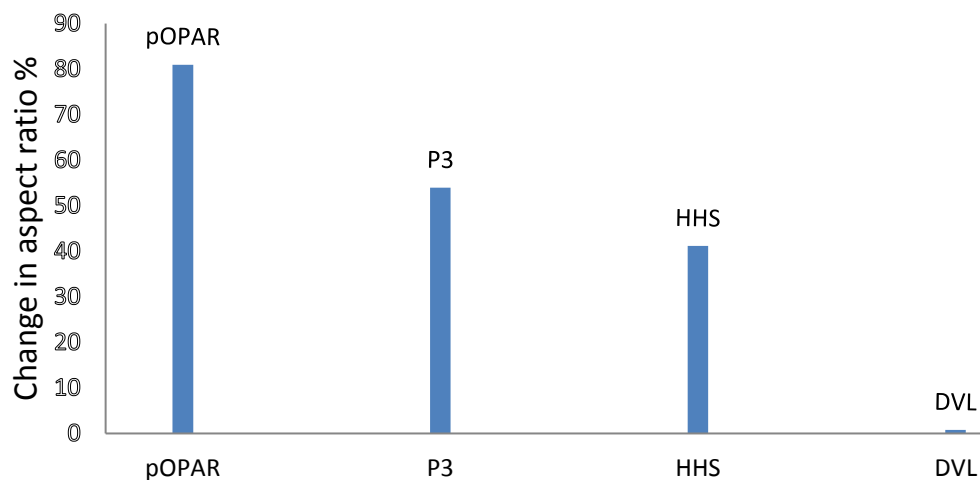


Figure 4.7 Change in aspect ratio of hillocks on the $\{100\}$ face of COD crystals, after introducing $5 \mu\text{g/ml}$ peptide solution, relative to pure growth.

4.4 Discussion

Inhibition of COD was investigated with several peptides derived from OPN. The $\{100\}$ faces presented hillocks that are elongated spirals oriented along the $[010]$ direction with two main growth directions, $[001]$ and $[010]$, as shown in Figure 4.8. In most cases, unless inhibited, the growth hillock had an apparent cusp indicating the complete lack of a step in the $[001]$ direction (Figure 4.8). This is not surprising given that this direction is responsible for the appearance of $\{100\}$ face, which never occurs without inhibition. During crystal growth, the fastest growing directions are bound by slower-growing faces and disappear. Absence of $[001]$ steps from the ellipse implies that it is the fastest growing step direction on that surface. Continued growth in the other directions, would ultimately result in the disappearance of the $\{100\}$ face. The fact that naturally occurring COD crystals lack $\{100\}$ faces confirms that those faces are the fastest growing ones, with the triangular $\{101\}$ faces, growing more slowly. $\{100\}$ faces can only be seen when an inhibitor is in the system, slowing step growth on those faces. If the velocity decreases by the same fraction in all directions, the resulting inhibited hillock must show a similar aspect ratio to the original hillocks. Observation of less elongated or circular hillocks during inhibition shows that $[001]$ steps are slowed by a relatively larger amount than are the $[010]$ steps. This is evidence that peptides are more strongly attracted to the $[001]$ step direction than to the $[010]$ direction.

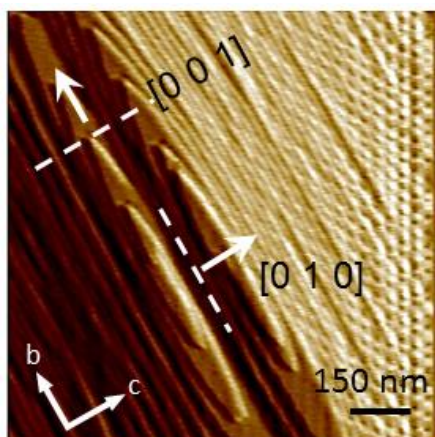


Figure 4.8 AFM deflection image of a growth hillock on a {100} face of a COD crystal. Arrows show the growth direction of each step. The b and c axes indicate the orientation of the COD unit cell shown in Figure 4.1.

Comparing the aspect ratios of the inhibited hillocks allows us to quantify the effectiveness of each inhibitor in retarding the growth. We find that peptides with lower iso-electric points have more effect on growth with the trend that those with the highest iso-electric points have little or no effect.

Table 4-2 Ca^{2+} ion density for each of the faces.

Possible step risers for [001] are (010) and (110).

Possible step risers for [010] steps are (001) and (101).

COD plane	Ca^{2+} density ($\text{Ca}^{2+} / \text{\AA}^2$)
(010) or (100)	0.0439
(110)	0.0152
(001)	0.0277
(101)	0.0125

Hillocks are comprised of step risers and terraces. The terrace has the same Miller indices as the face of the crystal and the step riser is a crystal plane at an angle to the terrace. Inhibition of the growth step could be due to a peptide adsorbing to a terrace, riser or both. There are several

potential indices of the step risers for the two main step directions on {100} faces, and we are unable to distinguish them experimentally. Possibilities that we deem likely for the [001] step are illustrated in Figure 4.9. Of course, these are idealizations – the actual step shape doubtless goes through many configurations as individual ions are incorporated.

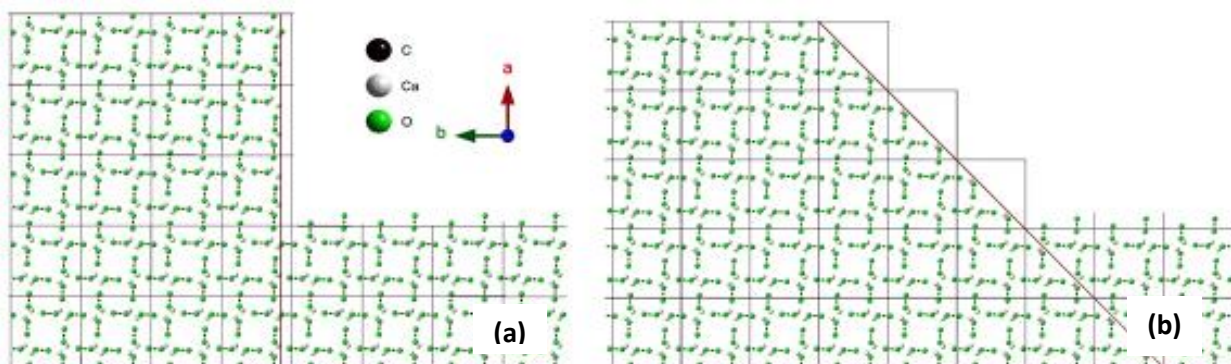


Figure 4.9 Two possible step risers for the [001] step on {100} faces: (a) (010) plane, (b) (110) plane. For convenience, the steps are shown to be several oxalate ions in height, but in reality, may be shorter.

Since the degree of inhibition depends on the direction, we postulate that the inhibitors bind to the steps. The different degrees are then likely due to differences in the structure of the step for the principal directions. According to the crystal structure, a [001] step could have (010) or (110) planes (see Figure 4.9) as step risers, both of which are low-index planes and therefore should have low surface energy. Calcium ion densities of each plane was measured using the Crystal maker software (Crystal maker software limited, Oxford, England) by slicing five-unit cell high crystal slab with each plane and counting the ions on the surface of that plane. Measured ion densities can be found in Table 4-2. A (010) riser has the same atomic arrangement as the {100} face with a high ion density of $0.0439 \text{ Ca}^{2+} / \text{\AA}^2$ (Figure 4.11), and are known to attract anionic macromolecules [41,47]. On the other hand, the (110) plane has a low Ca^{2+} density of $0.015 \text{ Ca}^{2+} / \text{\AA}^2$.

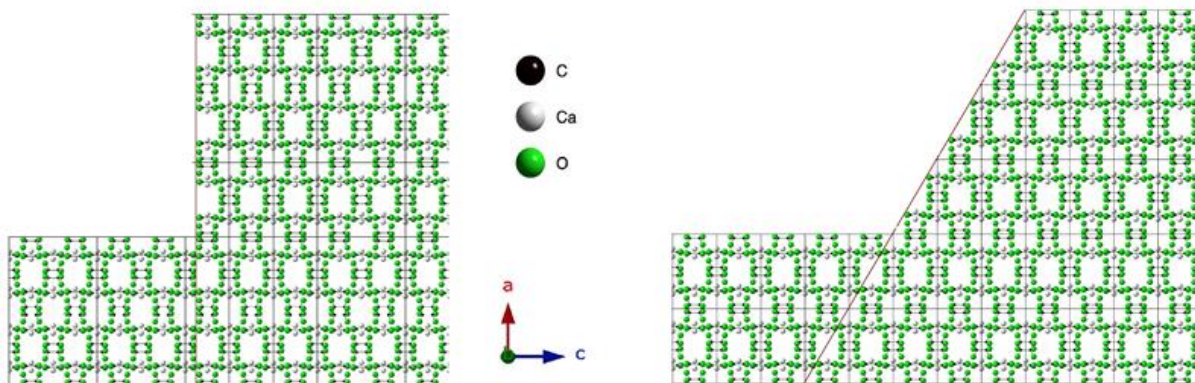


Figure 4.10 Two possible step risers for the [010] step on {100} faces: (a) (001) plane, (b) $(10\bar{1})$ plane. For convenience, water molecules are not shown, and steps are shown with a height of several unit cells.

Possible step risers for the [010] step are (001) and $(10\bar{1})$ planes with $0.0277 \text{ Ca}^{2+}/\text{\AA}^2$ and $0.0125 \text{ Ca}^{2+}/\text{\AA}^2$ Ca^{2+} densities respectively, which are illustrated in Figure 4.10.

Considering the calcium ion density, it is evident that out of all possible risers, (010) plane has the most calcium ions available to potentially bind with anionic peptides. Oxalate ions on both these planes are organized in layers with two different orientations. One layer has oxalate ions parallel to the {100} face and the other layer has oxalates normal to the face. These alternating orientations provide access to more Ca^{2+} ions than any other plane on COD crystals [51]. Out of the two step likely risers for the [001] step, we expect anionic molecules such as aspartic acid to make stronger bonds with the (010) plane.

Previous studies done by Thomas et al. and Chien et al. show weak adsorption to {101} planes [43,46], which they explain as due to the low ion density of these faces. This explains why the triangular faces are less inhibited [47,51] and is consistent with our observations. The higher affinity of anionic inhibitors with the {100} and {010} planes mean that inhibitors readily adsorb to the prismatic faces and the (010) step risers of the [001] steps on the prismatic faces. This explains why inhibitors promote the existence of these planes and why the growth hillocks become less elliptical in their presence.

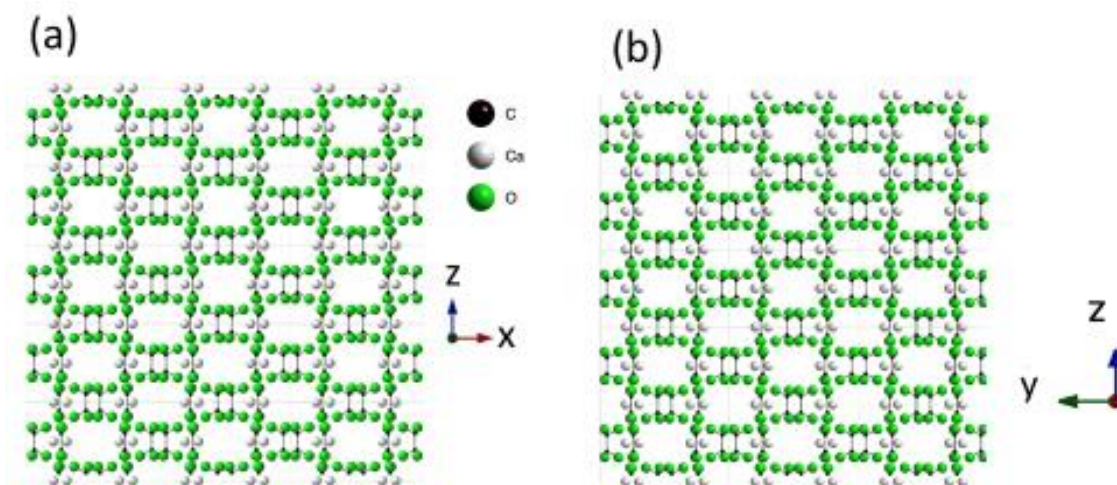


Figure 4.11 Atomic structures of COD {100} and {010} faces, illustrating similar atom positions.

4.5 Conclusion

Growth of COD crystals was imaged in real time using the AFM in the presence of peptides synthesized from OPN. Growth hillocks on {100} faces were elongated along the [010] direction with cusps on ends representing the lack of steps aligned with the [001] direction. Introducing peptides inhibited both step directions with the step velocity of [001] steps decreasing by a greater fraction. As a result, the presence of the inhibitors studied resulted in hillocks that were less elongated and, in some case, nearly circular. We studied the effects of a series of peptides with different iso-electric points ranging from 2.92 to 3.93 as listed in Table 4-1. It was observed that each peptide inhibited {100} faces of COD to a different degree. pOPAR, P3 and HHS changed the morphology and decreased step speeds, but DVL peptide had negligible effect on both the morphology and step speed. Measurements of the aspect ratio of the inhibited hillocks were used to quantify the activities of the inhibitors.

The differential affinity of the inhibitors to different steps is likely due to the atomic structures of steps. The [001] step direction which shows preferred binding with peptides likely exhibit either a (010) or (110) plane as the step riser. The (010) plane has the highest Ca^{2+} density ($0.0439 \text{ Ca}^{2+}/\text{\AA}^2$) of all COD planes and existence of this plane as a riser is most likely why [001] steps show a high affinity to inhibitors.

The [010] step direction could have $(10\bar{1})$ or (001) plane as the step risers and the $(10\bar{1})$ plane is the triangular face observed in naturally occurring COD crystals. It is known to show least amount of peptide interactions. Existence of this plane as the step riser can explain the low affinity of inhibitors to [010] steps.

Our observations suggest that the inhibition of [001] steps is the result of adsorption of inhibitors to (010) step risers. The $(10\bar{1})$ plane is likely the commonly occurring step riser for [010] steps, resulting a lower peptide interaction for that step.

The peptide-step interactions predicted in this chapter can be tested by performing molecular dynamic simulations on $\{100\}$ face with the two step directions and possible step risers.

5 AFM Scanning Effects on Sample Growth and Inhibition

5.1 Introduction

The Atomic Force Microscope (AFM) is a member of the scanning probe microscope family, the members of which image samples by means of a sharp tip [70]. In the case of the AFM, the surface is sensed through deflections of a weak cantilever spring, to which the probe is attached, in response to forces between the tip and the sample surface. It is the only tool that allows real-time, in situ investigations of surface processes at length scales ranging from the molecular level to 100 μm faces in vacuum, air, or liquid [56]. The tip of the AFM is typically a few micrometers long with an end radius often less than 10 nm in diameter. It is located at the free end of a cantilever that is typically 100 to 200 μm long. In contact mode atomic force microscopy, a feedback loop is used to vary the vertical sample position to maintain a constant cantilever deflection while the tip is scanned laterally relative to the sample. The required vertical motion is measured and mapped to create a topographic map of the scanned surface with near-atomic resolution. The AFM has been used to study the growth of mineral surfaces in solution in real time [47,56]. It has the ability to gather topographic information in seconds, allowing the growth kinetics to be studied.

Contact mode is usually used to study crystallization since it has the ability to scan faster than does tapping mode. However, for soft materials, the contact between the tip and surface could affect the surface and crystallization process.

The effects of contact forces can be minimized by several methods. If scanning is performed in fluid, capillary forces are eliminated, reducing contact forces between tip and sample. In order to minimize the forces further, care can be taken to continually adjust the set point voltage to the lowest possible value required to just maintain a tip-sample contact. Experiments performed on numerous systems have shown that a crystal can be imaged this way during growth without disrupting step propagation [56].

Another way that scanning a sample in solution can affect experimental results is the disturbance of solute concentrations due to the moving cantilever. A comparison study of crystal growth and inhibition performed using the AFM and two other observation techniques – Phase Shifting Michelson interferometry (PSMI) and laser confocal microscopy with differential interference

contrast microscopy (LCM-DIM) – revealed that the motion of the AFM tip relative to the sample during the scan can alter the solute concentration distribution in the region surrounding the crystal surface, affecting the growth kinetics [63]. Comparing experimental data on growth kinetics obtained using the three different techniques for the same system under otherwise identical conditions reveals the advantages and limitations of each technique. During that study, step velocities measured by the AFM were significantly faster than those observed by the other methods. This was explained as a result of a cantilever oscillating at high frequency inside the solution (tapping mode) or the constant motion of the cantilever across the sample close to the surface (contact mode). These movements stir the solution significantly, reducing the diffusion boundary layer and increasing the solute concentration near the interface. Consequently, the supersaturation at the step edges increases, resulting in faster step velocities measured by AFM. Similar effects were observed by Land et al. [64], but the changes in growth kinetics due to this effect were not been systematically studied by them. This mixing effect can also increase the inhibitor concentration near the scan surface, enhancing their influence on growth kinetics.

Even with precautions to minimize forces, interactions between the tip and sample in contact mode can create a pressure large enough to damage a soft sample. For example, the tip could scratch the sample surface, leading to enhanced 2D step nucleation [63] thus altering growth kinetics.

When a crystallization process involves adsorption of multiple species to the surface, the tip might affect some adsorbates more than the others. For instance, in the case of crystallization in the presence of peptides or proteins that inhibit crystallization, the AFM tip may interact with the inhibitor molecules, removing them from the surface. In this case, the scan area could exhibit different growth kinetics than the rest of the crystal. For example, the area scanned might have a different height than rest of the crystal due to faster step motion permitted by removal of the inhibitor molecules. One way to test this is to image a smaller scan size at the beginning of an experiment and later increase the scan size to compare regions that were scanned under different conditions.

The purpose of the present study is to observe these tip effects and quantify the results. We use calcium oxalate monohydrate (COM), which is the major constituent of kidney stones [2] as a

model system. Crystallization of COM {010} faces are easily modified by the presence of certain proteins or peptides in the growth solution [25,31,32,49].

5.2 Method

Calcium oxalate solutions and samples were prepared using the methods described in Chapter 2. In brief, calcium and oxalate stock solutions were mixed in tissue culture plate wells (24 well, BD Canada) at 1 mM concentration to nucleate COM crystals. After 3 hours of nucleation, crystals were filtered and transferred to pieces of polished silicon wafers coated with an adhesive partially cured by UV light. These silicon pieces were mounted on AFM specimen disks for scanning.

Crystal growth was imaged in real time using a Multimode AFM with Nanoscope V controller (Bruker) equipped with a glass fluid cell scanning in contact mode at 10 – 30 lines/s. Imaging was performed using SNL-10 (Bruker) silicon nitride cantilevers with an average tip radius of 2 nm and a nominal spring constant of 0.12 N/m.

Crystals were mounted in an initially dry AFM fluid cell. Suitable crystals with horizontal {010} faces were identified using the low-resolution optical microscope attached to the AFM. The fluid cell was then flooded with 0.3 mM calcium oxalate (CaOx) growth solution and left for 3–5 mins, allowing the system to achieve a steady state. The target crystal was scanned to locate an area without any major deformations. Next, the fluid cell was filled with the relevant CaOx solution for the experiment (with or without inhibitor) and the regions were imaged at 15 lines/s over a square scan area of size 1 μm with a 256-line resolution. After 4 minutes, the scan size was increased to 2 μm and two frames were captured before decreasing the scan size to 1 μm again. This process was repeated for 25–30 minutes. At the end of the experiment, the 2 μm images were analyzed to identify any effects due to scanning. Beginning of the experiment applied force from the tip was measured by acquiring a force curve.

In this study, the AFM tip effect was explored under different conditions. Initially, the effects were studied in the absence of inhibitor molecules. Experiments were conducted with a constant CaOx concentration of 0.3 mM and scanning forces ranging from 10 nN to 60 nN (corresponding to set point voltages of 0 V to 8 V) at a scan rate of 15 lines/s. A second set of experiments was performed under the same conditions, but at a scan rate of 12 lines/s.

The AFM tip effect was then studied with an inhibitor present during the growth of the crystal. In this case, calcium oxalate concentration, scan rate and scan force were kept constant at 0.3 mM, 15 lines/s and 25 nN respectively. The growth of {010} faces of COM was studied in the presence of osteopontin (OPN) with a molecular weight of 33 kDa, a macromolecule known to inhibit COM crystallization, [25,32,69] at concentrations ranging from 0.25 $\mu\text{g/ml}$ to 1 $\mu\text{g/ml}$ corresponding to molar concentrations of 7.6 nM to 30 nM. Each experiment was conducted with the procedure described above. Following 20–30 min of imaging, recovery after inhibition was studied by replacing the growth solution containing OPN with pure growth solution. Images were collected in a similar routine as before. Experiments were repeated on different crystals each time in a new sample to confirm findings.

We also performed a study in which the supersaturation was varied. For this, we repeated the above experiments with a single OPN concentration (0.5 $\mu\text{g/ml}$) and CaOx concentrations ranging from 0.3 mM to 0.5 mM while the scan rate and scan force were kept constant.

AFM images captured at 4 min intervals with a scan size of 2 μm were assembled into a movie. The images were corrected for drift and cropped using methods described in Chapter 2. The movies were examined for signs of differentiated growth between the inner 1 μm square section that was imaged continuously and the periphery, which was only imaged every 4 min. In order to analyze the tip effect quantitatively, AFM images were studied further using Igor Pro software (Wave Metrics). Height profiles (cross sections) of AFM height images were acquired along a line from periphery to the inner scan area (red line in Figure 5.1a) using built-in routines. any difference in growth rate between the two regions will result in a step in this profile. Points on the profile calculated by averaging several points along the normal to the profile line segment. The number of samples in the average is determined prior to the operation and was set to 5 in our analysis. In the case of enhanced growth in the scan area, the height profile is expected to begin with an even profile (uniform normal growth rate) and progress into a profile with a step as shown schematically in Figure 5.1.

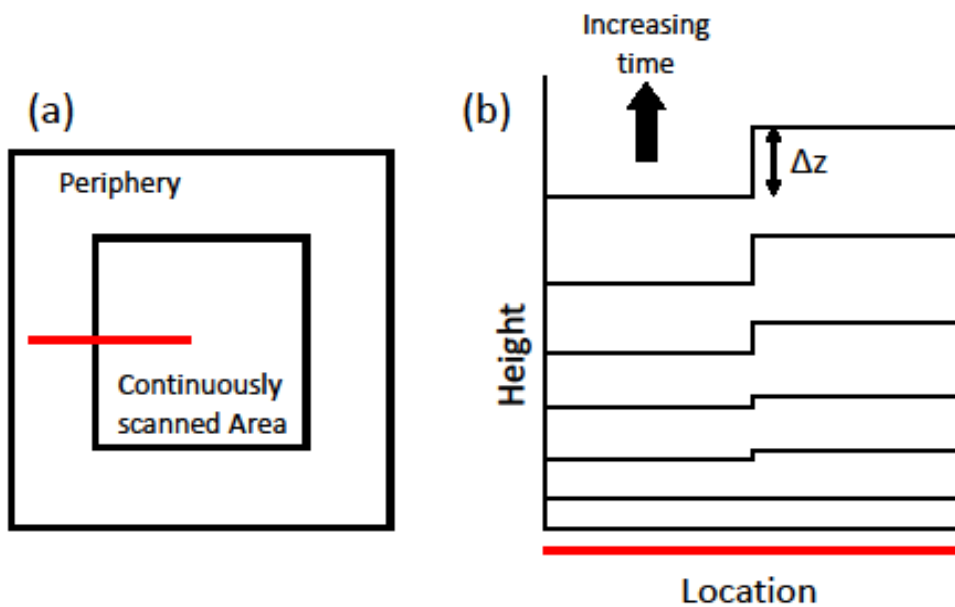


Figure 5.1 Schematic of the expected evolution of the height profile for tip-enhanced growth. (a) AFM scan area divided into a continuously scanned inner area and a periphery that is only scanned periodically. (b) Evolution of the height profile along the red line. In the case of enhanced growth in the inner area, an initially flat profile evolves into a step.

Actual profiles are not perfectly flat due to growth steps and other features. In order to quantify differential growth between the continuously scanned area and the reference peripheral area, the height of the step (Δz) in Figure 5.1 was measured by performing line fits to the two regions with the slope constrained to be the same to account for the possibility of overall surface tilt (Figure 5.2). The height of the step as a function of time can then be extracted as the differences in the intercept of the two-line fits.

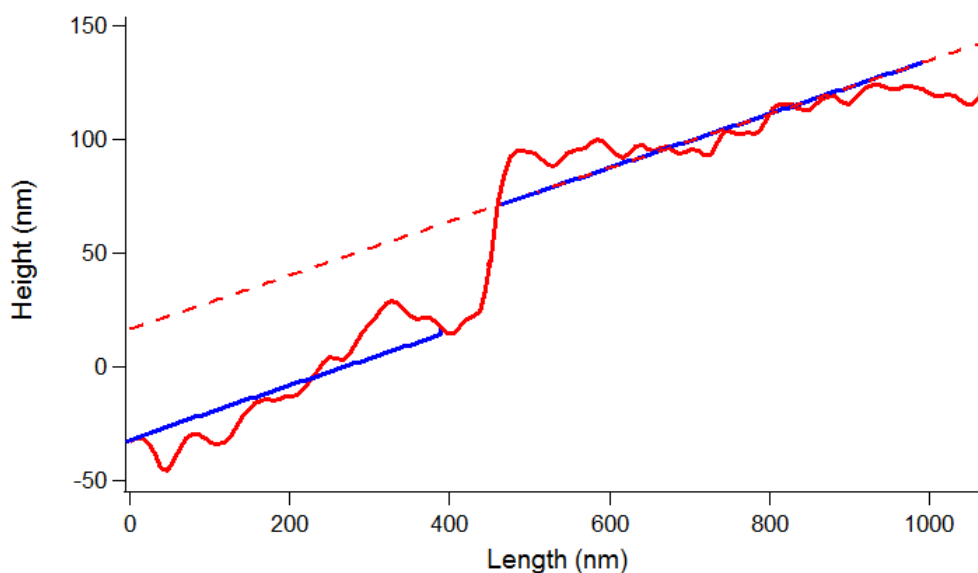


Figure 5.2 Red curve: line profile acquired from an AFM image 20 minutes into crystal growth at 0.3 mM in the presence of 0.5 $\mu\text{g/ml}$ OPN. The blue lines indicate fits to the continuously scanned area and periphery. The dashed line is an extrapolation to show the height difference between the scan area and periphery.

5.3 Results

{010} faces of COM crystals present growth steps arranged in spirals centered at a screw dislocation. In the absence of an inhibitor, no difference in morphology and growth rate between the continually scanned central area and periphery was evident. Figure 5.3 shows three AFM height images acquired over a time span of 10 minutes exhibiting no change in morphology. Increasing the imaging force did not change his observation.

Similar results were observed during a second set of experiments, performed at varying scan rates. Changing the scan rate did not cause any change in the crystal morphology during imaging. Movies made with AFM images confirm uninterrupted crystal growth and lack of enhanced growth.

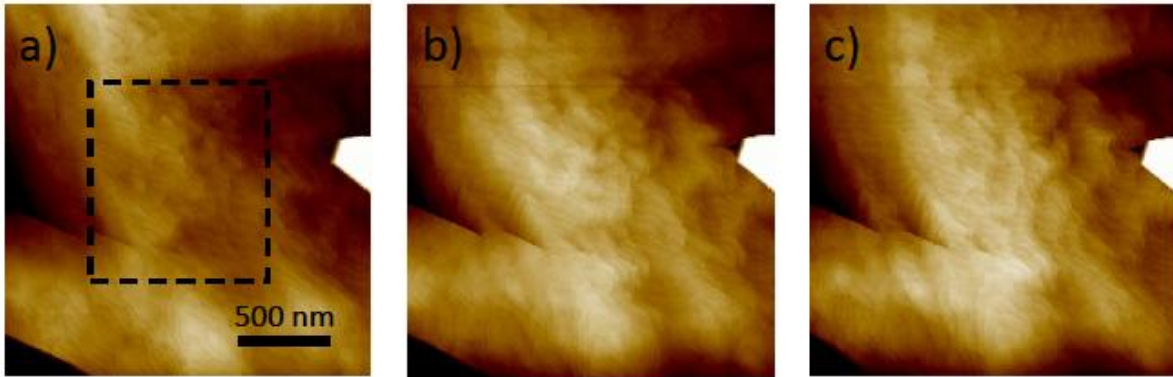


Figure 5.3 Atomic force microscope images of COM crystal growth without inhibitor acquired with an imaging force of 18 nN force at times of a) 0 min into the experiment, b) 4 min into the experiment and c) 10 min into the experiment. No difference between the continuously scanned area, indicated by the dashed lines, and periphery of the image is evident.

In contrast to the results in the absence of inhibitor, growth in the presence of osteopontin exhibited a clear effect due to imaging. All experiments carried out with 0.3 mM CaOx solution in the presence of four different concentrations of OPN showed enhanced growth in the continuously scanned area. Figure 5.4 shows three images taken 7 minutes apart during growth inhibited with 0.5 $\mu\text{g/ml}$ OPN. The initial image (Figure 5.4a), acquired at the beginning of the experiment, shows the scan area and periphery. In the next image, (b), signs of enhanced growth begin to appear. The morphology of the two areas seem similar but the continuously scanned inner area has clearly grown faster than the periphery. The last image, (c), was taken at the end of the experiment and shows a well-defined square corresponding to the continuously scanned region with a greater average height than the periphery.

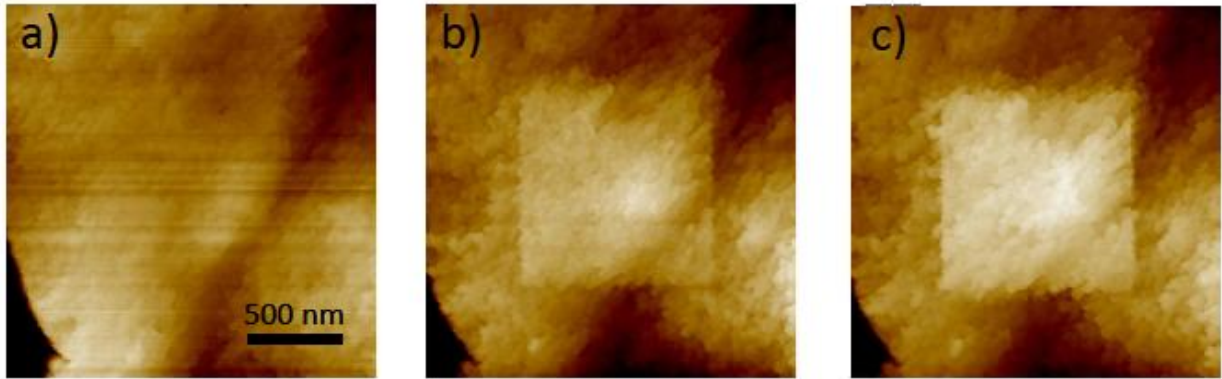


Figure 5.4 Atomic force microscope images of a COM {010} face grown from 0.3 mM CaOx solution in the presence of 0.25 $\mu\text{g/ml}$ OPN. a) First image after inhibitor is introduced. b) 12 minutes into the experiment. The scan area is starting to show enhanced growth relative to the periphery. c) 24 minutes into the experiment. Enhanced growth due to scanning is very prominent.

To determine the uncertainty in individual measurements of the height of the continuously scanned area relative to the periphery, we calculated the standard deviation of the height data in a line profile acquired in the periphery area alone. This provides an estimate of the smallest height difference that can be distinguished from natural height variation.

Further analysis was done by measuring cross sections at several as indicated in Figure 5.5a. In addition, one horizontal and one vertical line profile were analyzed from the periphery area (Figure 5.5b) to estimate the uncertainty in the measurements and as control profiles to compare profile shapes.

Figure 5.6 displays the time evolution of the profile indicated by the red line in Figure 5.5a. It can be seen that both the continuously scanned area and periphery have the same initial height, but that the continuously scanned region grows faster than the periphery as time progresses. Successive height profiles were fitted with two lines constrained to have the same slope and the height difference as a function of time. An example is shown with the values of intercepts in Figure 5.2.

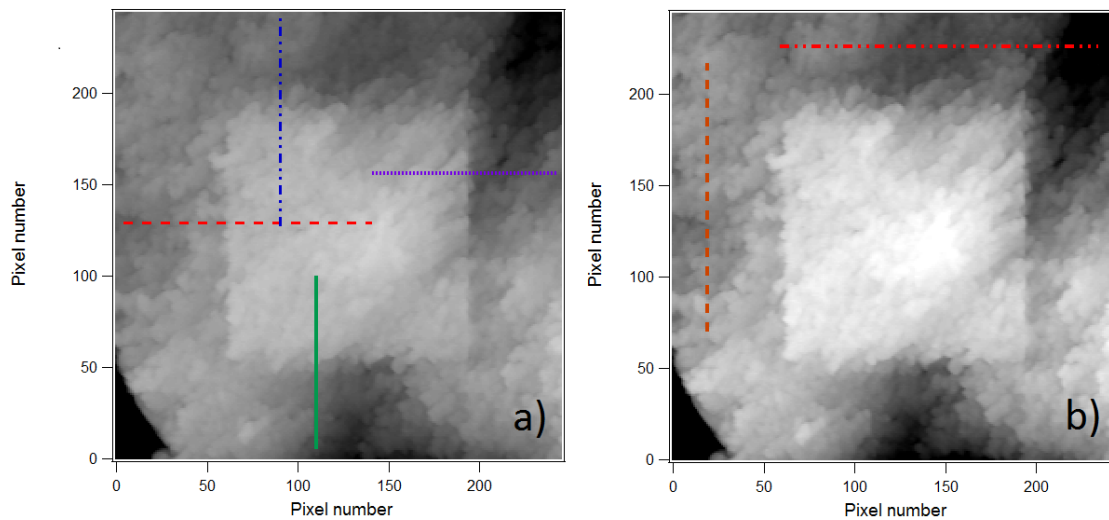


Figure 5.5. a) Locations of line profiles used to measure differential growth between the continuously scanned and periphery regions. b) Two profiles in the periphery used to estimate the uncertainty and as control profile shapes.

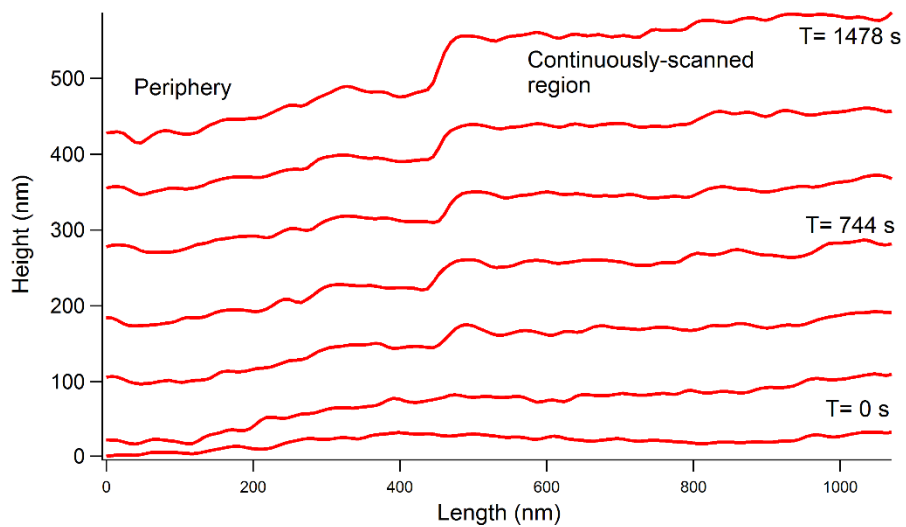


Figure 5.6. Height profiles of a line running from the periphery to the inner scan area (red dashed line in Figure 5.5 a) of the 2 μm scans acquired at 4 minute intervals. Profiles are shown with 100 nm vertical offsets for better visualization of the enhanced growth. a clear height difference between the periphery (left-hand side) and inner scan region (right-hand side) is evident.

Figure 5.7 shows the average height difference (Δz) between the periphery and inner scan area of the four profiles shown in Figure 5.5a as a function of time. The error bars indicate the standard deviation of the four data points for each time.

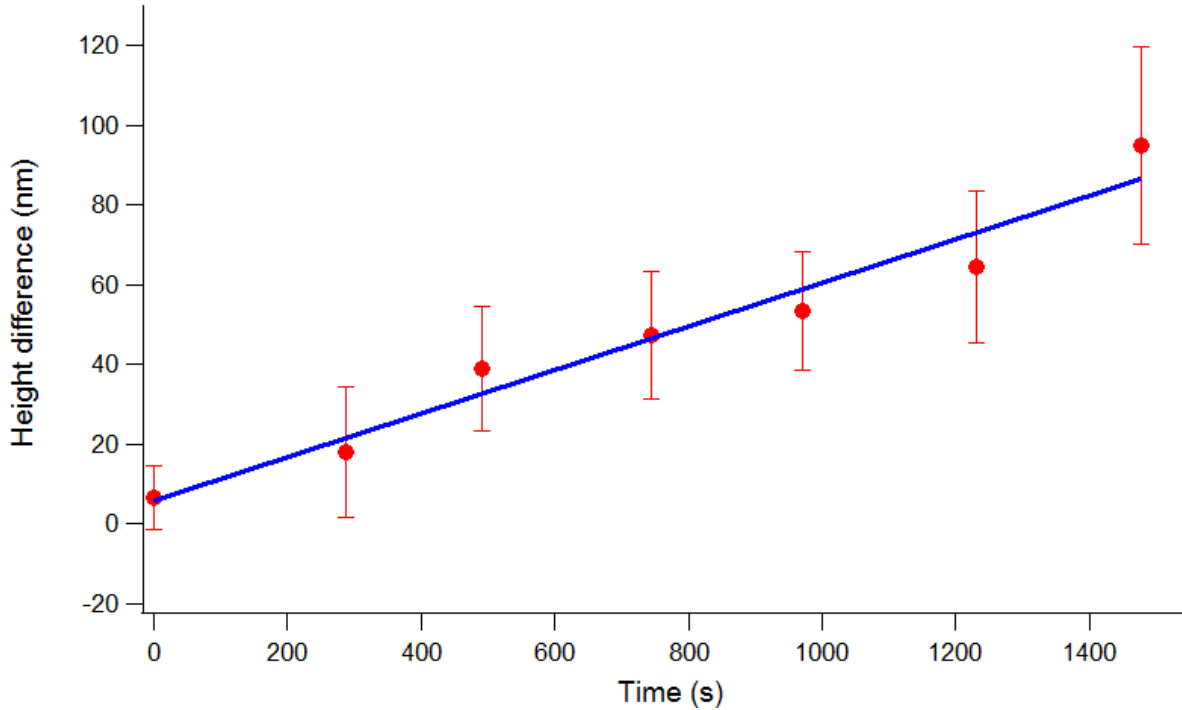


Figure 5.7 Average height difference between the periphery and continuously scanned region as a function of time for a {010} face grown with 0.5 $\mu\text{g/ml}$ OPN from 0.3 mM calcium oxalate solution. The dashed line indicates a linear fit.

Height profiles were gathered for growth in the presence of mass concentrations of 0.25, 0.5, 0.75 and 1 $\mu\text{g/ml}$ OPN at a 0.3 mM CaOx concentration with results summarized in Figure 5.8. As can be seen, the enhancement of growth in the continuously scanned region increases with OPN concentration up to 0.75 $\mu\text{g/ml}$, then decreases.

For steps of height h propagating with velocity v_s , spaced a distance λ apart, the vertical growth rate R of the crystal will be

$$R = \frac{v_s h}{\lambda}. \quad 5.1$$

The observation of differential vertical growth rates between the continuously scanned area and periphery indicates that at least one of v_s , h , and λ is different in the two regions. We observe little difference in the height and spacing of growth steps. So assume for the following analysis that only v_s varies. However, creep in the piezoelectric scanner, the glue attaching the silicon substrate to the AFM stud, and O-ring sealing the fluid cell make absolute sample heights difficult to measure.

Therefore, we can only accurately measure the enhancement of the normal growth (ΔR) in the continuously scanned area for each OPN concentration:

$$R_{Tip} - R = \frac{h}{\lambda}(v_{Tip} - v_s) \quad 5.2$$

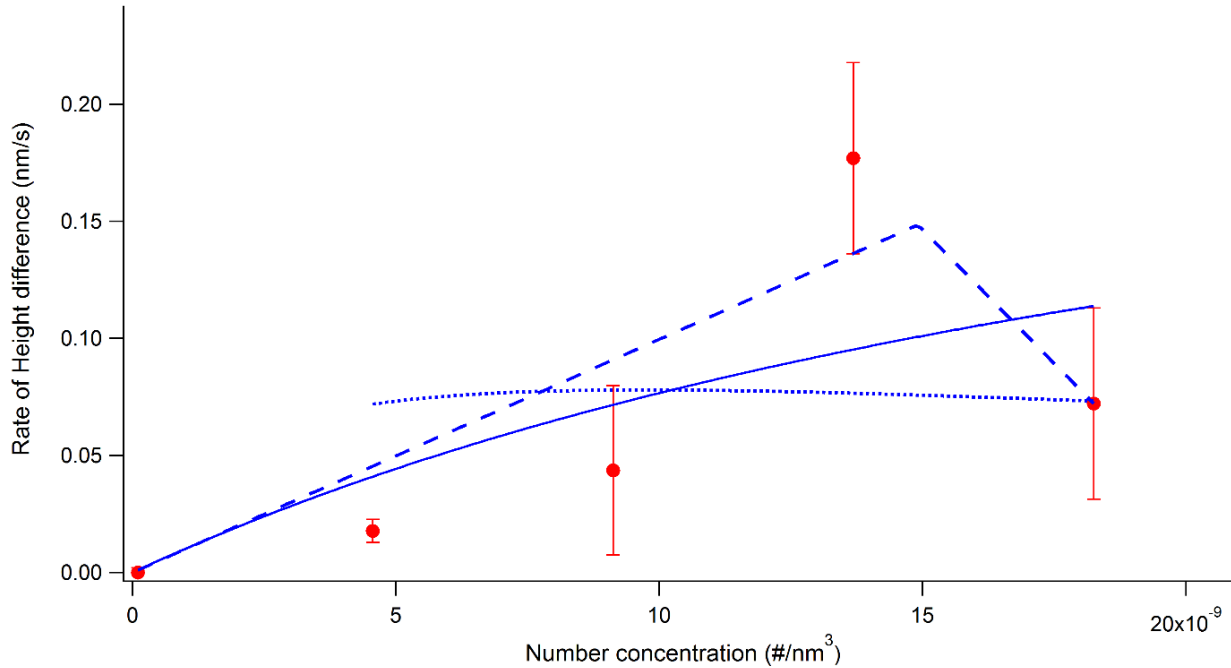


Figure 5.8. Growth rate of the continuously scanned area relative to the periphery, ΔR , as a function of inhibitor concentration. The solid line represents a simple kinetic model. The dotted line shows the fit to a modified C-V model. The dashed line indicates a fit to a one-dimensional pinning model.

Height profiles were gathered for growth in the presence of mass concentrations of 0.25, 0.5, 0.75 and 1 $\mu\text{g/ml}$ OPN at a 0.3 mM CaOx concentration with results summarized in Figure 5.8.

As can be seen, the enhancement of growth in the continuously scanned region increases with OPN concentration up to 0.75 $\mu\text{g/ml}$, then decreases.

We also investigated the effect of calcium oxalate supersaturation on growth enhancement by repeating the experiments at CaOx concentrations of 0.4 and 0.5 mM in the presence of 0.5 $\mu\text{g/ml}$ OPN. Observation for 0.4 mM and 0.5 mM CaOx concentrations were similar to those of the 0.3 mM solution. An enhancement of the growth rate in the continuously scanned area was seen at all supersaturations, as can be seen by the data in Figure 5.9.

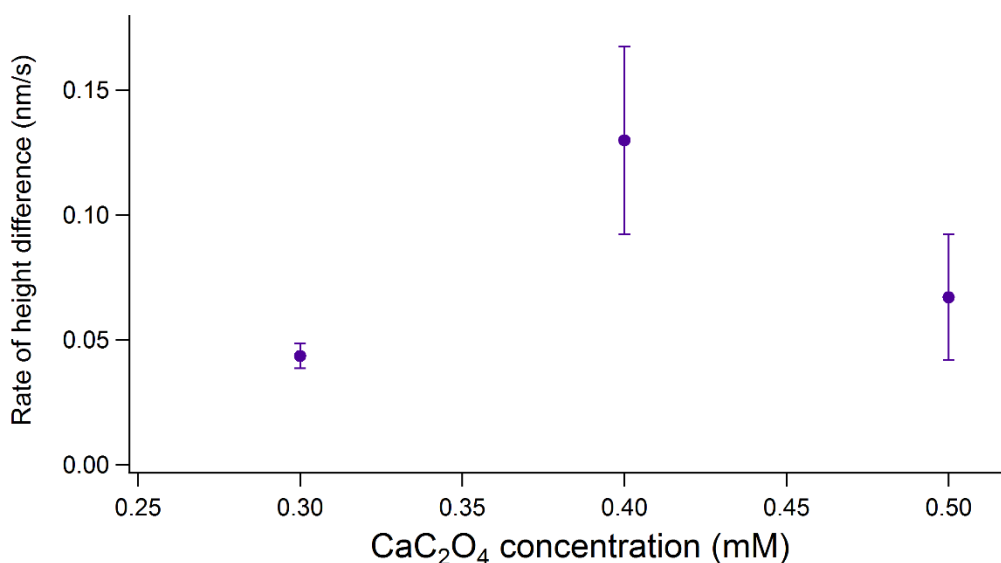


Figure 5.9 Growth rate of the continuously scanned area relative to the periphery for different calcium oxalate concentrations in the presence of 0.5 $\mu\text{g/ml}$ OPN.

5.4 Discussion

Calcium oxalate monohydrate was scanned using the AFM in the absence and presence of inhibitors to study the effect of the AFM tip on their activity. Examining the images in the absence of inhibitor molecules shows no difference between the continuously scanned area and

the periphery, independent of the scan rate and imaging force. We can therefore assume that growth at these conditions is not affected by imaging. Growth in the presence of OPN exhibited an obvious effect due to imaging. Analysis showed that the continuously scanned area grows faster than the periphery. This differential growth must be due to interactions between the tip and inhibitor molecules.

We have measured the height difference between the continuously scanned area and periphery to quantify the enhanced vertical growth rate at various OPN concentrations and CaOx supersaturations. Introduction of CaOx solution without inhibitors to an already-inhibited crystal surface resulted in a rapid recovery of growth from inhibition. This indicates a steady-state inhibitor coverage that is a balance between adsorption and desorption of OPN rather than the irreversible adsorption tacitly assumed by the C-V model. Our goal was to develop a model of the effect of inhibitors on growth and the effect of the AFM tip on inhibition.

We hypothesize that AFM imaging increases the desorption rate of inhibitors, presumably due to interactions between the tip and inhibitor molecules adsorbed to the growth surface. This lowers the steady-state inhibitor coverage in the scanned region and thereby enhances the step velocity. The simplest approach to modelling these effects is to assume a steady-state coverage governed by a Langmuir-like isotherm. The adsorption rate of OPN molecules depends in principle on number of molecules that are within their size l of the surface: lc_i , their characteristic diffusion time l^2/D and the fraction of available binding sites on surface. We assume OPN molecules desorb from the surface at a desorption rate r_- with an additional tip-induced desorption at a rate r_+ . The rate of change of surface inhibitor density (ρ_{2D}) on the continuously scanned surface is then

$$\frac{d\rho_{2D}}{dt} = (1 - \phi)p \frac{D}{l} c_i - (r_- + r_T)\rho_{2D}, \quad 5.3$$

where ϕ is the fraction of adsorption sites occupied by inhibitor molecules and p is a coefficient that contains geometric factors such as the probability of binding and length scales related to diffusion near surface. Incorporation of adsorbed inhibitor molecules might also contribute to the effective off rate. Evidence for incorporation of small molecules into the COM crystals can be found in the studies done by Grohe et al. [31]. For large molecules like OPN, this factor is probably not important.

As a first attempt to model these effects, we consider a modified Cabrera-Vermilyea model with a steady-state population of inhibitor molecules governed by a Langmuir isotherm. An adsorbed polymer with radius of gyration l covers an area l^2 of the surface, so we can then write the fraction of coverage as

$$\phi = \rho_{2D} l^2, \quad 5.4$$

where ρ_{2D} is the number of adsorbed molecules per unit area. This allows us to rewrite equation 5.3 in terms of fraction of coverage as, in the continuously scanned region,

$$\frac{d\phi_T}{dt} = (1 - \phi_T) p D l C_i - (r_- + r_T) \phi_T. \quad 5.5$$

In a steady state, the rate of change of coverage is zero, so that the steady-state coverage is

$$\phi_T = \frac{p D l C_i}{p D l C_i + r_- + r_T}. \quad 5.6$$

The rate of change of inhibitor coverage in the periphery area is same as equation 5.3 without the desorption due to the tip (i.e., with $r_T = 0$). For convenience, calculations are shown only for the continuously scanned area.

The presence of inhibitors influences growth, by modifying the step velocity v_s . For an uninhibited crystal with straight steps, step propagations depends on the flux of solute molecules to the step and is proportional to supersaturation for small supersaturations [7]. The effect of inhibitors on step velocity has been modelled in various ways in literature.

Perhaps the simplest model for the inhibited step speed is to assume that the step speed is modified by a kinetic coefficient β that depends on the amount of inhibitor present on the surface so [22] $v_s = \beta v_0$, where v_s is the inhibited velocity and v_0 is the step velocity without inhibitors.

Another accepted model for step pinning is the Cabrera-Vermilyea (C-V) model, which states that impurities that adsorb to the surface will pin advancing steps and slow them down by forcing the steps to curve between inhibitors (see Chapter 1). The instantaneous velocity of the steps is then given by

$$v_s = v_0 \left(1 - \frac{r^*}{r}\right), \quad 5.7$$

where r is the radius of curvature of the steps and r^* is the (2D) critical radius. In the case of straight steps with low number of kink sites, step inhibition can result from kink-site poisoning.

Such steps propagate by the formation of new kink sites (1-D nucleation). Inhibition of the step can occur by the blocking of kink sites by inhibitor molecules, preventing the spreading of the step [65]. Since steps on {010} faces of COM have measurable roughness, we eliminate this process from our modelling. One other way to model the inhibited step velocity is to consider strong adsorption of inhibitor molecules directly to the step edge, blocking the growth of straight step.

The simplest case of a kinetic coefficient model is to assume a kinetic coefficient β that is inversely proportional to the fraction of coverage. In that case we can write the enhanced growth rate as

$$\Delta R = R_{Tip} - R = \frac{v_0 h}{\lambda} (\beta(\phi_T) - \beta(\phi)) \quad 5.8$$

Where $\beta(\phi)$ describes the kinetic coefficient as a function of inhibitor surface coverage ϕ , and ϕ is an increasing function of c_i . We expect $\beta(\phi)$ to decrease monotonically with ϕ , but the shape of the $\beta(\phi)$ determines $\beta(\phi_T) - \beta(\phi)$ as c_i varied. For instance, if $\beta(\phi)$ has the form $\beta = 1 - \phi$,

5.9

corresponding to the simple assumption that only the fraction of the step without adsorbed inhibitor can grow, then we expect

$$\Delta R = \frac{v_0 h}{\lambda} ((1 - \phi_T) - (1 - \phi)). \quad 5.10$$

Assuming that the coverage ϕ is governed by a Langmuir isotherm with additional desorption due to the AFM tip as described earlier in equation 5.6, we arrive at

$$\Delta R = \frac{v_0 h p D L c_i}{\lambda} \left\{ \frac{r_T}{(p D L c_i + r_-)(p D L c_i + r_- + r_T)} \right\}. \quad 5.11$$

This equation can exhibit a maximum as a function of c_i , but does not show the sharp peak observed experimentally. A nonlinear least-squares to our data does not show a peak, as shown by the solid line in Figure 3.3.

The C-V model states that inhibitor molecules introduced to a crystal system adsorb strongly to the crystal surface and block the step advancement so that the only way for steps to propagate is to curve between pinning sites. The velocity of these steps therefore depends on the spacing between inhibitor molecules. If the spacing is smaller than the critical radius, growth stops altogether. Our observation that the step velocity in the periphery approaches zero, as shown by the AFM images in Figure 5.10c and d, indicates that there must be a threshold inhibitor

concentration that arrests growth. At lower concentrations, the spacing between inhibitor molecules controls the step velocity. From Equation 5.7, we can see that the step velocity ranges between v_0 and $v_0 \left(1 - \frac{r^*}{r}\right)$ as the step passes through a fence of pinning sites. We take the effective velocity to be the average $v_s = v_0 \left(1 - \frac{r^*}{2r}\right)$ with $2r$ given by the spacing between polymers from Equation 5.4:

$$2r = \frac{l}{\sqrt{\phi}}. \quad 5.12$$

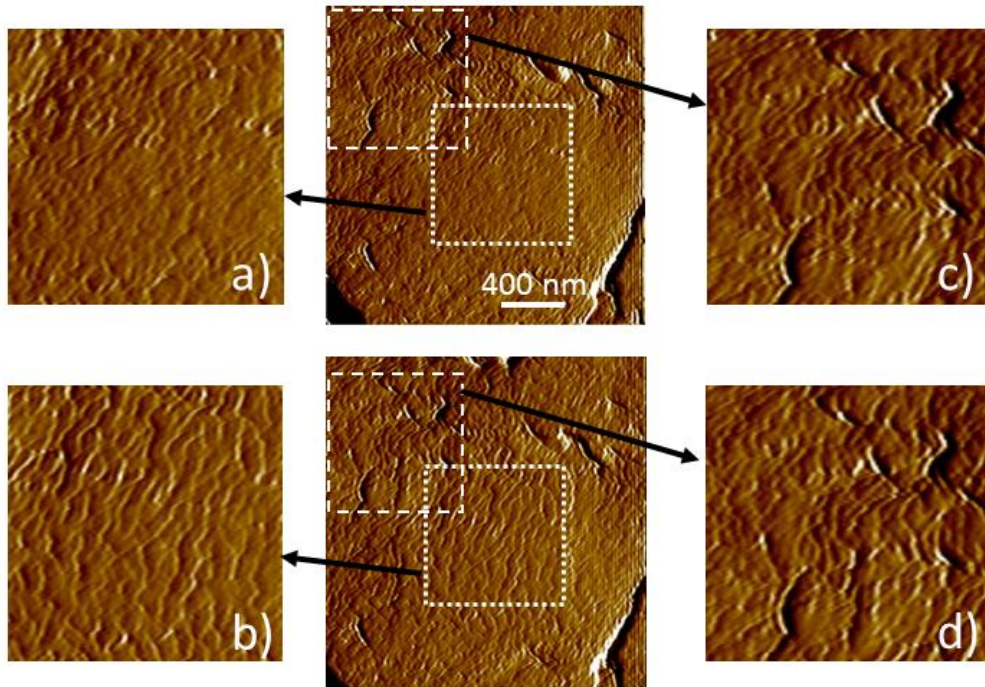


Figure 5.10. AFM images acquired 12 minutes apart while inhibited with 1 $\mu\text{g/ml}$ OPN. Areas enclosed by the dashed line represents the periphery region and by the dotted line represents the inner scan region. a) and b) show magnified sections from the inner scan area. c) and d) are magnifications of the periphery area. The lack of progression of steps from c) to d) is clear.

Combining equations 5.7 and 5.10, the vertical growth rate in the continuously scanned area can be written as

$$R_{Tip} = \frac{v_s h}{\lambda} = \frac{v_0 h}{\lambda} \left(1 - \frac{r^* \sqrt{\phi_T}}{l}\right). \quad 5.13$$

Using equation 5.6 for the coverage, we predict an enhanced vertical growth rate in the continuously scanned area due to the AFM tip relative to the periphery area of

$$\Delta R = R_{Tip} - R = \frac{v_0 h r^*}{\lambda l} [\sqrt{\phi} - \sqrt{\phi_T}] = \frac{v_0 h r^*}{\lambda l} \left[\sqrt{\frac{pDlC_i}{pDlC_i + r_-}} - \sqrt{\frac{pDlC_i}{pDlC_i + r_- - r_T}} \right]. \quad 5.14$$

In the fit to this expression shown in Figure 5.14, the variables v_0 , h , and λ are fixed at values observed experimentally, r^* is estimated from the minimum curvature seen in growth hillocks, and l is estimated from the expected radius of gyration of the polymer. The quantity pDl is treated as a single fit parameter. The best-fit curve returns a value of 3.2×10^{20} m³/s for pDl , which is quite far from the expected value of 5×10^{-23} m³/s based on typical diffusivities of macromolecules in water. Constraining pDl to instead have a value 5×10^{-23} m³/s results in a curve that is an even poorer representation of the data (not shown). We therefore conclude that this model is not valid for the experimental case studied.

A model based on one-dimensional step pinning mechanism introduced in Chapter 3 was more successful. If inhibitor molecules adsorb directly to one dimensional steps with a density of ρ molecules per unit length, the average distance between inhibitor molecules is $1/\rho$. For a molecule that occupies a length l of the step, the average length of regions available for growth is $\frac{1}{\rho} - l$.

The radius r of such a growth region is then

$$r = \frac{1}{2} \left(\frac{1}{\rho} - l \right) = \frac{1 - \rho l}{2\rho}. \quad 5.15$$

A curved step bounded by the ends of such a region will therefore grow with a speed of

$$v_s = v_0 \left(1 - \frac{2\rho r^*}{1 - \rho l} \right). \quad 5.16$$

This results in a predicted vertical growth rate

$$R = \frac{v_s h}{\lambda} = \frac{v_0 h}{\lambda} \left(1 - \frac{2\rho r^*}{1 - \rho l} \right). \quad 5.17$$

As ρ approaches $1/l$, the vertical growth rate reaches its minimum value of zero. Figure 5.10c and d suggest that such a threshold can be reached in our experiments. For small concentrations of inhibitor we find

$$\Delta R = R_{Tip} - R = \frac{v_0 h}{\lambda} \left[\left(1 - \frac{2\rho_T r^*}{1 - \rho_T l} \right) - \left(1 - \frac{2\rho r^*}{1 - \rho l} \right) \right], \quad 5.18$$

where ρ_T and ρ are the steady-state one-dimensional inhibitor densities in the continuously scanned and peripheral regions, respectively. Assuming that inhibitor molecules adsorb directly to steps, the “on” rate will be proportional to the number of molecules that are within their size of the step: There will be $\frac{1}{2}\pi l^2 c_i$. Each of these can move completely to the step in a characteristic diffusion time l^2/D . The rate of change in linear density of inhibitor molecules on a step is then

$$\frac{d\rho}{dt} = \frac{1}{2}p\pi l^2 C_i \frac{D}{l^2} (1 - \phi) - r_- \rho. \quad 5.19$$

In the continuously scanned, area the tip enhanced desorption results in a coverage that changes as

$$\frac{d\rho_T}{dt} = \frac{1}{2}p\pi l^2 C_i \frac{D}{l^2} (1 - \phi_T) - (r_- + r_T)\rho_T. \quad 5.20$$

Since the fraction ϕ of occupied binding sites can be written as ρl , equation 5.19 becomes

$$\frac{d\rho_T}{dt} = \frac{p\pi}{2} C_i D (1 - \rho_T l) - (r_- + r_T)\rho_T, \quad 5.21$$

resulting in a steady state coverage when $\frac{d\rho_T}{dt} = 0$ given by

$$\frac{\rho_T}{(1 - \rho_T l)} = \frac{p\pi}{2} \frac{C_i D}{r_- + r_T}. \quad 5.22$$

Setting $r_T = 0$ yields the corresponding equation for the peripheral region. We can write the expression for the relative enhanced growth rate ΔR for small adsorption densities as

$$\Delta R = \frac{v_0 h}{\lambda} 2r^* \frac{p\pi}{2} D C_i \left[-\frac{1}{r_- + r_T} + \frac{1}{r_-} \right] = \frac{v_0 h}{\lambda} r^* p\pi D C_i \frac{r_T}{r_- (r_- + r_T)}. \quad 5.23$$

There is a threshold concentration of OPN that stops growth altogether in periphery. In that case, concentrations higher than the threshold, when $\rho \rightarrow 1/l$, the relative enhanced growth rate is simply the normal growth rate in the continuously scanned area, which is

$$\Delta R = \frac{v_0 h}{\lambda} \left(1 - r^* p\pi \frac{D C_i}{r_- + r_T} \right). \quad 5.24$$

The concentration at which the ΔR is at a maximum is when the term $\left(1 - \frac{2\rho r^*}{1 - \rho l} \right)$ is minimum in equation 5.18. Using the corresponding equation for equation 5.21 for the peripheral area, concentration at which ΔR is maximum, c_{max} is given by

$$c_{max} = \frac{r_-}{p\pi D r^*}. \quad 5.25$$

We therefore find that this model, the relative growth rate should first increase linearly with concentration with a proportionality constant m , given by

$$m_1 = \frac{v_0 h}{\lambda} r^* p \pi D \frac{r_T}{r_-(r_- + r_T)}. \quad 5.26$$

At higher concentrations ΔR will decrease linearly with c_i with a slope of

$$m_2 = \frac{v_0 h}{\lambda} r^* p \pi D \frac{1}{(r_- + r_T)}. \quad 5.27$$

We have fit our data to this model with parameters shown in Table 5-1, with results shown by the dashed line in Figure 5.8. This fit can provide the ratio between the desorption rate induced by the tip and the natural desorption rate, which is a measure of the importance of tip-induced inhibitor desorption in interpretation of AFM data.

Table 5-1. Fit parameters for the step adsorption model.

Parameter	Value
m_1	$9.95 \times 10^6 \text{ nm}^4/\text{s}$
m_2	$-2.3 \times 10^7 \text{ nm}^4/\text{s}$
c_{max}	$1.49 \times 10^{-8} \text{ \#/ nm}^3$

5.5 Conclusion

The effects of AFM imaging on crystal growth were studied using calcium oxalate monohydrate crystals as a model system. In order to elucidate the effect of the AFM tip on crystal growth, experiments were conducted by continuously scanning a small area on the crystal and a periodically zooming out to scan the periphery area to compare growth and morphology between regions that had been imaged for different amounts of time.

In the absence of inhibitor molecules, the AFM tip has a negligible effect on COM growth. No difference was seen between the continuously scanned area and the periphery, which was scanned only occasionally. This was tested for a range of forces and at varying scan rates. In the

presence of OPN, it was observed that the continuously scanned area grows faster relative to the periodically scanned periphery area. This enhanced vertical growth in the continuously scanned area was measured as a height difference between the two regions and the rate of enhanced growth in the continuously scanned area was measured.

An attempt was made to apply typical inhibition models from the literature to see if they can produce the observed dependence on variables such as inhibitor concentration and supersaturation. It was found that a simple kinetic model would not successfully fit the experiment results. Next, model assuming that inhibitor adsorption is governed by a Langmuir-like isotherm with tip-induced desorption was explored. If we assume that adsorbed inhibitors reduce the step velocity in accordance with Cabrera-Vermilyea model, we are able to predict a peak in the enhanced growth rate as a function of concentration, but we were unable to fit a model to our data with realistic parameters.

Considering instead a one-dimensional inhibitor adsorption model, with OPN molecules strongly binding directly to the step predicts a step velocity that is linearly proportional to the fraction of available binding sites for OPN. Increasing the inhibitor concentration will increase the fraction of occupied binding sites until growth is arrested at a threshold concentration. This model was more successful and is able to provide an estimate of the ratio between the natural desorption rates and tip-induced desorption. These estimates will aid in determining scanning parameters and variables in performing AFM imaging on crystal systems with inhibitors in the future.

6 Conclusion and Future Work

6.1 Summary

Calcium oxalate is a major component of kidney stones, where it can be found in two different crystalline forms: calcium oxalate monohydrate (COM) and calcium oxalate dihydrate (COD) [2]. COM crystals thermodynamically more stable than the COD crystals under physiological conditions and are the most abundant form of calcium oxalate found in kidney stones. Both crystalline forms were studied in our project using the atomic force microscope (AFM) in the presence of proteins and peptides known to inhibit their growth. COM crystal growth was also used to study the effects of AFM imaging on crystal growth.

In the first project, COM crystals were imaged using the AFM in the presence of poly aspartic acid (poly-ASP). Poly aspartic acid is known to inhibit growth on $\{010\}$ faces of COM [1]. At low concentrations of poly-ASP, we observed that one particular direction becomes strongly pinned while the growth continues in other directions. This directional pinning, in approximately the $[120]$ direction, appeared at a threshold concentration of poly-ASP that decreased with increasing poly-ASP length. We presented a simple model to explain this trend. Our model explains the differential inhibition, which is not expected for the C-V model, as arising from inhibition due to adsorption of inhibitors directly to growth steps.

In the second project, $\{100\}$ faces of COD crystals were studied in the presence of several peptides with a range of isoelectric points derived from osteopontin (OPN). In COD, growth hillocks on $\{100\}$ faces are presented as elongated elliptical spirals with principal axes aligned along the $[001]$ and $[010]$ directions. Introduction of peptides to the surface inhibited these step directions to different degrees, resulting in less elongated spiral growth. The observed preferential binding is likely the result of differential calcium ion densities and different atomic structures on different steps of possible step risers for each step direction.

The purpose of the final project was to study the effects of AFM scanning on crystal growth and inhibition. We found that the act of scanning did not affect COM growth in the absence of inhibitors. In the presence of OPN, a continuously scanned area showed faster vertical growth than a peripheral area that was scanned less frequently. This suggests that the differential growth observed is a result of interactions between AFM tip and inhibitor molecules. Increasing the

inhibitor concentration resulted a variation in enhanced vertical growth in the continuously scanned area with a peak at about 0.75 $\mu\text{g/ml}$. We found that a simple kinetic model could not explain the results and the existence of a maximum implied that there must be a threshold inhibitor level that completely arrests growth. Similarly, a model based on the Cabrera-Vermilyea scheme for crystallization inhibition, with a population of inhibitors adsorbed to the surface governed by a Langmuir-like isotherm was unsuccessful. An assumption of inhibitors binding directly to growth fits was able to fit our experimental observations to a reasonable level and provides an estimate of the ratio between desorption induced by the tip and natural desorption. The observation that imaging a crystal growth surface can affect the growth itself is important in interpreting observations of crystal growth and inhibition by atomic force microscopy.

6.2 Future Work

In addition to its medical significance, calcium oxalate is a rich system for studying crystallization and the effects of inhibition by foreign molecules. We propose a number of promising follow-up studies.

6.2.1 COM and COD Crystal Growth

Further investigation is required to confirm the one-dimensional model proposed for COM inhibition by poly-ASP. We have made preliminary attempts to confirm the location of polymer chains by high-resolution AFM imaging during inhibition and by confocal microscopy using fluorescently-labeled poly-ASP to inhibit the crystal.

Another quantity that we can measure to validate the model is the polymer desorption rate. In the proposed model desorption rate was assumed to be negligible, but in reality, it would be a small but a measurable quantity. One way to measure desorption rate is by using the fluorescence recovery after photo bleaching (FRAP) method.

Our understanding of the preferential binding of polypeptides to specific step directions we observed in both COM and COD inhibition could be improved by performing molecular dynamics simulations. Molecular dynamics (MD) simulations have previously been performed by our collaborators, Hunter et al., on COM crystals to study the interactions of peptides derived from ospeopontin with crystal face [32]. Their MD simulations were done using the GROMACS

suite [66], using a force field, that is known to reliably describe the ions, peptides and proteins, was chosen in the simulations. A force field describes interactions between particles (atoms) using a set of equations and parameters used in the set of equations. Using this method, the positions of atoms comprising a slab of COM or COD crystal with the desired step can be placed inside a simulation box with the peptide structure positioned at some distance above the crystal surface. The remaining volume is then filled with water molecules as well as Cl^- ions or Na^+ ions to maintain an overall neutral charge. As the simulation is run, the polypeptide can diffuse through the solution to the crystal surface, allowing the energetics of the interaction to be determined numerically.

6.2.2 AFM Tip Effect on Crystal Growth and Inhibition.

The AFM tip effect observed during crystal growth in the presence of OPN can be further investigated by studying the recovery of growth from an initially-inhibited state. Upon removal of the inhibitor from solution, the adsorption term in the model described in Chapter 5 is eliminated. By comparing the rate of recovery to uninhibited growth in the continuously-scanned region relative to the peripheral region, we in principle determine the ratio between the natural desorption rate and the tip-induced desorption rate.

6.3 Preliminary work

6.3.1 Using Fluorescently Labeled Peptides to Locate poly-ASP on {010} Face of COM.

We labeled aspartic acid chains with a length of 30 monomers with a fluorescent dye (Alexa Fluor 488) and introduced it to a calcium oxalate growth solution of concentration 0.3 mM. A concentration of 20.0 nM of poly-ASP was chosen as this was previously determined to be the threshold for directional pinning of {010} faces under these conditions. COM {010} faces were imaged using a confocal microscope (Zeiss LSM 510) to observe the adsorbed inhibitors.

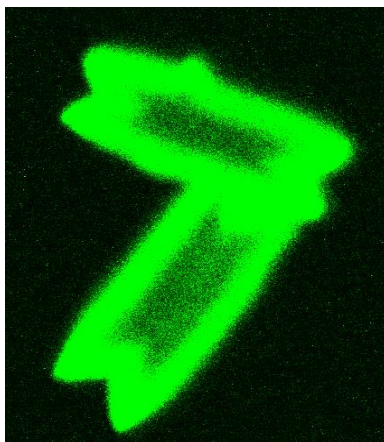


Figure 6.1 Confocal image of $\{010\}$ faces of COM crystals in the presence of 20 nM of fluorescently labeled poly-ASP. Size of a crystal is in the range of 10 – 15 μm .

An example from this experiment is shown in Figure 6.1. The adsorption of labeled poly-ASP to the growth surfaces is readily evident, demonstrating that the labeled molecules are able to interact with the growth surfaces similarly to pol-ASP. Future experiments will focus on higher resolution studies, perhaps with a mix of labeled and unlabeled poly-ASP to reduce the fluorescent signal.

6.3.2 Fluorescence Recovery after Photo Bleaching (FRAP).

Understanding crystal-protein interactions are important in developing models for the resulting growth inhibition. Since the velocity of growth steps on a crystal surface depends on the amount of inhibitor present, it is vital that we have an estimate of the rate at which proteins adsorb to and desorb from the surface. The desorption rate of peptides from $\{010\}$ faces of COM can be measured using the FRAP method.

In brief, COM crystals immersed in a saturated or supersaturated calcium oxalate solution containing a fluorescently-labeled inhibitor are imaged using confocal microscopy. The fluorescence intensity is measured in a steady state. Then a chosen area of interest on the surface is bleached using an Ar laser operating at 95% laser power, subsequently resulting in low fluorescence intensity. As bleached peptides desorb from the surface and are replaced by fresh peptides from the solution, the fluorescence recovers to its initial level. Figure 6.2a shows

fluorescence due to labeled peptides adsorbed to $\{010\}$ faces of COM crystals, while Figure 6.2b shows an example of bleached regions on a COM $\{100\}$ face.

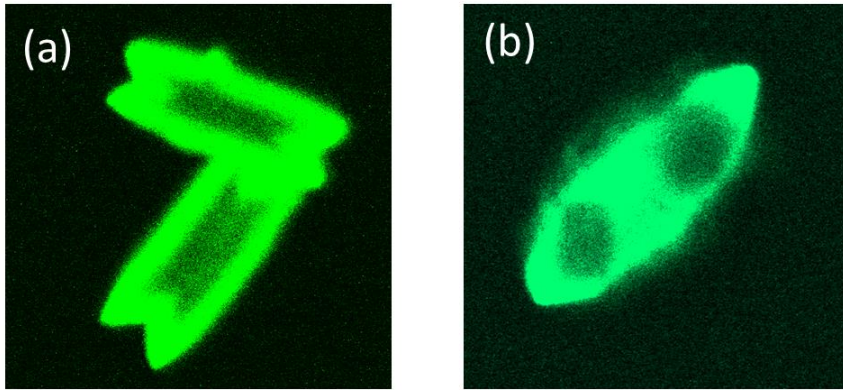


Figure 6.2 Confocal images of COM crystals inhibited with fluorescently labeled peptides. a) COM crystals with $\{010\}$ face up showing the intensity of the adsorbed peptide on the surface. b) An example of bleached regions indicated on COM crystal $\{100\}$ face.

An example of the recovery of fluorescence intensity of a bleached region of a $\{010\}$ face of a COM crystal inhibited by $2 \mu\text{g/ml}$ fluorescently labeled P3, is illustrated in Figure 6.3, where the time period between dashed lines is when the bleaching occurred.

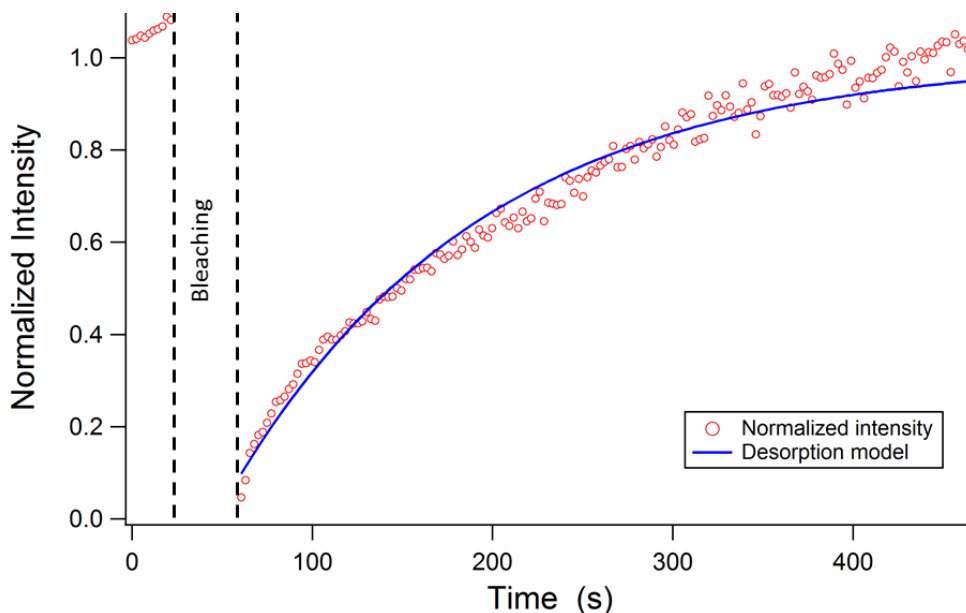


Figure 6.3 Recovery of intensity of a bleached region of a COM {010} face normalized by the initial control intensity for P3 at a concentration of 2 $\mu\text{g/ml}$. The dashed lines indicate the duration of bleaching and the solid line is a fit to a desorption model.

Previous FRAP studies by O'young et al. on COM crystals analyzed recovery following a model developed originally by Sprague et al. [67,68] that assumed an intensity of

$$I(t) = I_{\text{eq}}(1 - e^{-k_{\text{off}}t}), \quad 6.1$$

where I_{eq} is the intensity corresponding to the equilibrium concentration of adsorbed inhibitors, k_{off} is the desorption rate of bleached inhibitor molecules from the surface, and t is the time measured from the end of the bleaching period. In these studies, the k_{off} rate for P3 estimated as 0.001 s^{-1} [71]. For the case shown in Figure 6.3, the measured desorption rate was calculated to be 0.007 s^{-1} .

While our preliminary results were of the same order of magnitude as O'Young's results, our variation was higher. A systematic study of these desorption rates over a range of conditions will provide useful data for validating our models for the interaction of these peptides on COM crystallization.

6.3.3 High Resolution AFM Imaging

Several authors have studied crystallization of COM using high resolution AFM imaging. For instance, De Yoreo et al. have successfully identified inhibitor molecules on COM surfaces and examined the step propagation in the vicinity [25,59]. We have used the AFM to image COM crystal growth in small scan sizes of 20 – 300 nm in the absence and presence of inhibitors in an attempt to locate poly-ASP on the inhibited surfaces with directional pining.

We performed imaging in contact mode at a scan rate of 10 lines/s with a resolution of 512 lines per image. In order to get good quality high-resolution images, an AFM tip with a 2 nm tip radius and 0.03 N/m spring constant (MSNL-W, Bruker) was used. Samples and solutions were prepared using the methods described in Chapter 2 and the inline mixing method was used to replenish growth solution in the fluid cell. The syringe pump was paused as needed for short periods of times (no longer than for 30 s), during image acquisition to avoid any disturbances caused by the flow.

Figure 6.4 is an AFM height image of {010} face of COM acquired at a 20 nm scan size. The features seen on the surface were interpreted as the crystal lattice. The inset in the Figure 6.4 shows a scale drawing of the crystal lattice of a (010) plane overlaid on the AFM image aligned with the step directions determined from a larger image. We can see that the direction of the features in the image are aligned with the [121] crystallographic direction, which is one of the two main step directions observed on {010} face.

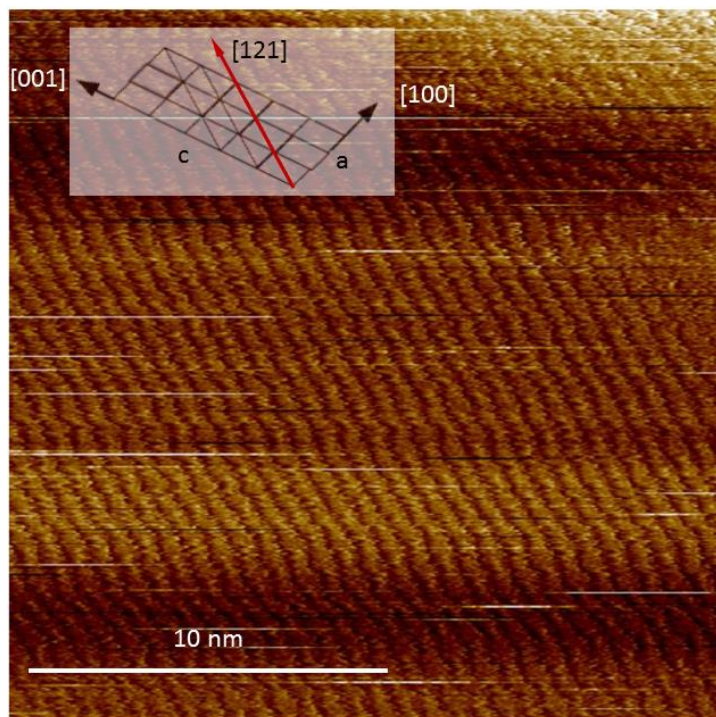


Figure 6.4 High resolution AFM height image of the {010} face of a COM crystal. The inset is a scaled drawing of the crystal lattice aligned with the orientation of the crystal. The red arrow indicates the crystallographic direction [121] aligned with features.

We introduced 0.15 mM calcium oxalate growth solution with a 9 nM poly-ASP (50 residue) concentration. Images were acquired at a scan rate of 8 lines/s. Once the images were constructed in to a movie we could isolate some of the features as possible poly-ASP molecules. Figure 6.5 shows three AFM deflection images, each obtained 60 seconds apart from the other, with possible molecules indicated with circles.

AFM images always contain streaks due to vibrations or removal of material from the surface. In this case, the point is that the streaks reappear in the same place for several successive frames, indicating that they are a real surface feature. These features can be identified in the time-lapse movie (see supplementary movies HighResolution_polyASP50).

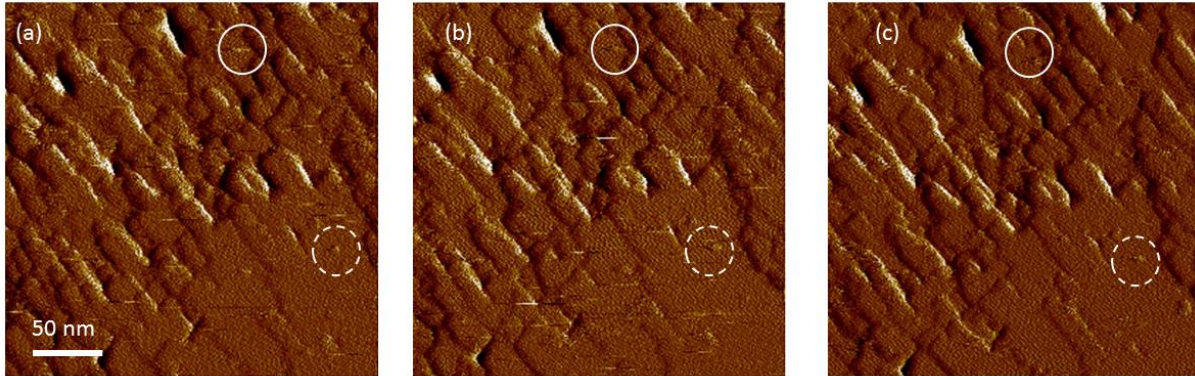


Figure 6.5 High-resolution AFM deflection images of the {010} face of a COM crystal inhibited with 9 nM of poly-ASP 50 acquired 60 s apart. The solid and dashed circles indicate the location of two polymers that persisted for several frames.

These high-resolution images provide details into the adsorbed locations on the surface. Furthermore, for larger molecules such as OPN, it should be possible to directly observe the inhibitor molecules interacting with a propagating step.

High-resolution AFM imaging is work that promises to confirm the adsorption of inhibitors to specific step directions and provide a better understanding of step-inhibitor interactions.

7 Reference

- [1] L. Wang, R. S. Qiu, W. Zachowicz, X. Guan, J. J. DeYoreo, G. H. Nancollas, and J. R. Hoyer, “Modulation of Calcium Oxalate Crystallization by Linear Aspartic Acid-Rich Peptides” *Langmuir* **22**, 7279–7285 (2006).
- [2] M. Daudon “Stone Morphology: Implication for Pathogenesis” *AIP Conference Proceedings* **1049**, 199 (2008).
- [3] X. Sun, J. M. Ouyang, Y.-B. Li, and X.-L. Wen, “Mechanism of Cytotoxicity of Micron/Nano Calcium Oxalate Monohydrate and Dihydrate Crystals on Renal Epithelial Cells” *RSC Advances* **5**, 45393–45406 (2015).
- [4] N. S. Mandel and G. S. Mandel, “Urinary Tract Stone Disease in the United States Veteran Population. II. Geographical Analysis of Variations in Composition” *The Journal of Urology* **142**, 1516–1521 (1989).
- [5] R. Vereecken and W. Proesmans, “A Review of Ninety-Two Obstructive Megaureters in Children” *Eur. Urol.* **36**, 342-347 (1999).
- [6] M. Dudon and F. Cohen-Solal, “Urinary Stones and Urinary Tract Abnormalities. Is the Stone Composition Independent of the Anatomical Abnormality?” *Prog. Urol* **13**, 1320–1329 (2003).
- [7] M. Vesselinov “Crystal Growth for Beginners: Fundamentals of Nucleation, Crystal Growth and Epitaxy” *World scientific publishing co.* **2**, (2016).
- [8] J. De Yoreo, and P. Vekilo, “Principles of Crystal Nucleation and Growth” *Reviews in mineralogy and geochemistry* **54(1)**, 57-93 (2003).
- [9] I. Melikhov, “Trapping during Growth from Solution” *Growth of Crystals* **11**, 309–321 (1979).

- [10] N. Cabrera and D. A. Vermilyea, “The Growth of Crystal from Solution” *Growth and perfection of crystals: Proceedings of an international conference on crystal growth*, 393-410 (1958).
- [11] R. S. Qiu, A. Wierzbicki, A. E. Salter, S. Zepeda, C. A. Orme, J. R. Hoyer, G. H. Nancollas, A. M. Cody, and J. J. Yoreo, “Modulation of Calcium Oxalate Monohydrate Crystallization by Citrate through Selective Binding to Atomic Steps.” *Journal of the American Chemical Society* **127**, 9036–44 (2005).
- [12] S. Farmanesh, R. Ramamoorthy, J. Chung, J. R. Asplin, P. Karande, and J. D. Rimer, “Specificity of Growth Inhibitors and Their Cooperative Effects in Calcium Oxalate Monohydrate Crystallization” *Journal of the American Chemical Society* **136**, 367–376 (2014).
- [13] J. J. De Yoreo, R. S. Qiu, and J. R. Hoyer, “Molecular Modulation of Calcium Oxalate Crystallization” *American Journal of Physiology-Renal Physiology* **291**, F1123–F1132 (2006).
- [14] K. J. Davis, P. ve, L. E. Wasylenki, and J. J. Yoreo, “Morphological Consequences of Differential Mg²⁺ Incorporation at Structurally Distinct Steps on Calcite” *American Mineralogist* **89**, 714–720 (2004).
- [15] A. Chernov, “THE SPIRAL GROWTH OF CRYSTALS” *Soviet Physics Uspekhi* **4**, 116–148 (1961).
- [16] Y. Liu, H. Mao, X. Liu, L. Qiao, and R. Guo, “Calcium Oxalate Crystallization in the Presence of Amphiphilic Phosphoproteins” *Cryst. Eng. Comm.* **16**, 8841–8851 (2014).
- [17] J. A. Wesson, E. M. Worcester, J. H. Wiessner, N. S. Mandel, and J. G. Kleinman, “Control of Calcium Oxalate Crystal Structure and Cell Adherence by Urinary Macromolecules” *Kidney International* **53**, 952–957 (1998).
- [18] J. S. Elliot and I. N. Rabinowitz, “Calcium Oxalate Crystalluria: Crystal Size in Urine” *The Journal of Urology* **123**, 324–327 (1980).

- [19] R. Dyer and B. Nordin, “Urinary Crystals and Their Relation to Stone Formation” *Nature* **215**, 751–752 (1967).
- [20] S. Deganello, “The Basic and Derivative Structures of Calcium Oxalate Monohydrate” *Zeitschrift für Kristallographie - Crystalline Materials* **152**, 247–252 (1980).
- [21] A. Millan, “Crystal Growth Shape of Whewellite Polymorphs: Influence of Structure Distortions on Crystal Shape” *Crystal Growth & Design* **1**, 245–254 (2001).
- [22] M. L. Weaver, R. S. Qiu, J. R. Hoyer, W. H. Casey, G. H. Nancollas, and J. J. Yoreo, “Surface Aggregation of Urinary Proteins and Aspartic Acid-Rich Peptides on the Faces of Calcium Oxalate Monohydrate Investigated by In Situ Force Microscopy” *Calcified Tissue International* **84**, 462–473 (2009).
- [23] M. Carvalho and M. A. Vieira, “Changes in Calcium Oxalate Crystal Morphology as a Function of Supersaturation” *International Braz. J. Urol.* **30**, 205–209 (2004).
- [24] A. Langdon, G. R. Wignall, K. Rogers, E. S. Sørensen, J. Denstedt, B. Grohe, H. A. Goldberg, and G. K. Hunter, “Kinetics of Calcium Oxalate Crystal Growth in the Presence of Osteopontin Isoforms: An Analysis by Scanning Confocal Interference Microscopy” *Calcified Tissue International* **84**, 240–248 (2009).
- [25] S. Qiu, A. Wierzbicki, C. Orme, A. Cody, J. Hoyer, G. Nancollas, S. Zepeda, and D. J. Yoreo, “Molecular Modulation of Calcium Oxalate Crystallization by Osteopontin and Citrate” *Proceedings of the National Academy of Sciences of the United States of America* **101**, 1811–1815 (2004).
- [26] A. Taller, B. Grohe, K. A. Rogers, H. A. Goldberg, and G. K. Hunter, “Specific Adsorption of Osteopontin and Synthetic Polypeptides to Calcium Oxalate Monohydrate Crystals” *Biophysical Journal* **93**, 1768–1777 (2007).

- [27] R. S. Qiu, A. Wierzbicki, A. E. Salter, S. Zepeda, C. A. Orme, J. R. Hoyer, G. H. Nancollas, A. M. Cody, and J. J. Yoreo, “Modulation of Calcium Oxalate Monohydrate Crystallization by Citrate through Selective Binding to Atomic Steps” *Journal of the American Chemical Society* **127**, 9036–9044 (2005).
- [28] C. Zhong, Z. Deng, R. Wang, and Y. Bai, “Inhibition Mechanism of Calcium Oxalate Crystal Growth by Cooperation Influence of Colloidal Selenium Nanoparticles and Bovine Serum Albumin” *Crystal Growth & Design* **15**, 1602–1610 (2015).
- [29] M. Keykhosravani, A. Doherty-Kirby, C. Zhang, D. Brewer, H. A. Goldberg, G. K. Hunter, and G. Lajoie, “Comprehensive Identification of Post-Translational Modifications of Rat Bone Osteopontin by Mass Spectrometry” *Biochemistry* **44**, 6990–7003 (2005).
- [30] P. V. Azzopardi, J. O’Young, G. Lajoie, M. Karttunen, H. A. Goldberg, and G. K. Hunter, “Roles of Electrostatics and Conformation in Protein-Crystal Interactions.” *PloS One* **5**, e9330 (2010).
- [31] B. Grohe, J. O’Young, A. D. Ionescu, G. Lajoie, K. A. Rogers, M. Karttunen, H. A. Goldberg, and G. K. Hunter, “Control of Calcium Oxalate Crystal Growth by Face-Specific Adsorption of an Osteopontin Phosphopeptide” *Journal of the American Chemical Society* **129**, 14946–14951 (2007).
- [32] S. Hug, B. Grohe, J. Jalkanen, B. Chan, B. Galarreta, K. Vincent, F. Lagugné-Labarthe, G. Lajoie, H. A. Goldberg, M. Karttunen, and G. K. Hunter, “Mechanism of Inhibition of Calcium Oxalate Crystal Growth by an Osteopontin Phosphopeptide” *Soft Matter* **8**, 1226–1233 (2011).
- [33] S. S. Nene, G. K. Hunter, H. A. Goldberg, and J. L. Hutter, “Reversible Inhibition of Calcium Oxalate Monohydrate Growth by an Osteopontin Phosphopeptide.” *Langmuir : the ACS journal of Surfaces and Colloids* **29**, 6287–95 (2013).

- [34] H. Shiraga, W. Min, W. VanDusen, Clayman, D. Miner, C. Terrell, J. Sherbotie, J. Foreman, C. Przysiecki, and E. Neilson, “Inhibition of Calcium Oxalate Crystal Growth in Vitro by Uropontin: Another Member of the Aspartic Acid-Rich Protein Superfamily” *Proceedings of the National Academy of Sciences* **89**, 426–430 (1992).
- [35] T. Jung, X. Sheng, C. Choi, W.-S. Kim, J. A. Wesson, and M. D. Ward, “Probing Crystallization of Calcium Oxalate Monohydrate and the Role of Macromolecule Additives with in Situ Atomic Force Microscopy” *Langmuir* **20**, 8587–8596 (2004).
- [36] L. Wang, W. Zhang, R. S. Qiu, W. J. Zachowicz, X. Guan, R. Tang, J. R. Hoyer, J. J. Yoreo, and G. H. Nancollas, “Inhibition of Calcium Oxalate Monohydrate Crystallization by the Combination of Citrate and Osteopontin” *Journal of Crystal Growth* **291**, 160–165 (2006).
- [37] M. L. Weaver, R. S. Qiu, J. R. Hoyer, W. H. Casey, G. H. Nancollas, and J. J. Yoreo, “Inhibition of Calcium Oxalate Monohydrate Growth by Citrate and the Effect of the Background Electrolyte” *Journal of Crystal Growth* **306**, 135–145 (2007).
- [38] K. R. Cho, A. E. Salter, J. J. Yoreo, A. Wierzbicki, S. Elhadj, Y. Huang, and R. S. Qiu, “Growth Inhibition of Calcium Oxalate Monohydrate Crystal by Linear Aspartic Acid Enantiomers Investigated by in Situ Atomic Force Microscopy” *Cryst. Eng. Comm.* **15**, 54–64 (2012).
- [39] B. Grohe, K. A. Rogers, H. A. Goldberg, and G. K. Hunter, “Crystallization Kinetics of Calcium Oxalate Hydrates Studied by Scanning Confocal Interference Microscopy” *Journal of Crystal Growth* **295**, 148–157 (2006).
- [40] C. Cerini, S. Geider, B. Dussol, C. Hennequin, M. Daudon, S. Veessler, S. Nitsche, R. Boistelle, P. Berthézène, P. Dupuy, A. Vazi, Y. Berland, J.-C. Dagorn, and J.-M. Verdier, “Nucleation of Calcium Oxalate Crystals by Albumin: Involvement in the Prevention of Stone Formation” *Kidney International* **55**, 1776–1786 (1999).

- [41] T. Jung, W.-S. Kim, and C. Choi, “Crystal Structure and Morphology Control of Calcium Oxalate Using Biopolymeric Additives in Crystallization” *Journal of Crystal Growth* **279**, 154–162 (2005).
- [42] T. Wang, L. A. Thurgood, P. K. Grover, and R. L. Ryall, “A Comparison of the Binding of Urinary Calcium Oxalate Monohydrate and Dihydrate Crystals to Human Kidney Cells in Urine” *BJU International* **106**, 1768–1774 (2010).
- [43] Y. C. Chien, D. L. Masica, J. J. Gray, S. Nguyen, H. Vali, and M. D. McKee, “Modulation of Calcium Oxalate Dihydrate Growth by Selective Crystal-Face Binding of Phosphorylated Osteopontin and Polyaspartate Peptide Showing Occlusion by Sectoral (Compositional) Zoning” *Journal of Biological Chemistry* **284**, 23491–23501 (2009).
- [44] J. H. Wiessner, G. S. Mandel, and N. S. Mandel, “Membrane Interactions with Calcium Oxalate Crystals: Variation in Hemolytic Potentials with Crystal Morphology” *The Journal of Urology* **135**, 835–839 (1986).
- [45] J. Lieske, F. Toback, and S. Deganello, “Face-Selective Adhesion of Calcium Oxalate Dihydrate Crystals to Renal Epithelial Cells” *Calcified Tissue International* **58**, 195–200 (1996).
- [46] A. Thomas, E. Rosseeva, O. Hochrein, W. Carrillo-Cabrera, P. Simon, P. Duchstein, D. Zahn, and R. Kniep, “Mimicking the Growth of a Pathologic Biomineral: Shape Development and Structures of Calcium Oxalate Dihydrate in the Presence of Polyacrylic Acid” *Chemistry - A European Journal* **18**, 4000–4009 (2012).
- [47] T. Jung, J.-N. Kim, W.-S. Kim, and C. Choi, “Study of Polymeric Additive Effect on Calcium Oxalate Dihydrate Crystal Growth Using Real-Time Atomic Force Microscopy” *Journal of Crystal Growth* **327**, 167–172 (2011).
- [48] B. Grohe, B. Chan, E. S. Sørensen, G. Lajoie, H. A. Goldberg, and G. K. Hunter, “Cooperation of Phosphates and Carboxylates Controls Calcium Oxalate Crystallization in Ultrafiltered Urine” *Urological Research* **39**, 327–338 (2011).

- [49] B. P. Chan, K. Vincent, G. A. Lajoie, H. A. Goldberg, B. Grohe, and G. K. Hunter, "On the Catalysis of Calcium Oxalate Dihydrate Formation by Osteopontin Peptides." *Colloids and surfaces. B, Biointerfaces* **96**, 22–8 (2012).
- [50] Y. Nakagawa, V. Abram, F. Kezdy, E. Kaiser, and F. L. Coe, "Purification and Characterization of the Principal Inhibitor of Calcium Oxalate Monohydrate Crystal Growth in Human Urine." *The Journal of biological chemistry* **258**, 12594–12600 (1983).
- [51] S. Deganello, "The Interaction between Nephrocalcin and Tamm-Horsfall Proteins with Calcium Oxalate Dihydrate." *Scanning microscopy* **7**, 1111–8 (1993).
- [52] S. Deganello, "Interaction between Nephrocalcin and Calcium Oxalate Monohydrate: A Structural Study" *Calcified Tissue International* **48**, 421–428 (1991).
- [53] H. Colfen, "Double-Hydrophilic Block Copolymers: Synthesis and Application as Novel Surfactants and Crystal Growth Modifiers" *Macromolecule rapid communication* **22**, 219–252 (2001).
- [54] D. Zhang, L. Qi, J. Ma, and H. Cheng, "Morphological Control of Calcium Oxalate Dihydrate by a Double-Hydrophilic Block Copolymer" *Chemistry of Materials* **14**, 2450–2457 (2002).
- [55] W. Burton, N. Cabrera, and F. Frank, "The Growth of Crystals and the Equilibrium Structure of Their Surfaces" *Philosophical Transactions of the Royal Society A: Mathematical, Physical and Engineering Sciences* **243**, 299–358 (1951).
- [56] T. A. Land, J. J. Yoreo, and J. D. Lee, "An In-Situ AFM Investigation of Canavalin Crystallization Kinetics" *Surface Science* **384**, 136–155 (1997).
- [57] D. Ricci and P. Braga, "Recognizing and Avoiding Artifacts in AFM Imaging." *Methods in molecular biology* **242**, 25–37 (2004).

- [58] R. Friddle, M. Weaver, S. Qiu, A. Wierzbicki, W. Casey, and D. J. Yoreo, “Subnanometer Atomic Force Microscopy of Peptide–Mineral Interactions Links Clustering and Competition to Acceleration and Catastrophe” *Proceedings of the National Academy of Sciences* **107**, 11–15 (2010).
- [59] T. A. Land, T. L. Martin, S. Potapenko, T. G. Palmore, and J. J. Yoreo, “Recovery of Surfaces from Impurity Poisoning during Crystal Growth” *Nature* **399**, 442–445 (1999).
- [60] A. Aggarwal, R. Tessadri, and B. Grohe, “Protein-Crystal Interactions in Calcium Oxalate Kidney Stone Formation” *International Journal of Biochemistry and Biophysics* **3**, 34–48 (2015).
- [61] S. A. Sukhishvili, Y. Chen, J. D. Müller, E. Gratton, K. S. Schweizer, and S. Granick, “Diffusion of a Polymer ‘Pancake’” *Nature* **406**, 146–146 (2000).
- [62] B. Finlayson and F. Reid, “The Expectation of Free and Fixed Particles in Urinary Stone Disease.” *Investigative urology* **15**, 442–448 (1978).
- [63] A. E. Driessche, F. Otálora, G. Sazaki, M. Sleutel, K. Tsukamoto, and J. A. Gavira, “Comparison of Different Experimental Techniques for the Measurement of Crystal Growth Kinetics” *Crystal Growth and Design* **8**, 4316–4323 (2008).
- [64] T. A. Land, A. J. Malkin, Y. G. Kutznesov, A. McPherson, and J. J. Yoreo, “Mechanisms of Protein and Virus Crystal Growth: An Atomic Force Microscopy Study of Canavalin and STMV Crystallization” *Journal of Crystal Growth* **166**, 893–899 (1996).
- [65] J. De Yoreo, L. Zepeda-Ruiz, R. Friddle, S. Qiu, L. Wasylenki, A. Chernov, G. Gilmer, and P. Dove, “Rethinking Classical Crystal Growth Models through Molecular Scale Insights: Consequences of Kink-Limited Kinetics” *Crystal Growth & Design* **9**, 5135–5144 (2009).

- [66] D. Spoel, E. Lindahl, B. Hess, G. Groenhof, A. E. Mark, and H. J. Berendsen, "GROMACS: Fast, Flexible, and Free" *Journal of Computational Chemistry* **26**, 1701–1718 (2005).
- [67] B. L. Sprague and J. G. McNally, "FRAP Analysis of Binding: Proper and Fitting" *Trends in Cell Biology* **15**, 84–91 (2005).
- [68] B. L. Sprague, R. L. Pego, D. A. Stavreva, and J. G. McNally, "Analysis of Binding Reactions by Fluorescence Recovery after Photobleaching" *Biophysical Journal* **86**, 3473–3495 (2004).
- [69] P. Debye and E. Hückel, "The theory of electrolytes. I. Lowering of freezing point and related phenomena," *Physikalische Zeitschrift* **24**, 185-206 (1923).
- [70] G. Binnig, C. Quate, and C. Gerber, "Atomic Force Microscope" *Physical Review Letters* **56**, 930–933 (1986).
- [71] J. O'Young, "Molecular dynamics and FRAP analysis of protein-crystal interactions" *Faculty of Graduate Studies, University of Western Ontario*, 95-132 (2008)

Appendix A

Recipes for the solutions used in experiments

To facilitate the production of the solutions used in our studies of calcium oxalate crystallization, we prepared stock solutions that could be mixed and diluted to attain with the desired concentration. For this purpose we prepared four stock solutions: 1.5 M sodium chloride (NaCl), 50 mM sodium oxalate ($\text{Na}_2\text{C}_2\text{O}_4$), 50 mM sodium acetate ($\text{NaC}_2\text{H}_3\text{O}_2$) and 50 mM calcium nitrate ($\text{Ca}(\text{NO}_3)_2$). Each chemical was weighed and was dissolved in deionized water with quantities shown in Table A.1 to A.4.

Table A.1 Quantities of chemicals needed for NaCl solution

Sodium chloride (NaCl) solution : 1.5 M		
Constituents	Molar mass	Amount
NaCl	58.44 g/mol	4.383 g
Water	18.02 g/mol	50 ml

Table A. 2 Quantities of chemicals needed for $\text{Na}_2\text{C}_2\text{O}_4$ solution

Sodium oxalate ($\text{Na}_2\text{C}_2\text{O}_4$) solution : 50 mM		
Constituents	Molar mass	Amount
$\text{Na}_2\text{C}_2\text{O}_4$	134.00 g/mol	0.335 g
Water	18.02 g/mol	50 ml

Table A. 3 Quantities of chemicals needed for $\text{Ca}(\text{NO}_3)_2$ solution

Calcium nitrate ($\text{Ca}(\text{NO}_3)_2$) solution: 50 mM		
Constituents	Molar mass	Amount
$\text{Ca}(\text{NO}_3)_2 \cdot 4 \text{H}_2\text{O}$	236.15 g/mol	0.590 g
Water	18.02 g/mol	50 ml

Table A. 4 Quantities of chemicals needed for $\text{NaC}_2\text{H}_3\text{O}_2$ solution

Sodium acetate ($\text{NaC}_2\text{H}_3\text{O}_2$) solution: 50 mM		
Constituents	Molar mass	Amount
$\text{NaC}_2\text{H}_3\text{O}_2$	82.03 g/mol	0.205 g
Water	18.02 g/mol	50 ml

These solutions were used to prepare calcium and oxalate stock solutions with a concentration of 5.88 mM using the quantities shown in Table A. 5 and 6. Micropipettes were used to measure the volumes for the stock solutions, in order to get a precise measurement. Preparation of stock solutions eliminate the need to prepare four separate solution ever single time an experiment is done. Stock solutions are later used to prepare calcium oxalate growth solutions in experiments by diluting them with deionized water to the necessary concentration. Only 17 ml of stock solutions were made at a time, and the stock solutions were only used for two-week time period to avoid any contamination.

Table A. 5 Quantity of each solutions needed to make 5.88 mM oxalate stock solution.

Oxalate stock solution: 5.88 mM		
Constituents	Concentration	Amount (ml)
NaCl solution	1.5 M	5.000
NaC ₂ H ₃ O ₂ solution	50 mM	10.000
Na ₂ C ₂ O ₄ solution	50 mM	2.000

Table A. 6 Quantity of each solutions needed to make 5.88 mM oxalate stock solution.

Calcium stock solution: 5.88 mM		
Constituents	Concentration	Amount (ml)
NaCl solution	1.5 M	5.000
NaC ₂ H ₃ O ₂ solution	50 mM	10.000
Ca(NO ₃) ₂ solution	50 mM	2.000

Concentrations of calcium oxalate solutions used in nucleation and growth with their ion concentrations and ionic strength is shown in Table A.7. Supersaturation corresponding to each concentration was calculated along with the saturation concentration (supersaturation approaches a zero)

Table A.7 Calcium oxalate growth and nucleation concentrations of each ion, calculated ionic strength and supersaturation.

Concentration of CaOx (mM)	Total ion concentration in growth solution (mol/l)						Ionic S (mol/l)	Supersaturation
	Na ⁺	Cl ⁻	CH ₃ OO ⁻	C ₂ O ₄ ²⁻	Ca ²⁺	NO ₃ ⁻		
1.00	0.1620	0.1500	0.0100	0.00100	0.00100	0.0020	0.166	1.32
0.15	0.0243	0.0225	0.0015	0.00015	0.00015	0.0003	0.025	0.58
0.20	0.0324	0.0300	0.0020	0.00020	0.00020	0.0004	0.033	0.75
0.30	0.0486	0.0450	0.0030	0.00030	0.00030	0.0006	0.050	0.97
0.40	0.0648	0.0600	0.0040	0.00040	0.00040	0.0008	0.066	1.10
0.50	0.0810	0.0750	0.0050	0.00050	0.00050	0.0010	0.083	1.18
0.07	0.0107	0.0099	0.0007	0.00007	0.00007	0.0001	0.011	0.00

Appendix B

Design of the continuous flow system for the AFM fluid cell

The AFM fluid cell was connected to a dual syringe pump to obtain a continuous flow of calcium oxalate solution to the cell in order to maintain a constant supersaturation. Legato 270p syringe pump is a push-pull pump that accommodates 2 syringes for infusion and 2 syringes for withdrawal. A smooth flow rate achieved by a small step angle step motor that drives a precision screw and a pusher block that moves the plungers. The pump supports infusion and withdrawal simultaneously at user defined flow rates. We used 20 ml syringes in the pump and set the flow rate to 5 ml/h.

The space between sample and the fluid cell fill up with fluid about 0.5 mm and the fluid cell has a diameter of 6 mm. The volume that flows in a single step (push) passes through a cross sectional area of

$$6 \times 0.5 \times 10^{-6} \text{ m}^2 = 3 \times 10^{-6} \text{ m}^2 .$$

Velocity of the fluid in the cell at a flow rate of 5 ml/h is

$$\frac{\left(\frac{5}{3600} \times 10^{-6} \text{ m}^3/\text{s}\right)}{3 \times 10^{-6} \text{ m}^2} = 4.63 \times 10^{-6} \text{ m/s}$$

A typical sample surface has calcium oxalate crystals spread out randomly on it. When the sample is mounted in the AFM, a circular area with a radius of 3 mm of the sample surface is exposed to growth solution. Typically, there are only about 50 crystals in that area subjected to growth.

We are going to calculate the consumption rate of calcium oxalate ions for crystal growth. For this calculation let us assume that 50% of the sample area is covered with crystals (crystals usually only cover about 5 %). From our experiments, we know that the approximate values of step height h , step velocity v and spacing between steps λ are 1 nm, 2 nm/s and 30 nm respectively. We can therefore estimate the normal growth rate R of the crystal as

$$R = \frac{vh}{\lambda} = 0.067 \text{ nm/s} .$$

Therefore, the volume of crystals increases at a rate of

$$(0.067 \text{ nm/s}) \left(\frac{\pi \times 3^2 \times 10^{-6}}{2} \text{ m}^3 \right) = 9.42 \times 10^{-16} \text{ m}^3/\text{s}$$

Given a density of 2.12 g/cm^3 and a molecular weight of 146 g/mol for calcium oxalate monohydrate, number of moles of solute that get incorporated in to the crystal per unit time is

$$\frac{(9.42 \times 10^{-16} \text{ m}^3/\text{s}) \left(2.12 \times 10^3 \frac{\text{kg}}{\text{m}^3} \right)}{\left(0.146 \frac{\text{kg}}{\text{mol}} \right)} = 1.37 \times 10^{-11} \text{ mol/s}$$

The syringe pump was set at a flow rate of 5 ml/hr , corresponding to $1.38 \times 10^{-9} \text{ m}^3/\text{s}$. At 0.3 mM calcium oxalate concentration, number of moles supplied to the fluid cell per second is

$$\left(0.3 \times 10^{-3} \frac{\text{mol}}{\text{l}} \right) (1.38 \times 10^{-9} \text{ m}^3/\text{s}) \left(\frac{1000 \text{ l}}{\text{m}^3} \right) = 4.65 \times 10^{-10} \text{ mol/s} .$$

Thus, the consumption of calcium oxalate ions for crystal growth is only about 2% of the calcium oxalate supply even for this conservative estimate. We can therefore safely assume that the flow rate is fast enough to avoid any depletion of ions in cell.

Appendix C

List of amino acids

Amino acid	Three letter code	One letter code
alanine	ala	A
arginine	arg	R
asparagine	asn	N
aspartic acid	asp	D
asparagine or aspartic acid	asx	B
cysteine	cys	C
glutamic acid	glu	E
glutamine	gln	Q
glutamine or glutamic acid	glx	Z
glycine	gly	G
histidine	his	H
isoleucine	ile	I
leucine	leu	L
lysine	lys	K
methionine	met	M
phenylalanine	phe	F
proline	pro	P
serine	ser	S

threonine	thr	T
tryptophan	trp	W
tyrosine	tyr	Y
valine	val	V

Curriculum Vitae

S.M. HIMASHA MEDHAVI WIJESEKARA.

Post-Secondary Education

- **PhD candidate** at Department of Physics and Astronomy, University of Western Ontario.
 - **Thesis project-** Effects of impurities on calcium oxalate monohydrate as measured by atomic force microscope.
- **Bachelor of Science (Honours) in Physics** with a Second-class Upper Division from the University of Colombo, Sri Lanka (October 2010), with a GPA of 3.26/4.00
 - Honours project: ‘Analysis of Rainfall: Possible Relations to Self-Organized Criticality.’

Publications

- S.M.H.M. Wijesekara and D.U.J. Sonnadara, “Evidence of Self Organized Criticality in Rainfall”, *In proceedings of the 66th Annual session of the Sri Lanka Association for the Advancement of Sciences*, Sri Lanka, Dec 2010.

Conference Presentations

- H. Wijesekara, R. Schulman, G. K. Hunter, H. A. Goldberg, J. L. Hutter, “Atomic Force Microscopy Study of the Effect of Poly(aspartic acid) on Calcium Oxalate”, *Canadian association of Physicists, Ottawa 2016*
- H. Wijesekara, R. Schulman, G. K. Hunter, H. A. Goldberg, J. L. Hutter, “Real time Real-Time Atomic Force Microscopy Study of the Inhibition of Calcium Oxalate Crystallization by poly (Aspartic acid)”, *Scanning Microscopy on Soft and Polymeric Materials, Toronto, September 2014*
- H. Wijesekara, S.Nene, R. Schulman, G.K.Hunter, H.A. Goldberg and J.Hutter, “Real-Time Atomic Force Microscopy Study of the Inhibition of Calcium Oxalate Crystallization”, *In proceedings of the 2nd CAMBR Distinguished Lecturer and Research Day*, Nov 2012
- Presentation titled ‘*Evidence of Self Organized Criticality in Rainfall*’ in 66th Annual session of Sri Lanka Association for Advancement of Sciences - Colombo Sri Lanka (Dec 2010)

Professional Experience

- **Graduate research assistant** - Department of Physics and Astronomy, University of Western Ontario (Sep 2011 – Present)
- **Graduate teaching assistant** - Department of Physics and Astronomy, University of Western Ontario (Sep 2011 – 2018)
- **Teaching Assistant** - Department of Physics, [University of Colombo - Sri Lanka](#) (Sep 2010 - 2011).
 - Supervised and assessed first and second year students' Introductory Physics and Electronics labs.
 - Assisted 'Practical Session of Research Course Unit' for M.Sc. Students.
 - Proctoring examinations.

Awards and Scholarships

- Western Graduate Research Scholarship, 2011 - 20117
- Graduate Record Examination (GRE) score of 1100 for quantitative + verbal & analytical writing 3.0.
- International English Language Testing System (IELTS) test score of 6.5.
- Best Student (Academic) – Musaeus College (Grade 12-13, 2003)